



**OFFSHORE TECHNOLOGY
RESEARCH CENTER**

**Deterministic Decomposition and Prediction
of Irregular Ocean Waves**

by

J. Zhang, J. Yang, J. Wen,
and I. Prislin

AF

2148

**Deterministic Decomposition and Prediction
of Irregular Ocean Waves**

by

J. Zhang, J. Yang, J. Wen,
and I. Prislin

1998

NSF# CDR-8721512

1/98A9475

For more information contact:

Offshore Technology Research Center
Texas A&M University
1200 Mariner Drive
College Station, TX 77845
(409) 845-6000

or,

Center for Offshore Technology
The University of Texas at Austin
2901 North IH 35, Suite 101
Austin, Texas 78722
(512) 471-3753

Abstract

For the deterministic decomposition and prediction of nonlinear short-crested irregular ocean waves, a Directional Hybrid Wave Model (DHWM), accurate up to second-order in wave steepness, has been developed. The Extended Maximum Likelihood Method is employed to determine the directional spreading of wave energy, and the initial phases of directional free-wave components are calculated using a least-square fitting scheme. The effects of nonlinear wave-wave interactions among the free-wave components are computed using a hybrid second-order wave-wave interaction model which is a combination of conventional and phase modulation approaches. The free-wave components are obtained by decoupling the nonlinear effects from the measurements. The wave decomposition is carried out through an iterative process of computing the free-wave components and their nonlinear interactions. Given an ocean wave field defined by multiple fixed-point measurements, the DHWM is capable of decomposing the wave field into a set of directional free-wave components. Based on the derived free-wave components, the wave characteristics of the wave field can be predicted deterministically and accurately by the DHWM in the vicinity of the measurements. The present method has been verified numerically and applied to both laboratory and field measurements in various scenarios. Satisfactory agreement between the predictions based on the decomposed free-wave components and the corresponding measurements indicates that the proposed method is reliable, flexible and robust. It is expected that the DHWM will have a variety of applications to ocean science and engineering.

Acknowledgment

The theoretical part of this research was supported by the Offshore Technology Research Center which is sponsored in part by National Science Foundation Engineering Research Centers Program Grant Number CDR-8721512 and the numerical and experimental parts by the Joint Industry Program sponsored by Chevron, Exxon, Mobil, Shell, and Texaco. Without their support the research would not be possible. The Coastal Data Information Program made the Harvest pressure measurements available. Mr. C. Wang and D. J. Wisch of Texaco provided the plots of the Harvest platform. Drs. G. Z. Forristall and H. Xu of Shell, and Dr. J. Heideman of Exxon made the Fulmack data available. Their assistance is gratefully acknowledged. Finally, Dr. W. Ye and Mr. E. Meza Conde made constructive comments and suggestions and provided generous help in testing the computer programs.

Contents

Abstract	i
Acknowledgment	iii
1 Introduction	1
2 Mathematical Formulations	6
2.1 The Hybrid Wave Model	6
2.1.1 The Conventional Perturbation Solution	7
2.1.2 The Phase Modulation Solution	8
2.1.3 The Hybrid Wave Model Solution	20
2.2 Directional Decomposition	24
2.2.1 Estimation of Directional Energy Spreading	24
2.2.2 The Extended Maximum Likelihood Method	25
2.3 Determining Initial Phases	27
3 Numerical Schemes	29
3.1 Selection of Representative Directional Free-Wave Components	31
3.2 Initial Phase Fitting	34
3.3 Decoupling Nonlinear Effects	34
4 Numerical Verifications	38
4.1 Consistency and Difference between Conventional and Phase Modulation Approaches	38
4.2 Comparison with Unidirectional HWM	45
4.3 Verification by Synthetic Data	46
5 Comparisons with Laboratory and Field Measurements	53
5.1 OTRC Laboratory Data	54

5.1.1	Experimental Measurement	54
5.1.2	Numerical Recovery and Prediction	56
5.2	HARVEST Field Data	64
5.2.1	Field Measurement	64
5.2.2	Numerical Recovery and Prediction	65
5.3	FULWACK Field Data	69
5.3.1	Field Measurement	69
5.3.2	Numerical Recovery and Prediction	71
6	Conclusions and Further Work	75
	References	77
	Appendix A	81
	Appendix B	84
	Appendix C	86

List of Figures

2.1	Band division of directional hybrid wave model.	21
3.1	Flowchart of the numerical scheme.	30
4.1	Comparison between the conventional perturbation solution (—) and the phase modulation solution (- - -) for a dual free-wave spectrum with $\varepsilon_1 = 0.10$, $\varepsilon_l = 0.3822$: (a) surface elevation; (b) horizontal velocity; (c) vertical acceleration.	40
4.2	Comparison between the conventional perturbation solution (—) and the phase modulation solution (-●-) for a dual free-wave spectrum with $\varepsilon_1 = 0.10$, $\varepsilon_l = 0.3822$: x -direction horizontal velocity profiles of the long- and short-waves up to the leading-order (I —) and the second-order (II —), and long-wave velocity only (-×-).	41
4.3	Comparison between the conventional perturbation solution and the phase modulation solution for a dual free-wave spectrum with $\varepsilon_1 = 0.20$, $\varepsilon_l = 0.139$: (a) short-wave elevation by the conventional perturbation solution at the leading-order (—), and up to the second-order (- - -) and by the phase modulation solution up to the second-order (-●-); (b) short-wave elevation by the conventional perturbation solution at the leading-order (—) and at the second-order (- - -), where Θ_1 is the phase of the long wave.	42
4.4	Comparison between the conventional perturbation solution (—) and the phase modulation solution (-●-) for a dual free-wave spectrum with $\varepsilon_1 = 0.20$, $\varepsilon_l = 0.139$: x -direction horizontal velocity profiles of the long- and short-waves up to the leading-order (I —) and the second-order (II —), and long-wave velocity only (-×-).	43
4.5	Unidirectional free-wave spectrum for verification of the DHWM against the unidirectional HWM.	46

4.6	Comparison of the DHWM (—) with the unidirectional HWM (- - -): (a) surface elevation; (b) dynamic pressure; (c) horizontal velocity.	47
4.7	Comparison of the DHWM (—) with the unidirectional HWM (- - -) for a unidirectional breaking wave case: (a) free-wave spectrum; (b) surface elevation; (c) dynamic pressure.	48
4.8	Free wave components (4) used as input (o) for the wave field simulation and their output (Δ) after the wave field decomposition.	50
4.9	Free wave components (64) used as input (o) for the wave field simulation and their output (Δ) after the wave field decomposition.	51
5.1	Surface elevation time-series as input (o) for the wave field decomposition and the corresponding recovered results (—) for the OTRC laboratory data at: (a) W1; (b) W4; (c) W5.	57
5.2	Pressure time-series as input (o) for the wave field decomposition and the corresponding recovered results (—) for the OTRC laboratory data at: (a) P1; (b) P5; (c) P7.	58
5.3	Pressure time-series as measurements (o) and the corresponding predicted results (—) for the OTRC laboratory data at the location of P6: (a) predicted from the surface elevation measurements; (b) predicted from the pressure measurements.	59
5.4	Surface elevation time-series as measurements (o) and the corresponding predicted results (—) for the OTRC laboratory data at the location of W3: (a) predicted the from surface elevation measurements; (b) predicted the from pressure measurements.	60
5.5	Pressure time-series as measurements (—) and the corresponding predicted results from the decomposed free-wave components based on the surface elevation time-series at W1–W5 with one (- - -) and seven (- - -) wave components at each frequency for the OTRC laboratory data: (a) at the location of P2; (b) at the location of P3.	62

5.6	Pressure time-series as input (o) for the wave field decomposition and the corresponding recovered results (—) for the HARVEST field measurements at: (a) P1; (b) P2; (c) P3.	66
5.7	Pressure time-series as measurements (o) and the corresponding predicted results (—) for the HARVEST field measurements at: (a) P4; (b) P5; (c) P6.	67
5.8	Time-series as input (o) for the wave field decomposition and the corresponding recovered results (—) for the FULWACK field measurements: (a) surface elevation at the location of the wave gauge, (b) V_x at EMV 5; (b) V_y at EMV 5.	73
5.9	Velocity time-series as measurements (o) and the corresponding predicted results (—) for the FULWACK field measurements: at EMV 4: (a) V_x ; (b) V_y	74

List of Tables

5.1	Coordinates of the sensors in the OTRC model test (prototype scale). . .	55
5.2	Standard errors and correlation coefficients between the measured and computed time-series for the OTRC laboratory data.	61
5.3	Coordinates of the sensors for the HARVEST field measurements. . . .	65
5.4	Standard errors and correlation coefficients between the measured and computed time-series for the HARVEST field measurements.	68
5.5	Coordinates of the sensors in the FULWACK field measurements. . . .	70

.....

.....

.....

1 Introduction

A deterministic description of multi-directional waves can provide the prediction of wave characteristics in the time domain based on related measurements. This capability is lack in existing studies, and yet is desirable to many ocean and coastal science and engineering applications. For example, in order to determine the statistics of typical wave characteristics of rough seas, such as wave groupness, the maximum wave height or crest height and related wave period, measured surface elevations are needed. While surface elevations can be readily measured in the laboratory, surface elevations in the ocean are often indirectly measured using pressure transducers, velocity meters or other instruments. Thus it requires the above mentioned capability to deduce the surface elevation based on indirect measurements. This study aims at the development of a nonlinear directional wave model and related numerical scheme which can make the deterministic predictions of general wave characteristics of short-crested seas based on the measurements of a variety of commonly deployed instruments.

Ocean waves can be intuitively viewed as the constitution of many wave components of different frequencies, amplitudes and advancing in different directions. The basic wave components, known as free-wave (or linear) components, obey the dispersion relation. Due to the nonlinear nature of surface waves, the interactions among these free-wave components result in bound-wave components which in general do not obey the dispersion relation. When linear wave theory is employed, bound-wave components are either ignored or treated as free-wave components of the same frequency. The procedure of predicting waves characteristics is first to decompose a measured wave field into free-wave components and then to superpose the corresponding wave characteristics of the free-wave components and their interactions (bound-wave components). In the case of unidirectional irregular waves, linear wave theory with the help of the Fast Fourier Transform (FFT) can deterministically determine wave characteristics based on the measurement at a fixed point. Because ocean wave are often directional or short-

crested, the assumption of unidirectional waves is sometimes unrealistic. In the case of directional seas, the number of simultaneous wave records of a wave field is often limited to as few as three to five due to the cost. The use of two-dimensional FFT to decompose a wave field is prohibited. Alternatively, linear wave theory together with cross-spectrum analyses are used to derive a directional frequency-amplitude or energy spectrum, which is no longer a deterministic decomposition of a measured wave field. As a result, the information of the initial phases of wave components is lost. Hence, quite different from a unidirectional wave field, wave characteristics of short-crested ocean waves in general can not be deterministically predicted based on the measurements even under the assumption of linear wave theory. Wave characteristics is simulated based on the assumption of random phases of wave components. However, it is well known that quite different wave processes may have the same or similar spectrum if the relative phases of wave components are not specified (Funke & Mansard 1981).

In the cases of steep ocean waves, the contributions of bound-wave components may become dominant or important with respect to the free-wave components of the same frequency in the frequency bands either lower or higher than the spectral peak frequency (Zhang *et al.* 1996a). Because the relationship between the elevation and potential of free-wave components are different from those of bound-wave components, predicted wave properties using linear wave theory, for example wave kinematics based on measured wave elevation or wave elevation based on measured dynamic pressure, were found to be quite inaccurate for steep waves (Torum & Gudmestad 1989; Spell *et al.* 1996; Zhang *et al.* 1996b). For accurate prediction, nonlinear wave effects have to be considered in the decomposition and superposition of a wave field. That is, the bound-wave components are decoupled from the measured wave characteristics before a wave field is decomposed into its free-wave components. Based on the free-wave components, the bound-wave components can be computed and the resultant wave characteristics nearby the measurements can be obtained as the superposition of free-wave and bound-wave components. In the case of unidirectional irregular waves, it has been shown that

the hybrid nonlinear wave model (HWM) can provide more accurate predictions than using linear wave theory (Spell *et al.* 1996). Encouraged by the success in unidirectional irregular waves, this study is envisioned.

Previous studies on the measurements of short-crested waves have been dominated by statistical approaches. The statistical approaches based on linear wave theory were well documented. For reference, readers are referred to Borgman (1990). Using weakly nonlinear wave theory, attempts were made to decouple the energy of bound-wave components from the measured energy spectrum (Tick 1959; Weber & Barrick 1977; Komen 1980). Assuming a directional wave-energy spreading function, Masuda *et al.* (1979) and Mitsuyasu *et al.* (1979) showed the contribution from second order bound-wave components is significant at the frequencies about twice of the spectral peak frequency in wind waves generated in a flume. Using poly-spectra analyses, Herbers & Guza (1991 & 1992) showed that the nonlinear contributions from the sum- and difference-frequency interactions could be significant in measured short-crested wave pressure and particle velocities. In spite of many differences, a common assumption made in these nonlinear statistical studies is that the initial phases of free-wave components are independent and randomly distributed between 0 to π . Contrary to the abundance of studies based on statistical approaches, the corresponding studies based on deterministic approaches were very rare. Our literature survey only found an early attempt by Sand (1979) and recent one by Schaffer & Hyllested (1994), and both of them were based on linear wave theory. Besides, their methods were limited to the measurements of one surface elevation and two horizontal velocity components and sometimes there could be significant energy losses during the wave decomposition.

The study presented in this report is deterministic and considers both wave directionality and nonlinearity. In several respects, this study is innovative and unique. First, based on as few as three independent measurements recorded at fixed-points, the DHWM is able to decompose a directional irregular wave field into free-wave components without the assumptions of random initial phases of free-wave components and a prior

directional spreading function. Secondly, the nonlinear effects are decoupled from the measured wave characteristics by using two different perturbation approaches: a conventional and a phase modulation methods. It was found that truncated solutions for bound-wave components given by a conventional perturbation method may not converge if the wavelengths of two interacting wave components are quite different while the convergent solutions can be derived using the phase modulation method (Zhang *et al.* 1993). For a wave field of energy distributed in a relatively broad frequency band, the use of both conventional and phase modulation methods to describe the wave-wave interaction can provide convergent solutions for unidirectional irregular waves (Zhang *et al.* 1996a), which is also numerically demonstrated for multi-directional waves in § 4.1. In our earlier study, only conventional method was used for the solution of bound-wave components, which limits the application to a wave field of a relatively narrow-band spectrum (Prislin *et al.* 1997). Thirdly, this study renders deterministic predictions of wave characteristics of a measured directional field. It is demonstrated that a variety of wave measurements (pressure transducers, surface pericing wave gauges and velocimetry) can be used as input for the wave decomposition. Since all wave characteristics can be computed based on the potential of free-wave components, our method can be straightforwardly extended to allow for other measurements, such as wave slopes and accelerations as well. Finally, because of above capabilities, extensive and rigorous examinations about the validity and accuracy of this model and numerical scheme can be made through the comparisons in the time-domain between the predicted wave characteristics and the corresponding laboratory and field measurements.

In addition to the neglect of viscous and wind effects, and wave breaking due to the use of potential theory, the proposed directional hybrid wave model (DHWM) developed in this study is truncated at second order in wave steepness. The ‘weak’ or resonant wave interactions in deep or intermediate-depth water are of third order and hence are not considered. The weak wave interactions can become substantial after hundreds of dominant wave periods (Su & Green 1981; Phillips 1979). Hence, for accurate prediction,

the computation of wave characteristics based on this study should be limited within a short distance from the measurements (typically a few wavelengths of the dominant wave components) and the proposed model is not valid for the study of long-term or long-distance wave evolution, such as wave energy transfer among wave components with different frequencies (Hasselmann 1962).

The report is organized in the following manner. In § 2 the mathematical formulations of the DHWM are described. To materialize the DHWM, numerical procedures for the decomposition of a directional wave field are detailed in § 3. Numerical verifications of the present theory and methods are elaborated in § 4. The predictions based on the present method are compared with both laboratory and field measurements in various scenarios, and the accuracy and usefulness of the DHWM are examined in § 5. Finally, the conclusions and further work are presented in § 6.

2 Mathematical Formulations

2.1 The Hybrid Wave Model

For an incompressible and irrotational flow with a free surface, the governing equation and boundary conditions can be written as

$$\nabla^2 \Phi = 0, \quad -h \leq z \leq \zeta, \quad (2.1)$$

$$\frac{\partial \Phi}{\partial t} + \frac{1}{2} |\nabla \Phi|^2 + g\zeta = C_0 \quad \text{at } z = \zeta, \quad (2.2)$$

$$\frac{\partial \zeta}{\partial t} + \frac{\partial \Phi}{\partial x} \frac{\partial \zeta}{\partial x} + \frac{\partial \Phi}{\partial y} \frac{\partial \zeta}{\partial y} = \frac{\partial \Phi}{\partial z} \quad \text{at } z = \zeta, \quad (2.3)$$

$$\frac{\partial \Phi}{\partial z} = 0 \quad \text{at } z = -h, \quad (2.4)$$

where Φ is the velocity potential, ζ the surface elevation, t time, g the gravitational acceleration and h the water depth which is assumed to be uniform in this study. The x -axis is set at the calm water level, the y -axis is orthogonal to x -axis in the horizontal plane, and the z -axis is pointing upwards. C_0 is the Bernoulli constant which will be chosen to ensure $z = 0$ located at the calm water level.

The conventional perturbation method (Longuet-Higgins 1962) may render the truncated solutions for the wave-wave interaction problem in the order of wave steepness, defined as the product of the wave number and amplitude. When the ratio of the short-wavelength to that of the long wave, ε_l , is of $O(1)$, the conventional perturbation solution converges very quickly. However, when ε_l is small and approaches the long-wave steepness ε_1 , the truncated solution converges slowly and eventually diverges (Zhang *et al.* 1993).

The phase modulation method proposed by Zhang *et al.* (1993) is an complementary solution to the conventional perturbation method. It considers the consequence of wave interactions as the modulation on the short wave by the long wave and describes it

directly in the solution of the short-wave component. For unidirectional waves the phase modulation solution has been proved to be identical up to third-order in wave steepness with the conventional perturbation solution when $\varepsilon_1 \ll \varepsilon_l < 0.5$. However, as ε_1 becomes larger and greater than ε_l , the conventional perturbation solution diverges, while the phase modulation solution is convergent. But, when $\varepsilon_l > 0.5$, the phase modulation method can not accurately predict the slowly varying interaction between the two wave components at third-order in wave steepness (Zhang *et al.* 1993; Chen & Zhang 1997). The work conducted in this section is to extend the previous results to directional waves.

2.1.1 The Conventional Perturbation Solution

The conventional solution for the potential of the interaction between two directional wave components in an intermediate-depth water was given by Longuet-Higgins (1962) and Hsu *et al.* (1979),

$$\begin{aligned} \Phi = & \sum_{i=1}^2 \left\{ \frac{a_i g \cosh[k_i(z+h)]}{\sigma_i \cosh(k_i h)} \sin \theta_i + \frac{3 a_i^2 \sigma_i \cosh[2k_i(z+h)]}{8 \sinh^4(k_i h)} \sin(2\theta_i) \right\} \\ & + \frac{a_1 a_2 \sigma_2}{2} A_{(-)} \frac{\cosh[|\mathbf{k}_1 - \mathbf{k}_2|(z+h)]}{\cosh(|\mathbf{k}_1 - \mathbf{k}_2|h)} \sin(\theta_1 - \theta_2) \\ & + \frac{a_1 a_2 \sigma_2}{2} A_{(+)} \frac{\cosh[|\mathbf{k}_1 + \mathbf{k}_2|(z+h)]}{\cosh(|\mathbf{k}_1 + \mathbf{k}_2|h)} \sin(\theta_1 + \theta_2), \end{aligned} \quad (2.5)$$

where

$$A_{(\mp)} = \mp \frac{k_2 [2\lambda(1 \mp \lambda)(\Gamma \alpha_1 \alpha_2 \pm 1) \mp \lambda^3(\alpha_1^2 - 1) + \alpha_2^2 - 1]}{k_2(1 \mp \lambda)^2 - \alpha_2 |\mathbf{k}_1 \mp \mathbf{k}_2| \tanh(|\mathbf{k}_1 \mp \mathbf{k}_2|h)}, \quad (2.6a)$$

$$\lambda = \frac{\sigma_1}{\sigma_2}, \quad (2.6b)$$

$$\alpha_i = \coth(k_i h), \quad i = 1, 2, \quad (2.6c)$$

$$\Gamma = \cos(\beta_1 - \beta_2), \quad (2.6d)$$

$$\theta_i = k_{ix}x + k_{iy}y - \sigma_i t + \delta_i, \quad i = 1, 2, \quad (2.6e)$$

in which a_i , β_i , k_i , σ_i and δ_i represent the wave amplitude, directional angle with respect to the x -axis, wave number vector, frequency and initial phase of the i th wave component, k_i is the modulus of the wave number vector, $k_i = |k_i|$, k_{ix} and k_{iy} represents the x - and y -components of k_i , respectively. By default, a smaller subscript indicates a lower frequency for the wave component, i.e. $\sigma_1 < \sigma_2$. The subscripts of sign (+) and sign (-) indicate the sum and difference type interactions, respectively. The conventional solution for the surface elevation is in the form of

$$\begin{aligned} \zeta = & \sum_{i=1}^2 \left\{ a_i \cos \theta_i + \frac{a_i^2 \sigma_i^2}{4g} \left[2 + \frac{3 \cosh(2k_i h)}{\sinh^4(k_i h)} - \frac{1}{\sinh^2(k_i h)} \right] \cos 2\theta_i \right\} \\ & + \frac{a_1 a_2 k_2}{2\alpha_2} [-(1 - \lambda)A_{(-)} + M_{(-)}] \cos(\theta_1 - \theta_2) \\ & + \frac{a_1 a_2 k_2}{2\alpha_2} [(1 + \lambda)A_{(+)} + M_{(+)}] \cos(\theta_1 + \theta_2), \end{aligned} \quad (2.7a)$$

where

$$M_{(\mp)} = \lambda^2 + 1 - \lambda(\Gamma\alpha_1\alpha_2 \pm 1). \quad (2.7b)$$

The Bernoulli constant is found to be

$$C_0 = \sum_{i=1}^2 \frac{a_i^2 k_i}{2} \frac{1}{\sinh 2k_i h}. \quad (2.8)$$

The dynamic pressure, velocity and acceleration components of the conventional perturbation solution can be readily derived from the velocity potential, accurate up to second order, and the related formulations are presented in Appendix A.

2.1.2 The Phase Modulation Solution

Zhang et al. (1993 & 1996a) found that the truncated solution by the conventional perturbation method for the interaction between an unidirectional short wave and a unidirectional long-wave components may not converge, if the two wavelengths are quite different. This convergence difficulty can be overcome using the phase modulation method

(Zhang *et al.* 1993). The phase modulation method was extended to allow for directional waves in deep water by Hong (1993). His results revealed the structure of the solutions for the modulated short-wave phase, amplitude and velocity potential of a short wave modulated by a long wave advancing in a different direction. However, Hong's derivation is mathematically lengthy and complicated with the conformal mapping of different solution domains. To simplify the derivation, developed in this study is a new modulation perturbation analysis with which the solution for the modulated directional short-wave component is obtained directly in the Cartesian coordinates. Furthermore, the present solution is extended to allow for an intermediate-water depth with respect to the long-wave component.

In contrast to the conventional approach, which describes the effects of wave-wave interactions in terms of high order solutions and interprets them as *bound* waves or *forced* waves, the phase modulation approach considers the consequence of wave interactions as the modulation on the short-wave component and thus describes it directly in the solution of the short-wave component. For a directional deep-water short-wave component modulated by an intermediate water-depth long-wave component, we explicitly formulate the modulation in the solutions for the short-wave potential and elevation according to the features discovered by Hong (1993) and then determine the solutions by using the governing equation and boundary conditions. The derivation is described below.

The total potential and surface elevation can be expressed as a superposition of the potentials and elevations of a short-wave and a long-wave components,

$$\Phi = \Phi_1 + \Phi_3, \quad (2.9)$$

$$\zeta = \zeta_1 + \zeta_3, \quad (2.10)$$

where the subscripts 1 and 3 stand for the long-wave and short-wave components, respectively.

The governing equation and boundary conditions for Φ are the same as (2.1)–(2.4) except that the bottom boundary condition for the short-wave component is changed to

$$\nabla \Phi_3 \rightarrow 0 \quad \text{as } z \rightarrow -h, \quad (2.11)$$

because the water depth is deep with respect to the short-wave component.

The effect of the interactions on the long-wave component is known to be at most of third-order in wave steepness (Zhang *et al.* 1993; Hong 1993). Hence, the solution for the long-wave component at the second-order is the same as a single Stokes wave train. By expanding the free surface boundary conditions at the undisturbed long-wave surface and subtracting the undisturbed long-wave surface boundary conditions, we obtain the governing equation and boundary conditions for the short-wave component, correct to the second order in wave steepnesses,

$$\begin{aligned} \nabla^2 \Phi_3 &= 0, & -h \leq z \leq \zeta_1, & \\ \frac{\partial \Phi_3}{\partial t} + g\zeta_3 + \nabla \Phi_1 \cdot \nabla \Phi_3 + \frac{\partial^2 \Phi_1}{\partial t \partial z} \zeta_3 & & & \end{aligned} \quad (2.12)$$

$$+ \frac{1}{2} |\nabla \Phi_3|^2 + \frac{\partial^2 \Phi_3}{\partial t \partial z} \zeta_3 = 0 \quad \text{at } z = \zeta_1, \quad (2.13)$$

$$\begin{aligned} \frac{\partial \zeta_3}{\partial t} - \frac{\partial \Phi_3}{\partial z} + \nabla_h \Phi_1 \cdot \nabla_h \zeta_3 + \nabla_h \Phi_3 \cdot \nabla_h \zeta_1 \\ - \frac{\partial^2 \Phi_1}{\partial z^2} \zeta_3 + \nabla_h \Phi_3 \cdot \nabla_h \zeta_3 - \frac{\partial^2 \Phi_3}{\partial z^2} \zeta_3 = 0 \quad \text{at } z = \zeta_1, \end{aligned} \quad (2.14)$$

$$\nabla \Phi_3 \rightarrow 0 \quad \text{as } z \rightarrow -h, \quad (2.15)$$

where ∇_h is the horizontal gradient operator. The last two terms on the left-hand-sides of (2.13) and (2.14) are of second order and describe the interaction of the short-wave component with itself. Thus, they only contribute to the second harmonic of the short-wave component and consequently can be ignored in the derivation of the modulations of the first harmonic of the short-wave component. The remaining nonlinear terms in (2.13) and (2.14) represent the interaction between the long-wave and short-wave components.

Because the second harmonic of the short-wave component is of the second-order, the modulational effects on the second harmonic are of the third-order. The solution for the second harmonic of short-wave component up to the second-order is the same as a single Stokes wave and its derivation is omitted here for brevity.

From Hong's study (1993), we anticipate that the modulated short-wave component potential and elevation can be expressed as,

$$\Phi_3 = A_3 f_A e^{k_3 f_k} \sin \tilde{\theta}_3, \quad (2.16)$$

$$\zeta_3 = a_3(1 + \varepsilon_1 b \cos \theta_1) \cos \tilde{\tilde{\theta}}_3, \quad (2.17)$$

where

$$f_A = 1 + \varepsilon_1 \tau \cos \theta_1, \quad (2.18a)$$

$$f_k = z - a_1 \cos \theta_1 + \varepsilon_1 z \cos \theta_1 \sum_{j=0}^J \gamma_j (k_1 z)^j, \quad (2.18b)$$

$$\tilde{\theta}_3 = k_{3x}x + k_{3y}y - \sigma_3 t + \delta_3 + k_3 a_1 \sin \theta_1 \sum_{j=0}^{J+1} \rho_j (k_1 z)^j, \quad (2.18c)$$

$$\tilde{\tilde{\theta}}_3 = k_{3x}x + k_{3y}y - \sigma_3 t + \delta_3 + k_3 a_1 \rho_0 \sin \theta_1 + \Delta \varepsilon_1 \sin \theta_1, \quad (2.18d)$$

A_3 is the average potential amplitude of the short-wave component, f_A represents the modulation of the potential amplitude, f_k denotes the effects of the changes of the short-wavenumber and the relative still water level due to the presence of the long-wave component. $\tilde{\theta}_3$ and $\tilde{\tilde{\theta}}_3$ are the modulated phases for the modulated velocity potential and surface elevation, respectively. They are modeled as the sum of the corresponding linear phase and the modulation by the long-wave component, b stands for the modulation of the elevation amplitude and Δ is the phase shift between the elevation phase and the potential phase at the free surface. The parameters, ρ , γ , τ and b , can be further expanded in terms of the frequency ratio of the long-wave to the short-wave component,

λ ,

$$\rho_j = \sum_{n=0}^{2(J+1)-2j} \lambda^n \rho_{jn}, \quad \gamma_j = \sum_{n=0}^{2J-2j} \lambda^n \gamma_{jn}, \quad \tau = \sum_{n=0}^{2J} \lambda^n \tau_n, \quad b = \sum_{n=0}^{2J} \lambda^n b_n, \quad (2.19)$$

where the summation is set to be zero if its upper limit is negative.

Since the phase modulation approach is intended to describe the interactions between short-wave and long-wave components with quite different wavelengths, λ is expected to be relatively small. Generally speaking, it is smaller than 0.5. Theoretically, the summations in (2.18b), (2.18c) and (2.19) can be extended to infinity. But in reality they have to be truncated at a finite order. Equations (2.18b) and (2.18c) involve double summations and the series in both summations converge if $\lambda \ll 1$, because the magnitude of $k_1 z$ also depends on λ . Therefore, to achieve an accuracy at certain order of λ for the solutions of the potential and elevation, the truncations of the summations in (2.18b), (2.18c) and (2.19), have to be made consistently. For example, the truncation of ρ_j in (2.19) depends on the subscripts j and the truncation integer J in the summations of (2.18b) and (2.18c). The reasons are elaborated below.

To ensure the value of the short-wave potential to be nontrivial, the absolute value of its exponential index $k_3 z$ can not be too large. i.e. the index should be of $O(1)$. Because of $k_1/k_3 = \alpha_1 \lambda^2$, we have $|k_1 z| \sim O(\alpha_1 \lambda^2)$. Furthermore, because the water depth is intermediate with respect to the long-wave component, $\alpha_1 \sim O(1)$. Hence, $|k_1 z| \sim O(\lambda^2)$ and $(k_1 z)^j \sim O(\lambda^{2j})$. If ρ_j is truncated at $2(J+1)-2j$, then ρ_{j+1} should be truncated at $2(J+1)-2(j+1)$. As a result, $\rho_j(k_1 z)^j$ and $\rho_{j+1}(k_1 z)^{j+1}$ are accurate up to the same order of magnitude, i.e. $O(\lambda^{2(J+1)})$. Likewise, the truncation in γ_j should be made accordingly. Since τ and b only involve a single summation, to achieve the same accuracy their summations in (2.19) are truncated at $2J$. As a result, the truncated solutions for the short-wave potential and elevation are accurate up to $O(\varepsilon_1 \lambda^{2J})$.

Substituting (2.16) into the Laplace equation (2.12), we obtain

$$\nabla^2 \Phi_3 = E e^{k_3 f_k} \sin \tilde{\theta}_3 \cos \theta_1 \varepsilon_1 k_3^2 + F e^{k_3 f_k} \cos \tilde{\theta}_3 \sin \theta_1 \varepsilon_1 k_3^2 = 0, \quad (2.20)$$

and the coefficients E and F are given by

$$\begin{aligned} E = & -\lambda^4 \alpha_1^2 \tau - 2\Gamma \sum_{j=0}^J \rho_j (k_1 z)^j + \lambda^2 \alpha_1 \left[1 - \sum_{j=0}^J \gamma_j (k_1 z)^{j+1} \right] \\ & + 2 \sum_{j=0}^J (j+1) \gamma_j (k_1 z)^j + \lambda^2 \alpha_1 \sum_{j=0}^{J-1} (j+1)(j+2) \gamma_{j+1} (k_1 z)^j, \end{aligned} \quad (2.21a)$$

$$\begin{aligned} F = & -2\lambda^2 \alpha_1 \Gamma \tau + 2\Gamma \left[1 - \sum_{j=0}^J \gamma_j (k_1 z)^{j+1} \right] - \lambda^2 \alpha_1 \sum_{j=0}^J \rho_j (k_1 z)^j \\ & + 2 \sum_{j=1}^J j \rho_j (k_1 z)^{j-1} + \lambda^2 \alpha_1 \sum_{j=1}^{J-1} j(j+1) \rho_{j+1} (k_1 z)^{j-1}, \end{aligned} \quad (2.21b)$$

where Γ was defined in (2.6d). Splitting (2.20) with respect to $\sin \tilde{\theta}_3$ and $\cos \tilde{\theta}_3$, we have $E = F = 0$, which can be satisfied by further letting all coefficients of the terms, $(k_1 z)^m$, be zero. For $E = 0$, we get the following equations,

$$O(1) : -2\Gamma \rho_0 - \lambda^4 \alpha_1^2 \tau + \lambda^2 \alpha_1 + 2\gamma_0 + 2\lambda^2 \alpha_1 \gamma_1 = 0, \quad (2.22a)$$

$$\begin{aligned} O(k_1^m z^m) : & -2\Gamma \rho_m - \lambda^2 \alpha_1 \gamma_{m-1} + 2(m+1) \gamma_m \\ & + \lambda^2 \alpha_1 (m+1)(m+2) \gamma_{m+1} = 0, \quad m = 1, 2, \dots \end{aligned} \quad (2.22b)$$

Similarly, for $F = 0$,

$$O(1) : 2\Gamma - 2\lambda^2 \alpha_1 \tau \Gamma - \lambda^2 \alpha_1 \rho_0 + 2\rho_1 + 2\lambda^2 \alpha_1 \rho_2 = 0, \quad (2.23a)$$

$$\begin{aligned} O(k_1^m z^m) : & -2\Gamma \gamma_{m-1} - \lambda^2 \alpha_1 \rho_m + 2(m+1) \rho_{m+1} \\ & + \lambda^2 \alpha_1 (m+1)(m+2) \rho_{m+2} = 0, \quad m = 1, 2, \dots \end{aligned} \quad (2.23b)$$

Equations (2.22) and (2.23) can be further expanded in terms of λ . From (2.22a), we

obtain the following hierarchy equations

$$O(1) : -2\Gamma\rho_{00} + 2\gamma_{00} = 0, \quad (2.24a)$$

$$O(\lambda) : -2\Gamma\rho_{01} + 2\gamma_{01} = 0, \quad (2.24b)$$

$$O(\lambda^2) : -2\Gamma\rho_{02} + \alpha_1 + 2\gamma_{02} + 2\alpha_1\gamma_{10} = 0, \quad (2.24c)$$

$$O(\lambda^3) : -2\Gamma\rho_{03} + 2\gamma_{03} + 2\alpha_1\gamma_{11} = 0, \quad (2.24d)$$

$$O(\lambda^n) : -2\Gamma\rho_{0,n} + 2\gamma_{0,n} - \alpha_1^2\tau_{n-4} + 2\alpha_1\gamma_{1,n-2} = 0, \quad n \geq 4. \quad (2.24e)$$

Similarly, (2.22b) can be expanded as, for $m = 1, 2, \dots$,

$$O(1) : -2\Gamma\rho_{m,0} + 2(m+1)\gamma_{m,0} = 0, \quad (2.25a)$$

$$O(\lambda) : -2\Gamma\rho_{m,1} + 2(m+1)\gamma_{m,1} = 0, \quad (2.25b)$$

$$O(\lambda^n) : -2\Gamma\rho_{m,n} - \alpha_1\gamma_{m-1,n-2} + 2(m+1)\gamma_{m,n} \\ + (m+1)(m+2)\alpha_1\gamma_{m+1,n-2} = 0, \quad n \geq 2. \quad (2.25c)$$

In the same way, (2.23a) is further expanded as

$$O(1) : 2\rho_{10} + 2\Gamma = 0, \quad (2.26a)$$

$$O(\lambda) : 2\rho_{11} = 0, \quad (2.26b)$$

$$O(\lambda^n) : 2\rho_{1n} - 2\alpha_1\tau_{n-2}\Gamma - \alpha_1\rho_{0,n-2} + 2\alpha_1\rho_{2,n-2} = 0, \quad n \geq 2. \quad (2.26c)$$

and so does (2.23b) for $m = 1, 2, \dots$

$$O(1) : -2\Gamma\gamma_{m-1,0} + 2(m+1)\rho_{m+1,0} = 0, \quad (2.27a)$$

$$O(\lambda) : -2\Gamma\gamma_{m-1,1} + 2(m+1)\rho_{m+1,1} = 0, \quad (2.27b)$$

$$O(\lambda^n) : -2\Gamma\gamma_{m-1,n} - \alpha_1\rho_{m,n-2} + 2(m+1)\rho_{m+1,n} \\ + (m+1)(m+2)\alpha_1\rho_{m+2,n-2} = 0, \quad n \geq 2. \quad (2.27c)$$

The simultaneous equations (2.24)–(2.27) can be used to express all coefficients of ρ_j and γ_j in terms of $\rho_0(\rho_{00}, \rho_{01}, \dots, \rho_{0n})$, and $\tau(\tau_0, \tau_1, \tau_2, \dots, \tau_n)$. Later, it will be shown that the coefficients ρ_0 and τ can be determined using the free-surface boundary conditions. Thus, the solution for the potential can be obtained. The procedures of expressing the coefficients of ρ_j and γ_j in terms of ρ_0 and τ are detailed below.

To facilitate the description of the procedures, the coefficients ρ_{ij} and γ_{ij} are described as the elements of the matrices ρ and γ , respectively, as in (2.28), where i and j are the row and column numbers of the element, respectively. The i th row elements in ρ and γ matrices belong to the coefficients ρ_i and γ_i , respectively, as shown in (2.19). The description is divided in two parts,

$$\{\rho\} = \begin{pmatrix} \rho_{00} & \rho_{01} & \rho_{02} & \dots & \rho_{0n} \\ \rho_{10} & \rho_{11} & \rho_{12} & \dots & \rho_{1n} \\ \rho_{20} & \rho_{21} & \rho_{22} & \dots & \rho_{2n} \\ \vdots & \vdots & \vdots & \ddots & \vdots \\ \rho_{n0} & \rho_{n1} & \rho_{n2} & \dots & \rho_{nn} \end{pmatrix}, \quad \{\gamma\} = \begin{pmatrix} \gamma_{00} & \gamma_{01} & \gamma_{02} & \dots & \gamma_{0n} \\ \gamma_{10} & \gamma_{11} & \gamma_{12} & \dots & \gamma_{1n} \\ \gamma_{20} & \gamma_{21} & \gamma_{22} & \dots & \gamma_{2n} \\ \vdots & \vdots & \vdots & \ddots & \vdots \\ \gamma_{n0} & \gamma_{n1} & \gamma_{n2} & \dots & \gamma_{nn} \end{pmatrix} \quad (2.28)$$

(a) Noticing that the solutions for ρ_{10} and ρ_{11} are explicitly given by (2.26a) and (2.26b), the solutions for all elements in the first two columns ($j = 0$ and 1) of the matrices ρ and γ can be expressed in terms of ρ_{00} or ρ_{01} (which are the elements of ρ_0) explicitly by solving the simultaneous equations (2.24a), (2.24b), (2.25a), (2.25b), (2.27a) and (2.27b). The results are given below.

$$\rho_{i,j} = \begin{cases} \frac{\rho_{0j}}{i!} \Gamma^i, & i \text{ is even and } i \geq 2, j = 0, 1, \\ -\frac{\Gamma^i}{i!}, & i \text{ is odd and } i \geq 2, j = 0, \\ 0, & i \text{ is odd and } i \geq 2, j = 1. \end{cases} \quad (2.29)$$

$$\gamma_{i,j} = \begin{cases} \frac{\rho_{0j}}{(i+1)!} \Gamma^{i+1}, & i \text{ is even and } 0, i \geq 0, j = 0, 1, \\ -\frac{\Gamma^{i+1}}{(i+1)!}, & i \text{ is odd and } i > 0, j = 0, \\ 0, & i \text{ is odd and } i > 0, j = 1. \end{cases} \quad (2.30)$$

(b) The remaining elements in the matrices ρ and γ are expressed in the recursive relations. There are three rules for obtaining these recursive relations based on the simultaneous equations (2.24c)–(2.24e), (2.25c), (2.26c) and (2.27c). First, an element either ρ_{ij} or γ_{ij} can always be calculated in terms of $\rho_{i'j'}$ and $\gamma_{i'j'}$ if $2i + j > 2i' + j'$. Reminding that the first subscript i implies the corresponding element multiplied by $(k_1 z)^i$ which is of $O(\lambda^{2i})$ and the second subscript j indicates the multiplication of λ^j , the combination of the two subscripts, $2i + j$, indicates the order of λ associated with the corresponding element. Hence, this rule is expected because in a perturbation method the coefficients associated with higher order terms should be solved in terms of coefficients associated with lower order terms. However, there exists a scenario: in each of the above equations there are two elements which belong to the same matrix and whose combinations of the subscripts ($2i + j$) are the same and the largest. Hence, the second rule for deriving the recursive relations is how to decide which of the two elements is treated as an unknown. When the two elements in an equation has the same greatest combined value of the subscripts, i.e. $2i + j = 2i' + j'$, then the element has a greater second subscript j ($j > j'$) is calculated based on the element of a smaller second subscript. The reason why the element with a smaller second subscript j' is always known earlier than the one with a greater second subscript j is because the elements in the first two columns of the matrices (ρ and γ) have already been solved as described in part (a). Therefore, for the elements with the same combined value of the two subscripts, the recursive relations for the elements propagates from the left to the right of the matrix. Finally, as shown in (2.25c), two elements $\rho_{m,n}$ and $\gamma_{m,n}$ have exactly the same subscripts and their combination are the greatest. Thus, the third rule for obtaining the recursive relations is that $\gamma_{m,n}$ is calculated based on the results

of $\rho_{m,n}$. This is because that the calculation of the corresponding $\rho_{m,n}$ can be made without knowing $\gamma_{m,n}$ in advance as indicated by (2.27c).

According to the above three rules, the order for calculating the elements in the matrices ρ and γ is determined and summarized in (2.31). The number at the location of an element indicates the relative order to be calculated in using the recursive relations. For clearness of printing, the corresponding elements are not printed. It should be reminded that the elements in the first row of ρ are treated as known and the elements in the first two columns in both matrices have been solved in (2.29) and (2.30).

$$\{\rho\} = \begin{pmatrix} \rho_{00} & \rho_{01} & \rho_{02} & \rho_{03} & \rho_{04} & \rho_{05} & \rho_{06} & \rho_{07} & \rho_{08} & \dots \\ \rho_{10} & \rho_{11} & (1) & (2) & (4) & (6) & (9) & (12) & (16) & \dots \\ \rho_{20} & \rho_{21} & (3) & (5) & (8) & (11) & (15) & \dots & & \\ \rho_{30} & \rho_{31} & (7) & (10) & (14) & \dots & & & & \\ \rho_{40} & \rho_{41} & (13) & (17) & \dots & & & & & \end{pmatrix}, \quad (2.31a)$$

$$\{\gamma\} = \begin{pmatrix} \gamma_{00} & \gamma_{01} & (1) & (2) & (4) & (6) & (9) & (12) & (16) & (20) & \dots \\ \gamma_{10} & \gamma_{11} & (3) & (5) & (8) & (11) & (15) & (19) & \dots & & \\ \gamma_{20} & \gamma_{21} & (7) & (10) & (14) & (18) & \dots & & & & \\ \gamma_{30} & \gamma_{31} & (13) & (17) & \dots & & & & & & \\ \gamma_{40} & \gamma_{41} & (21) & \dots & & & & & & & \end{pmatrix}. \quad (2.31b)$$

Substituting ζ_3 and Φ_3 into the boundary conditions (2.13) and (2.14) and collecting the terms of the same order in terms of the wave steepness, ε_1 , we obtain the following equations

$$O(1) : A_3 \sigma_3 = a_3 g, \quad (2.32a)$$

$$O(\varepsilon_1) : -A_3 \sigma_3 \tau - A_3 k_3 k_1^{-1} \sigma_1 (\rho_0 - \alpha_1 \Gamma) + a_3 g (b - \alpha_1^{-1}) = 0, \quad (2.32b)$$

$$A_3 \sigma_1 \tau - a_3 g \Delta = 0. \quad (2.32c)$$

$$O(1) : a_3 \sigma_3 = A_3 k_3, \quad (2.33a)$$

$$O(\varepsilon_1) : -A_3 k_3 (\tau + \gamma_0) + a_3 (\sigma_3 b + \sigma_1 \Delta) + a_3 k_3 k_1^{-1} \sigma_1 (\rho_0 - \alpha_1 \Gamma) = 0, \quad (2.33b)$$

$$-A_3 k_3 (\Gamma + \rho_1) + a_3 \sigma_3 \Delta + a_3 \sigma_1 (b - \alpha_1) = 0. \quad (2.33c)$$

where the equations of $O(\varepsilon_1)$ are further split with respect to the factors of $\sin \theta_1$ and $\cos \theta_1$. Equation (2.32a) renders the relationship between the average potential and elevation amplitudes,

$$A_3 = \frac{a_3 g}{\sigma_3}. \quad (2.34)$$

Combining (2.32a) and (2.33a), the linear dispersion relationship is obtained: $\sigma_3^2 = g k_3$. Equation (2.32c) relates the phase shift Δ to τ ,

$$\Delta = \lambda \tau. \quad (2.35)$$

Noticing $\lambda^2 = \alpha_1^{-1} k_1 / k_3$, (2.35) and (2.34), equations (2.32b), (2.33b) and (2.33c) can be reduced to,

$$-\tau - \lambda^{-1} \alpha_1^{-1} \rho_0 + \lambda^{-1} \Gamma + b - \alpha_1^{-1} = 0, \quad (2.36a)$$

$$-\tau - \gamma_0 + b + \alpha_1^{-1} \lambda^{-1} \rho_0 + \lambda^2 \tau - \lambda^{-1} \Gamma = 0, \quad (2.36b)$$

$$-\Gamma - \rho_1 + \lambda \tau + \lambda b - \lambda \alpha_1 = 0. \quad (2.36c)$$

Although the short-wave potential Φ_3 depends on many parameters (ρ_n and γ_n) which are to be determined using the recursive relations in terms of ρ_0 and τ , it is noted that only ρ_0 , ρ_1 and γ_0 appear in the free-surface boundary conditions. Subtracting (2.36a) from (2.36b) and subtracting (2.36c) divided by λ from (2.36b), we eliminate b from the system of equations.

$$-\gamma_0 + \alpha_1^{-1} + 2\alpha_1^{-1} \lambda^{-1} \rho_0 + \lambda^2 \tau - 2\lambda^{-1} \Gamma = 0, \quad (2.37a)$$

$$-2\tau - \gamma_0 + \alpha_1^{-1}\lambda^{-1}\rho_0 + \lambda^{-1}\rho_1 + \alpha_1 + \lambda^2\tau = 0. \quad (2.37b)$$

Since γ_0 and ρ_1 can be calculated in terms of ρ_0 and τ using the recursive relations resulting from the Laplace equation as described earlier, there are only two unknowns τ and ρ_0 in (2.37) and hence they can be solved exactly. The procedures are briefly described below.

Equations (2.37a) and (2.37b) can be further perturbed in terms of λ . From (2.37a), we have the following set of equations,

$$O(\lambda^{-1}) : \rho_{00} = \Gamma\alpha_1, \quad (2.38a)$$

$$O(\lambda^0) : \rho_{01} = \frac{1}{2}(\alpha_1\gamma_{00} - 1), \quad (2.38b)$$

$$O(\lambda) : \rho_{02} = \frac{1}{2}\alpha_1\gamma_{01}, \quad (2.38c)$$

$$O(\lambda^n) : \rho_{0n+1} = \frac{\alpha_1}{2}(\gamma_{0n} - \tau_{n-2}), \quad n \geq 2. \quad (2.38d)$$

Similarly, equation (2.37b) can be perturbed into the following set of equations,

$$O(\lambda^{-1}) : \rho_{00} = -\alpha_1\rho_{10} = \alpha_1\Gamma, \quad (2.39a)$$

$$O(\lambda^0) : \tau_0 = \frac{1}{2}(\alpha_1^{-1}\rho_{01} + \rho_{11} - \gamma_{00} + \alpha_1), \quad (2.39b)$$

$$O(\lambda) : \tau_1 = \frac{1}{2}(\alpha_1^{-1}\rho_{02} + \rho_{12} - \gamma_{01}), \quad (2.39c)$$

$$O(\lambda^n) : \tau_n = \frac{1}{2}(\alpha_1^{-1}\rho_{0n+1} + \rho_{1n+1} - \gamma_{0n} - \tau_{0n-2}), \quad n \geq 2. \quad (2.39d)$$

Noticing $\gamma_{00} = \Gamma\rho_{00} = \Gamma^2\alpha_1$ from (2.24a) and (2.39a), ρ_{01} can be calculated from (2.38b). Because ρ_{00} and ρ_{01} are known, the coefficients γ_{ij} ($j = 0, 1$) and ρ_{ij} ($j = 0, 1; i \geq 2$) can be obtained using the recursive relations shown in (2.29) and (2.30). Then ρ_{02} and τ_0 can be calculated as shown in (2.38c) and (2.39b). Based on the recursive relation (2.26c), we obtain

$$\rho_{12} = \alpha_1 \left(\Gamma\tau_0 + \frac{1}{2}\rho_{00} - \rho_{20} \right). \quad (2.40)$$

Then τ_1 can be calculated from (2.39c). The solutions for ρ_{0n+1} and τ_n for $n \geq 2$ can be alternatively obtained from lower to higher n using (2.38d) and (2.39d). In the computation, γ_{0n} and ρ_{1n+1} are computed using the recursive relations described earlier. The solutions for ρ_{ij} ($i \geq 2; j \geq 2$) and γ_{ij} ($j \geq 1$) can also be calculated using the recursive relations. Substituting ρ_{0n} and τ_n ($n = 0, 1, \dots$) into (2.36a), b_n ($n = 0, 1, \dots$) can be calculated.

The final solutions for ρ , γ , τ , and b are presented in Appendix B. The potential and elevation of the modulated first-harmonic short-wave components can be readily obtained from (2.16), (2.17) and (2.18) after ρ , γ , τ , and b have been evaluated. The modulated dynamic pressure, velocity and acceleration can be derived from the modulated potential and are presented in Appendix C.

2.1.3 The Hybrid Wave Model Solution

When applying the hybrid wave model to an ocean wave field, its spectrum is usually divided into three regions: pre-long, powerful and restriction regions from low to high frequency as sketched in Figure 2.1. The powerful region involves all free-wave components with relatively significant wave energy and is further divided into four bands, i.e. long-wave band one (L1) and two (L2) and short-wave band 1 (S1) and 2 (S2), starting from low to high in the frequency domain. For most ocean wave fields, the spectral peak is usually inside the band L1. The amplitudes and especially the wave steepnesses of the free-wave components in the pre-long wave region are very small. Hence, the interaction of a free-wave component in the pre-long wave region with any free-wave components is insignificant and hence neglected. It is also assumed that the wave components in the restriction region are mainly the bound-wave components resulting from the interactions among the free-wave components in the wave bands of L1, L2, S1 and S2. Therefore, the cut-off frequency for the free-wave components is that at the end of S2.

Two free-wave components located in the same frequency band or in neighboring

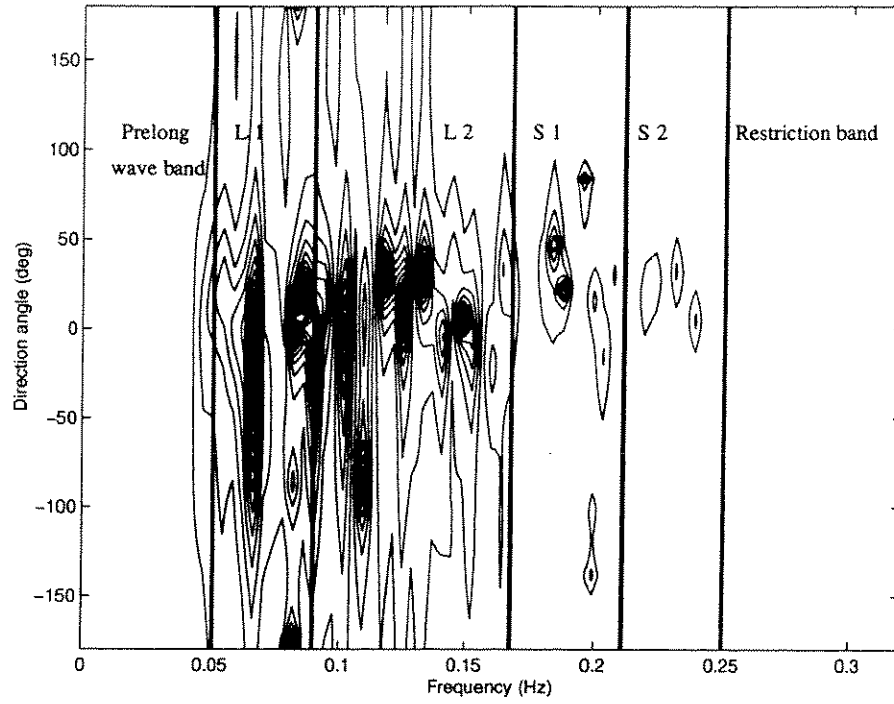


Figure 2.1: Band division of directional hybrid wave model.

bands are relatively close in the frequency domain and hence the interactions between them are calculated using the conventional perturbation approach. While two free-wave components located in two different bands separated by at least one other band are relatively far apart in the frequency domain and, therefore, are calculated using the phase modulation approach. For simplicity of illustration, we assume that a frequency spectrum for an irregular wave field is divided into three wave bands, say, two long-wave bands (L1 and L2) and one short-wave band (S1), in describing the solution for a wave field of multiple free-wave components. It is straightforward to extend the solution to a wave field consisting of more than three wave bands. Following the earlier discussion, the interactions between the free-wave components in L1 and L2 are calculated using the conventional perturbation method, likewise, for the interactions between the free-wave components in L2 and S1, respectively, and between the free-wave components in S1. However, the interactions between the two free-wave components located respectively in

L1 and S1 are computed using the phase modulation method.

Assuming there are M_1 and M_2 frequency increments in L1 and L2, and N frequency increments in S1, respectively, and there is only one free-wave component at each frequency, the total velocity potential of a directional wave field can be written as

$$\Phi = \Phi_{L1} + \Phi_{L2} + \Phi_{S1L1} + \Phi_{S1L2} + \Phi_{SS}, \quad (2.41)$$

in which Φ_{L1} and Φ_{L2} are the resultant total potentials, including the potentials of all free-wave components in L1 and L2, and the nonlinear interactions between them, Φ_{S1L1} is the modulated short-wave potentials by L1 in S1, Φ_{S1L2} is the resultant potential resulting from the nonlinear interactions between L2 and S1, Φ_{SS} is the resultant short-wave potential from interactions between the free-wave components in S1. These potential can be calculated by:

$$\begin{aligned} \Phi_{L1} + \Phi_{L2} = & \sum_{j=1}^M \left\{ \frac{a_j g}{\sigma_j} \frac{\cosh[k_j(z+h)]}{\cosh(k_j h)} \sin \theta_j + \frac{3}{8} \frac{a_j^2 \sigma_j \cosh[2k_j(z+h)]}{\sinh^4(k_j h)} \sin(2\theta_j) \right\} \\ & + \sum_{j=2}^M \sum_{i=1}^{j-1} \left\{ \frac{a_i a_j \sigma_j}{2} A_{j-i} \frac{\cosh[|\mathbf{k}_j - \mathbf{k}_i|(z+h)]}{\cosh(|\mathbf{k}_j - \mathbf{k}_i|h)} \sin(\theta_j - \theta_i) \right. \\ & \left. + \frac{a_i a_j \sigma_j}{2} A_{j+i} \frac{\cosh[|\mathbf{k}_j + \mathbf{k}_i|(z+h)]}{\cosh(|\mathbf{k}_j + \mathbf{k}_i|h)} \sin(\theta_j + \theta_i) \right\}, \end{aligned} \quad (2.42)$$

where $M = M_1 + M_2$, A_{j-i} and A_{j+i} are the same as $A_{(-)}$ and $A_{(+)}$ given in (2.6a) except that the subscripts 1 and 2 are replaced by i and j , respectively.

$$\Phi_{S1L1} = \sum_{j=M+1}^{M+N} \Phi_j, \quad (2.43)$$

where Φ_j is determined in the same way as Φ_3 in (2.16) except that the modulation factors f_A and f_k , and the modulated phase $\bar{\theta}_j$ need to be extended to allow for the

modulation by multiple long-wave components in L1,

$$f_{A_j} = 1 + \sum_{i=1}^{M_1} \varepsilon_i \tau_{ij} \cos \theta_i, \quad (2.44)$$

$$f_{k_j} = z - \sum_{i=1}^{M_1} \left\{ a_i \cos \theta_i + \varepsilon_i z \cos \theta_i \left[\sum_{l=0}^J \gamma_{lij} (k_i z)^l \right] \right\}, \quad (2.45)$$

$$\tilde{\theta}_j = k_{jx} x + k_{jy} y - \sigma_j t + \delta_j + \sum_{i=1}^{M_1} \left[k_j a_i \sin \theta_i \sum_{l=0}^J \rho_{lij} (k_l z)^l \right], \quad (2.46)$$

where the subscripts of i and j stand for i th long-wave component and j th short-wave component, respectively.

$$\begin{aligned} \Phi_{S1L2} + \Phi_{SS} = & \sum_{j=M+1}^{M+N} \frac{3}{8} \frac{a_j^2 \sigma_j \cosh[2k_j(z+h)]}{\sinh^4(k_j h)} \sin(2\theta_j) + \left(\sum_{j=M+2}^{M+N} \sum_{i=M+1}^{j-1} + \sum_{j=M_1+1}^M \sum_{i=M+1}^{M+N} \right) \\ & \left\{ \frac{a_i a_j \sigma_j}{2} A_{j-i} \frac{\cosh[|\mathbf{k}_j - \mathbf{k}_i|(z+h)]}{\cosh(|\mathbf{k}_j - \mathbf{k}_i|h)} \sin(\theta_j - \theta_i) \right. \\ & \left. + \frac{a_i a_j \sigma_j}{2} A_{i+j} \frac{\cosh[|\mathbf{k}_j + \mathbf{k}_i|(z+h)]}{\cosh(|\mathbf{k}_j + \mathbf{k}_i|h)} \sin(\theta_j + \theta_i) \right\}. \end{aligned} \quad (2.47)$$

Similarly, we can express the surface elevation ζ as

$$\zeta = \zeta_{L1} + \zeta_{L2} + \zeta_{S1L1} + \zeta_{S1L2} + \zeta_{SS}, \quad (2.48)$$

where the right-hand-side terms are corresponding to the potentials with the same subscripts in (2.41).

$$\begin{aligned} \zeta_{L1} + \zeta_{L2} = & \sum_{j=1}^M a_j \cos \theta_j \\ & + \sum_{j=1}^M \frac{a_j^2 \sigma_j^2}{4g} \left[2 + \frac{3 \cosh(2k_j h)}{\sinh^4(k_j h)} - \frac{1}{\sinh^2(k_j h)} \right] \cos 2\theta_j \\ & + \sum_{j=2}^M \sum_{i=1}^{j-1} \left\{ \frac{a_i a_j k_j}{2\alpha_j} [-(1-\lambda)A_{j-i} + M_{j-i}] \cos(\theta_j - \theta_i) \right. \\ & \left. + \frac{a_i a_j k_j}{2\alpha_j} [(1+\lambda)A_{i+j} + M_{i+j}] \cos(\theta_i + \theta_j) \right\}. \end{aligned} \quad (2.49)$$

$$\zeta_{S1L1} = \sum_{j=M+1}^{M+N} a_j (1 + \sum_{i=1}^{M_1} \varepsilon_i b_{ji} \cos \theta_i) \cos \tilde{\theta}_j, \quad (2.50)$$

where b_{ji} is the value b for j th short-wave component modulated by i th long-wave component and

$$\tilde{\theta}_j = k_{jx}x + k_{jy}y - \sigma_j t + \delta_j + \sum_{i=1}^M k_j a_i \rho_{0ij} \sin \theta_i + \sum_{i=1}^M \varepsilon_i \Delta_{ij} \sin \theta_i, \quad (2.51)$$

in which ρ_{0ij} and Δ_{ij} are the coefficients ρ_0 and Δ of j th short-wave component modulated by i th long-wave component, respectively.

$$\begin{aligned} \zeta_{S1L2} + \zeta_{SS} = & \sum_{j=1}^N \frac{a_j^2 k_j}{2} \cos 2\theta_j + \left(\sum_{j=M+2}^{M+N} \sum_{i=M+1}^{j-1} + \sum_{j=M_1+1}^M \sum_{i=M+1}^{M+N} \right) \\ & \times \left\{ \frac{a_i a_j k_j}{2\alpha_j} [-(1-\lambda)A_{j-i} + M_{j-i}] \cos(\theta_j - \theta_i) \right. \\ & \left. + \frac{a_i a_j k_j}{2\alpha_j} [(1+\lambda)A_{i+j} + M_{i+j}] \cos(\theta_i + \theta_j) \right\}. \end{aligned} \quad (2.52)$$

The hybrid wave model solutions for pressure, velocity and acceleration can be readily derived from the velocity potential, and are presented in the Appendix C.

2.2 Directional Decomposition

2.2.1 Estimation of Directional Energy Spreading

Wave directionality is an important property of short-crested ocean waves. A wavenumber-frequency energy spectrum S is defined as a function of wavenumber k and frequency σ , $S = S(k, \sigma)$, which is also known as a three-dimensional Fourier spectrum or a conditional spectrum (Irani *et al.* 1986). If the dispersion relation is invoked, a wavenumber-frequency spectrum reduces to a directional spectrum or a two-dimensional Fourier spectrum, which describes wave energy distribution as a function of wave propagation direction β and frequency.

Many methods have been developed for resolving wave directionality. But, since the initial multidirectional measurements and analysis in the 50's (Chase *et al.* 1957) no method for the analysis of multidirectional seas has been universally accepted (van Heteren *et al.* 1988, Herbers & Guza 1990, Brissette & Tsanis 1994, Goda 1994). As pointed out by Herbers & Guza (1990), the fidelity of physically plausible directional spectrum estimates that are consistent with the observations is often not limited by the estimation technique but by the resolving power of measured array data, which depend on the number of measuring instruments and their layout. In practice, the resolution of the instrument array is often limited because the *in situ* instruments are always sparse; and the statistical uncertainty in the data is significant because of the limited duration of stationary conditions. However, two methods, Maximum Likelihood Method (MLM) and Maximum Entropy Method (MEM), are most widely used because of their relatively high resolution power for estimating the directional wave spectrum and their flexibility. Both of these two methods have been extended to be applicable to multiple array data of different wave properties, and are named as Extended Maximum Likelihood Method (EMLM) (Isobe *et al.* 1984) and Extended Maximum Entropy Method (EMEM) (Hashimoto *et al.* 1994), respectively. Although EMEM can detect partially reflected waves more accurately by resorting to additional physical constraints than EMLM does, the latter is much less intensive in computing than the former and has the same resolution power as the former in most scenarios. Therefore, the EMLM developed by Isobe *et al.* (1984) is employed in this study to estimate the directional spectrum of a measured wave field.

2.2.2 The Extended Maximum Likelihood Method

According to linear wave theory, the Fourier transform of a wave property, F , at the location m can be expressed as

$$F_m(\sigma) = \sum_j H_m(\sigma, \beta_j, h, z_m) e^{-i\mathbf{k}_j \cdot \mathbf{x}_m} Z(\sigma, \beta_j), \quad (2.53)$$

where β_j is the directional angle of the j th wave component at the frequency σ , H_m is a linear transfer function of relating the wave amplitude to the wave property F and depends on the frequency, wave direction, water depth h and vertical coordinate of the location, z_m . \mathbf{k}_j is the wave number vector of the j th wave component, $\mathbf{k}_j = (k_j \cos \beta_j, k_j \sin \beta_j)$. $\mathbf{x}_m = (x_m, y_m)$ denotes the horizontal coordinates of the location, and $Z(\sigma, \beta_j)$ is the complex amplitude of the wave component.

The cross-spectrum for two different wave properties recorded respectively at locations m and n is defined as,

$$C_{mn}(\sigma) = \langle F_m \cdot F_n^* \rangle = \sum_j H_m e^{-i\mathbf{k}_j \cdot \mathbf{x}_m} H_n^* e^{i\mathbf{k}_j \cdot \mathbf{x}_n} S(\sigma, \beta_j), \quad (2.54)$$

where $\langle \rangle$ and the superscript $*$ denote the ensemble mean and the complex conjugate, respectively, and the directional wave spectrum is

$$S(\sigma, \beta_j) = \langle Z(\sigma, \beta_j) \cdot Z^*(\sigma, \beta_j) \rangle. \quad (2.55)$$

In (2.54), it is assumed that

$$\langle Z(\sigma, \beta_j) \cdot Z^*(\sigma, \beta_{j'}) \rangle = 0 \quad \text{for } j \neq j', \quad (2.56)$$

because Z is a random variable (Isobe *et al.* 1984). Therefore, a cross-spectrum matrix $\{C(\sigma)\}$ of size $(M \times M)$ can be formed from M distinct measurements as shown in (2.54). Inverting the cross-spectrum matrix by the MLM. Isobe *et al.* (1984) found that the directional wave spectrum can be estimated as

$$S(\sigma, \beta_j) = \frac{\Lambda}{Q^{*T}(\sigma, \beta_j) \{C(\sigma)\}^{-1} Q(\sigma, \beta_j)}, \quad (2.57a)$$

with

$$\Lambda = \frac{C_{ll}(\sigma)}{\sum_j \left\{ 1 / \left[Q^{*T}(\sigma, \beta_j) \{ C(\sigma) \}^{-1} Q(\sigma, \beta_j) \right] \right\}}, \quad (2.57b)$$

where the superscript T and -1 denote the transpose and inverse of a matrix, respectively, Q is a vector of length M and $\{Q(\sigma, \beta_j)\}_m = H_m(\sigma, \beta_j, h, z) e^{-i\mathbf{k}_j \cdot \mathbf{x}_m}$, $C_{ll}(\sigma)$ is the power spectrum of wave elevation measured at location l .

In this study the directional resolution of EMLM is set to four degrees, i.e. $\Delta\beta = \beta_{j+1} - \beta_j = 4^\circ$, which gives ninety directional components per frequency. The number of discrete frequencies is determined by the duration of the time-series and the cutoff frequency. To reduce the computation time, a limited number of discrete directional wave components at each frequency are used, based on the computed directional amplitude spectrum. For narrow directional wave energy spreading, one directional wave component for each frequency might be adequate. While for broad directional wave energy spreading, more than one directional components at each frequency are employed to represent the spreading. Hence, the number of directional wave components to be used at each frequency depends on the directional spreading of the measured ocean waves. After the number of directional wave components at each frequency is determined, the wave amplitudes are rescaled to conserve the total energy of the spectrum. The details of reducing the number of discrete directional wave components at each frequency will be described in § 3.

2.3 Determining Initial Phases

Wave phase information plays a very important role in recovering and predicting the properties of ocean waves in the time-domain. Wave phases are the fingerprints of the ocean wave process and uniquely determine the events described in wave data. For unidirectional waves, the initial phases can be determined by the FFT. While, for multidirectional waves, the initial phase information is eliminated due to the use of the

cross-spectra during the directional decomposition. Therefore, the initial phases need to be recovered after the directional wave spectrum is obtained.

In this study, a least square phase fitting method is employed to determine the initial phases of free-wave components. The initial phases of the free-wave components at each frequency are determined by minimizing a target function at this frequency. The target function is defined as

$$R_n = \sum_{j=1}^J \left(\frac{\Delta_{jn}}{H_j} \right)^* \left(\frac{\Delta_{jn}}{H_j} \right), \quad (2.58a)$$

$$\Delta_{jn} = \sum_{m=1}^M H_j a_{nm} e^{i(\mathbf{k}_{nm} \cdot \mathbf{x}_j + \epsilon_{nm})} - E_{jn} e^{i\phi_{jn}} + \mathcal{E}_{jn}, \quad (2.58b)$$

where Δ_{jn} is the difference between the recovering property, i.e. the superposition of computed linear and nonlinear results, and the corresponding measurement of n th frequency at the j th sensor. J is the total number of sensors whose measurements are used in the decomposition and M the total number of the free-wave components used at n th frequency. H_j is the transfer function at j th sensor, and a_{nm} , \mathbf{k}_{nm} , and ϵ_{nm} are the amplitude, wave number vector and initial phase of the m th free-wave component at n th frequency, respectively. \mathbf{x}_j is the horizontal coordinates vector of the j th sensor. E_{jn} and ϕ_{jn} are the measured Fourier modulus and phase at n th frequency of the j th sensor, respectively. \mathcal{E}_{jn} is the second-order nonlinear wave-wave interaction effect of n th frequency at the j th sensor, and can be calculated using the hybrid wave model in § 2.1 based on the free-wave components. Minimization of R_n is carried out by using the Polak-Ribiere conjugate gradient minimization procedure at each frequency. (Press et al. 1992). In the first iteration \mathcal{E}_{jn} is unknown, thus set to zero.

3 Numerical Schemes

The measured wave properties are actually the results of superposition of free-wave components and their nonlinear interaction contribution. As discussed in § 2, to decouple the nonlinear wave-wave interaction effects from the measured signals, the free-wave components have to be known. While only after the nonlinear effects are decoupled from the measurements can the free-wave components be obtained. Therefore, the numerical realization of the deterministic hybrid wave model has to be iterative. The schematic flow chart of the numerical procedure is shown in Figure 3.1.

First, the EMLM is used to determine the wave energy distribution as a function of the direction at each discretized frequency based upon the input measurements. Since the EMLM does not retain the initial phases of free-wave components, the initial phases are recovered by fitting the prediction with the input data. Once the spectrum and initial phases are obtained, the effects of the nonlinear interaction among free-wave (linear) components are computed and subtracted from the resultant wave properties, i.e. measurements. At the first iteration the measurements are used as the input for the directional decomposition. After that, the input to the EMLM is the modified measurements with the nonlinear wave effects being decoupled. At each iteration, the free-wave components are recomputed using the EMLM and the phase fitting, and then the nonlinear effects are updated using the formulas described in § 2.1.3. The differences of the nonlinear effects between the two sequential iterations are examined. If the differences are smaller than a prescribed tolerance error, the decomposed free-wave components are accepted and the iteration terminated. Otherwise, the input measurements are remodified and the iteration continues.

Three major steps in the wave decomposition: selection of representative directional free-wave components, initial phase computation, and decoupling of the nonlinear effects of wave interactions from measurements are detailed below.

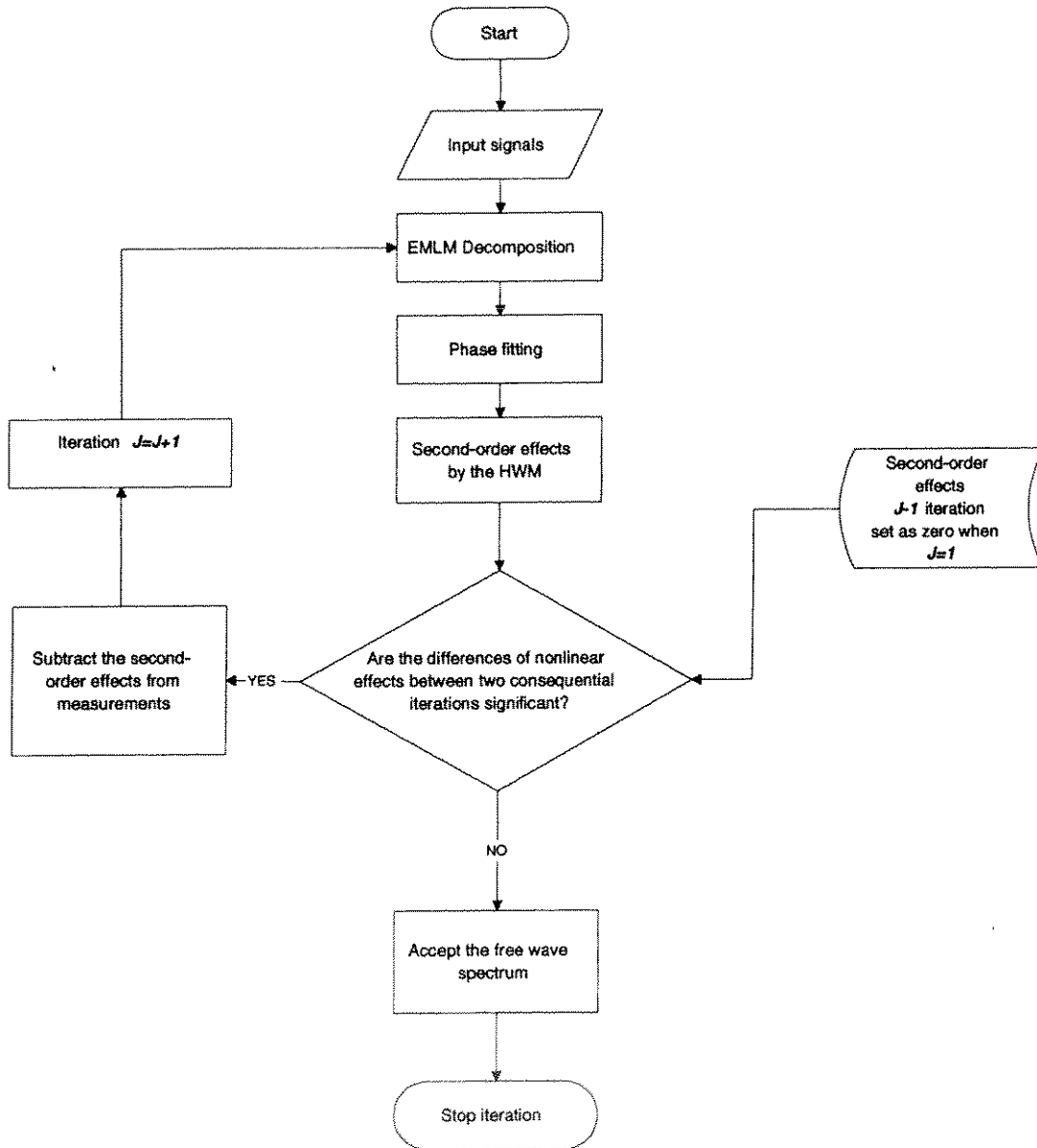


Figure 3.1: Flowchart of the numerical scheme.

3.1 Selection of Representative Directional Free-Wave Components

As discussed in §2, the directional resolution is set to four degrees for the EMLM decomposition in this study. Therefore, there are 90 directional wave components at each frequency. The number of discrete frequencies is determined by the length of the time series as well as the cutoff frequency. In this study we only use a small number of directional wave components, say 1, 3 or 5, at each frequency for computational efficiency. The computation time is roughly proportional to the square of the number of directional wave components at each frequency.

Given the directional energy spreading, the component with the largest amplitude at each frequency, defined as the most energetic component, can be identified and its propagation direction is taken as the main direction of wave propagation at this frequency. If just one component is considered at each frequency, its direction is the same as the most energetic component. In order to conserve the energy, the amplitude of the representative component must be rescaled. The rescale factor is given by

$$\mu = \sqrt{\frac{\sum_{i=1}^M A_i^2}{A_{max}^2}}, \quad (3.1)$$

where A_i and A_{max} are the amplitudes of the i th directional free-wave component and the most energetic free-wave component, respectively, at this frequency, M is the number of directional wave components at each frequency, $M = 90$ in this study. The amplitude of the representative free-wave component at this frequency is μA_{max} .

When the directional spreading is narrow, one component at each frequency is a good approximation. While the directional spreading is wide, more components at each frequency should be used to achieve a better approximation. The criteria of determining how many free-wave components should be used at each frequency is elaborated below.

The square root of the normalized second directional angle moment is defined as, at each frequency,

$$\Pi = \sqrt{\frac{\sum_{i=1}^M [A_i(\beta_i - \beta_0)]^2}{\sum_{i=1}^M A_i^2}}, \quad (3.2)$$

where β_i and β_0 are the directional angles of i th directional free-wave component and the most energetic free-wave component, respectively, at the frequency. If there is only one directional wave component at the frequency, the second moment is zero. If the energy spreading is uniformly distributed in all directions, the second moment is $2\pi/3$. The value of Π defined in (3.2) indicates the extent of directional spreading. When it is relatively small, the wave field at this frequency has a narrow directional spreading. While Π is large, it has a relatively wide spreading.

When the directional spreading is wide, more than one free-wave components at each frequency are selected to represent the directional spreading. The angular moments are also employed to determine the directions of the free-wave components in addition to the most energetic component at each frequency. For the purpose of computation, the index of the M free-wave components at each frequency resulting from the directional decomposition is shifted so that the index of the most energetic wave component is $M/2 + 1$ and each one half of the amplitude of the wave component in the opposite direction of the most energetic component is placed at $j = 1$ and $j = M + 1$, respectively. Hence, there are equally $M/2$ wave components at both sides of the most energetic free-wave component. For simplicity, we only show the procedure of selecting N free-wave components at the left-hand-side of the most energetic free-wave component. The procedure for those at the right-hand-side is virtually identical.

The normalized first and second angular moments M_1 and M_2 are defined as

$$M_1 = \frac{\sum_{j=1}^{M/2} A_j^2 (\beta_j - \beta_0)}{\sum_{j=1}^{M/2} A_j^2}, \quad (3.3)$$

$$M_2 = \frac{\sum_{j=1}^{M/2} A_j^2 (\beta_j - \beta_0)^2}{\sum_{j=1}^{M/2} A_j^2}, \quad (3.4)$$

where A_j and β_j are the amplitude and directional angle of the j th component at the left-hand-side of the most energetic component, respectively. The ratio, M_2/M_1 , is chosen as the direction of the leftmost representative free-wave component. If $N > 1$, the directional angles of the remaining $N - 1$ representative directional wave components are evenly distributed between the angles of the leftmost component and most energetic component. Because of the discrete angles used in the computation, the direction is rounded for the selected component.

Once all the directions of $2N + 1$ representative components have been determined, their amplitudes are rescaled, i.e. multiplied by a factor μ , to conserve the energy at this frequency. The rescale factor is

$$\mu = \sqrt{\frac{\sum_{i=1}^{M+1} A_i^2}{\sum_{m=1}^{2N+1} B_m^2}}, \quad (3.5)$$

where B_m is a subset of A_i , and is defined by $B_m = A_i$ where B_m is in the same direction as A_i .

3.2 Initial Phase Fitting

The initial phases of free-wave components are computed after their amplitudes and directions have been obtained. As discussed in §2.3, the initial phase is determined by minimizing the target function at each frequency, which is the difference between the measurements and the corresponding predictions. The prediction is the sum of free-wave components and their second-order nonlinear interactions. Assuming that the number of wave measurements is J and the number of wave components is N at each frequency, we have $2J$ real equations to solve for N unknown phases. The minimum number of measurements used as input is three. For flexibility, N is not required to be equal to $2J$. Therefore, the set of simultaneous equations may be an over-determined problem if $2J > N$. Hence, a least square approach is employed to solve for the initial phases by minimizing the target function. The minimization is performed by systematically varying the magnitudes of the initial phases in a multi-dimensional space of dimension N . The search for the approximate solutions of the initial phases is accomplished when the target function is smaller than a preset error tolerance. The computation is accelerated using a conjugate gradient minimization algorithm, known as the Fletcher-Reeves-Polak-Ribiere method (Press *et al.* 1992).

3.3 Decoupling Nonlinear Effects

Once the amplitudes, directions and initial phases of the free-wave components are obtained, we can compute the nonlinear interaction effects at the locations where the measurements are used as input. As discussed in §2.1.3, the spectrum are divided into several bands and the wave interactions among these bands are computed according to the hybrid wave model. Although the interactions of the pre-long wave range or restrictive range with other bands are neglected because they are not significant, the difference- and sum-frequency type interactions of the long-wave bands and short-wave bands can have their effects in these two frequency ranges and hence these effects are

subtracted from the measurements. Thus the free-wave components in the pre-long wave range may be quite different from the corresponding ones obtained directly from the FFT of the measurements. The criteria of the division of the wave bands is similar to that described by Zhang *et al.* (1996a) and is not repeated here.

As it is known that the modulation of a short wave by a long wave is significant and the influence of the short wave on the long wave is at least one order higher (Zhang *et al.* 1993), the decoupling of the nonlinear effects is performed in the order from the longer wave band to the shorter wave band. In conjunction with the hybrid wave model, the potential and elevation of wave components in the long- and short-wave bands are formulated differently. Consequently, the decoupling procedures are different in different wave bands.

The conventional perturbation method is used to compute the nonlinear interactions between two free-wave components located inside the same band or in the neighboring bands. The result of nonlinear effects is obtained in the frequency domain. The amplitude and phase spectra from the Fourier transform are converted to cos and sin spectra a_j^c and a_j^s to facilitate the computation, i.e.

$$a_j \cos(\mathbf{k}_j \cdot \mathbf{x} - \sigma t + \beta_j) = a_j^c \cos(\sigma t) + a_j^s \sin(\sigma t), \quad (3.6)$$

where

$$a_j^c = a_j \cos(\mathbf{k}_j \cdot \mathbf{x} + \beta_j), \quad (3.7a)$$

$$a_j^s = a_j \sin(\mathbf{k}_j \cdot \mathbf{x} + \beta_j), \quad (3.7b)$$

and thus a_j^c and a_j^s can have negative values. The nonlinear contributions are directly subtracted from the cos and sin spectra of the measurements.

The phase modulation method is employed to compute the interaction between the free-wave components located in two different bands separated by at least one other band.

The modulation of each short-wave components is calculated in the time domain using the equations described in § 2.1.3. There are two approaches to decouple the nonlinear effects due to the modulation of short free-wave components from the measurements. When the DHWM uses a single free-wave component at each frequency, the decouple process is virtually identical to that described in Zhang *et al.* (1996a). The modulation of the short-wave components by the long-wave components is transferred to the frequency domain from the time domain using the FFT. The unmodulated free-wave components in a short-wave band are then obtained by solving a set of simultaneous equations in the frequency domain, $[C]\{A_f\} = \{A_R\}$. The coefficient matrix, $[C]$, of the simultaneous equations is determined by the long-wave components which modulate the short-wave components, and the coefficient vector, $\{A_R\}$, at the right-hand-side of the equations is the modified measurement in the frequency range of the short-wave band. The nonlinear effects due to interactions between long-wave components have already been subtracted in the modified measurements. Detailed description about the algorithm of computing the coefficient matrix can be found in Zhang *et al.* (1996a). After the free-wave components in the short-wave band, $\{A_f\}$, are calculated, the modulation effects in the frequency domain outside the frequency range of the corresponding short-wave band are computed and subtracted from the resultant wave spectra. Furthermore, the second harmonics and the interaction between the free-wave components within the same short-wave band are calculated and decoupled from the resultant wave spectra. However, when multiple free-wave components are used at each frequency, the above decoupling method can not be directly applied. An alternative method of decoupling the nonlinear effects due to the modulation of short-wave components is to directly subtract them from the measurement in the time domain. The differences between the elevations (or other measured wave characteristics) of modulated short-wave components and the corresponding unmodulated components are viewed as the nonlinear effects due to the modulation by long-wave components. They can be calculated for given free long-wave and short-wave components and subtracted from the measurements. It is observed that

the two approaches render almost identical results in the cases of one free-wave component at each frequency.

After the nonlinear effects are decoupled from the measurements, the modified measurements are used as input for the computation at the next iteration. The three major steps: (a) linear directional decomposition using the EMLM and selecting the representative directional free-wave components, (b) initial phase fitting and (c) decoupling of nonlinear effects are sequentially carried out at each iteration. At the end of each iteration, the newly computed nonlinear effects are compared with those of the previous iteration. The iteration terminates, when the differences between the nonlinear effects of sequential iterations are smaller than a prescribed error tolerance.

4 Numerical Verifications

In this section, numerical verification of the DHWM is conducted to ensure that the present model is theoretically and numerically reliable and convergent. Firstly, the consistence and difference between the conventional perturbation solution and the phase modulation solution are examined. Then, the numerical accuracy and convergence of the DHWM are compared with already established unidirectional Hybrid Wave Model (HWM) in the case of unidirectional irregular waves. Finally, the DHWM is verified against two sets of synthetic data, i.e. firstly, the DHWM is used to predict the simulated wave fields with each set of synthetic free-wave components as its input, and then the predicted wave fields are decomposed by the DHWM and the resultant free-wave components are compared with the corresponding synthetic free-wave components.

4.1 Consistency and Difference between Conventional and Phase Modulation Approaches

As discussed in § 2, the phase modulation approach is complementary to the conventional perturbation approach. When $\varepsilon_1 \ll \varepsilon_l < 0.5$, the phase modulation solution is identical to the conventional perturbation solution. To numerically verify this point, dual free-wave components are considered with the frequencies of the long- and short-wave components being 0.1328 Hz and 0.2148 Hz, respectively. The water depth is set to be 145.0 m, which is intermediate water depth for the long wave and relatively deep with respect to the short wave. The wave length ratio of the short to long wave, ε_l , is 0.3822. The wave steepness of the long-wave component, ε_1 , is 0.10. The amplitude of the short-wave component is 0.5382 m and the steepness 0.10. The direction angles of the long- and short-wave components are 0 and 30 degrees, respectively. Both conventional and phase modulation approaches are used to predict the surface elevation at the horizontal position (-11.6 m, 0 m). Velocity and acceleration components are also

predicted at the same horizontal location but 3.0 m below the still water level. Figure 4.1 shows that the time-series of the surface elevation, x -direction horizontal velocity and vertical acceleration predicted by these two approaches are almost identical. Figure 4.2 presents the predicted x -direction horizontal velocity under the long-wave crest as a function of depth. The predictions of both approaches are in excellent agreement. The small discrepancy is attributed to the implicit inclusion of third-order effects in the phase modulation solution. The consistency of these two methods indicates that the results of the DHWM is not sensitive to the band division.

However, when ε_1 approaches ε_l , i.e. the long-wave component is very steep and the short-wave component is much shorter than the long-wave component in wavelength, the conventional perturbation solution may diverge while the phase modulation solution remains convergent. The non-convergence of the conventional solution was proved by Zhang *et al.* (1993) in the case of unidirectional dual wave interaction. Here, we only numerically demonstrate this point. A set of steep dual free-wave components are studied with the long-wave component at the frequency of 0.07422 Hz and the short-wave component at 0.1992 Hz. The water depth remains 145.0 m. The short to long wave length ratio ε_l is 0.1390, $\varepsilon_1 = 0.2$ and $\varepsilon_2 = 0.1$. The direction angles are $+15$ and -15 degrees, respectively, for the long- and short-wave components. Figure 4.3a shows the comparison of the modulated short-wave elevations predicted using the two different approaches. For reference, the solution for unmodulated short-wave elevation is also presented. The modulated short-wave elevation is obtained by subtracting the long-wave elevation from the resultant wave elevation of the interacting dual wave components. The solutions of both approaches are truncated at second-order in wave steepness. Comparing with unmodulated short-wave elevation, the modulated elevation predicted by the phase modulation approach is greater in amplitude and shorter in wavelength at the crest of the long-wave component, and smaller and longer at its trough. These features are well known for modulated short-waves by long waves (Phillips 1979; Longuet-Higgins 1987). On the other hand, the predicted elevations using the conventional approach is much greater in

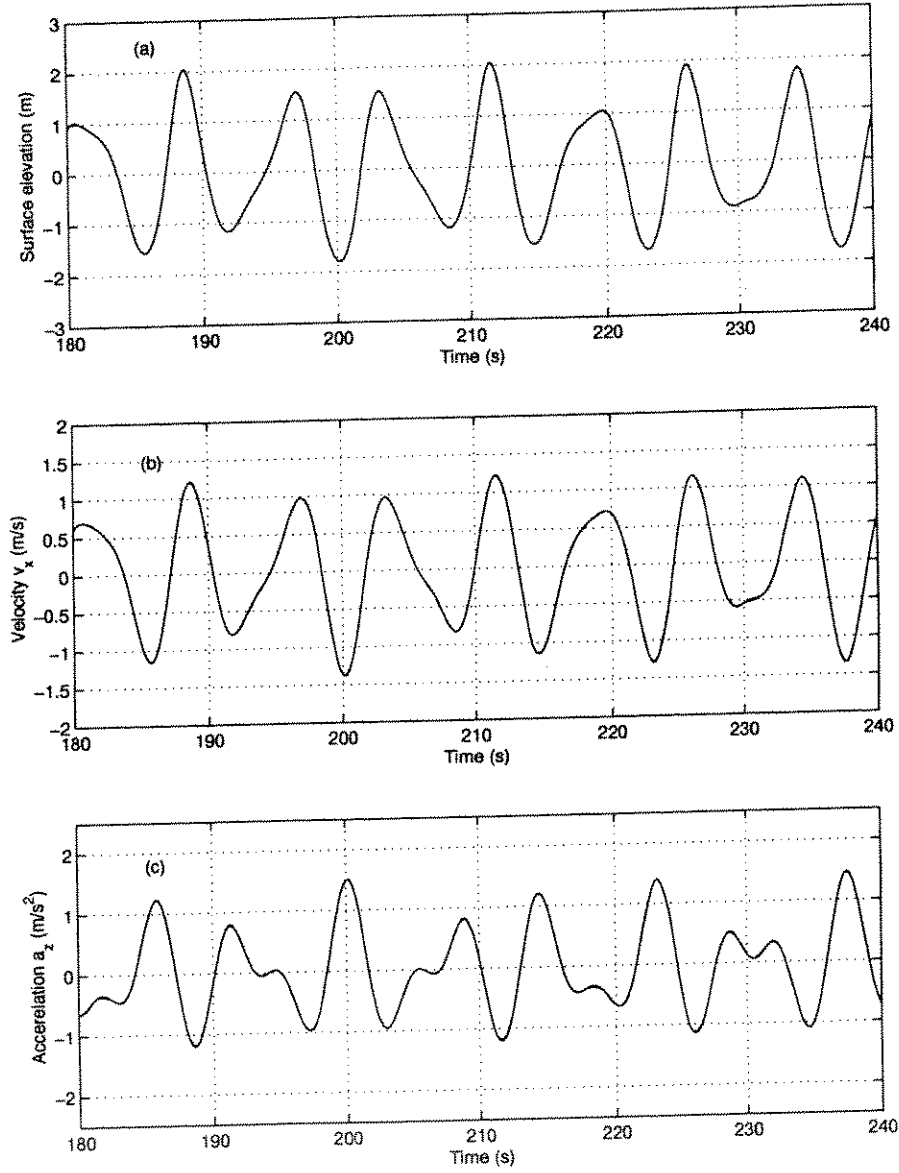


Figure 4.1: Comparison between the conventional perturbation solution (—) and the phase modulation solution (- - -) for a dual free-wave spectrum with $\varepsilon_1 = 0.10$, $\varepsilon_I = 0.3822$: (a) surface elevation; (b) horizontal velocity; (c) vertical acceleration.

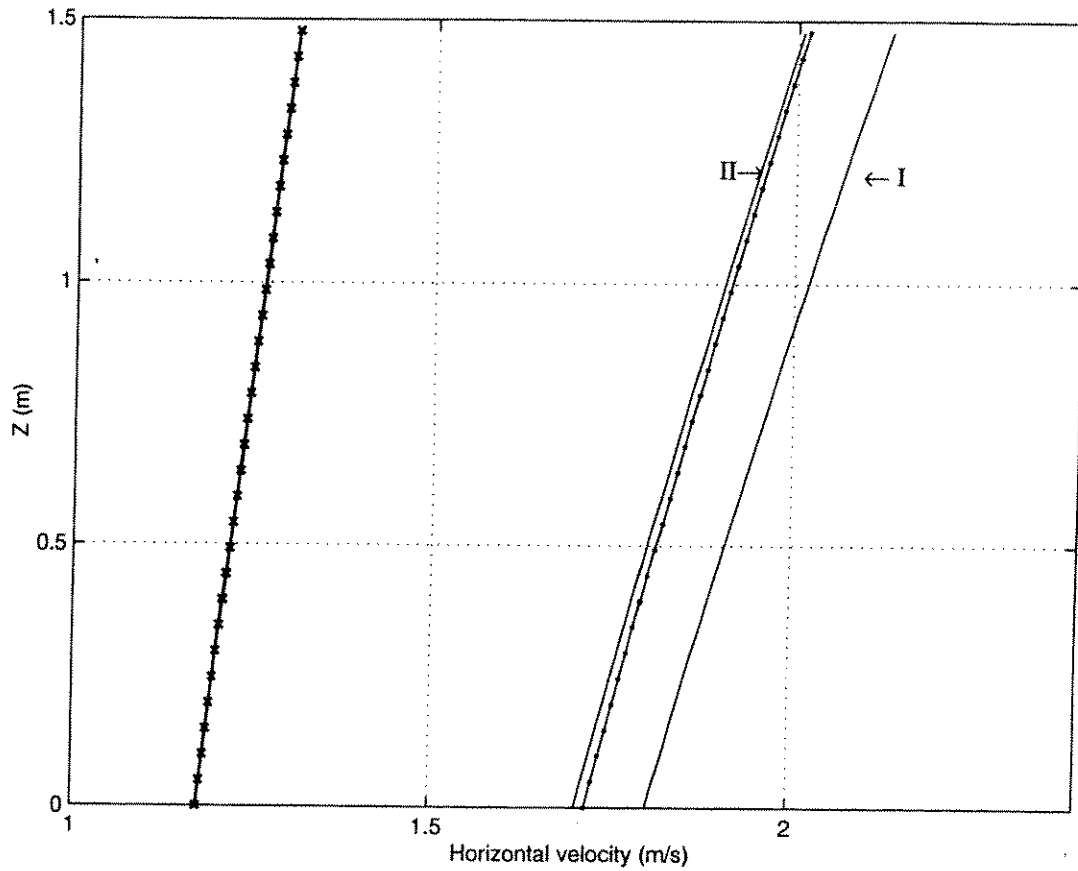


Figure 4.2: Comparison between the conventional perturbation solution (—) and the phase modulation solution (—•—) for a dual free-wave spectrum with $\varepsilon_1 = 0.10$, $\varepsilon_l = 0.3822$: x -direction horizontal velocity profiles of the long- and short-waves up to the leading-order (I —) and the second-order (II —), and long-wave velocity only (—×—).

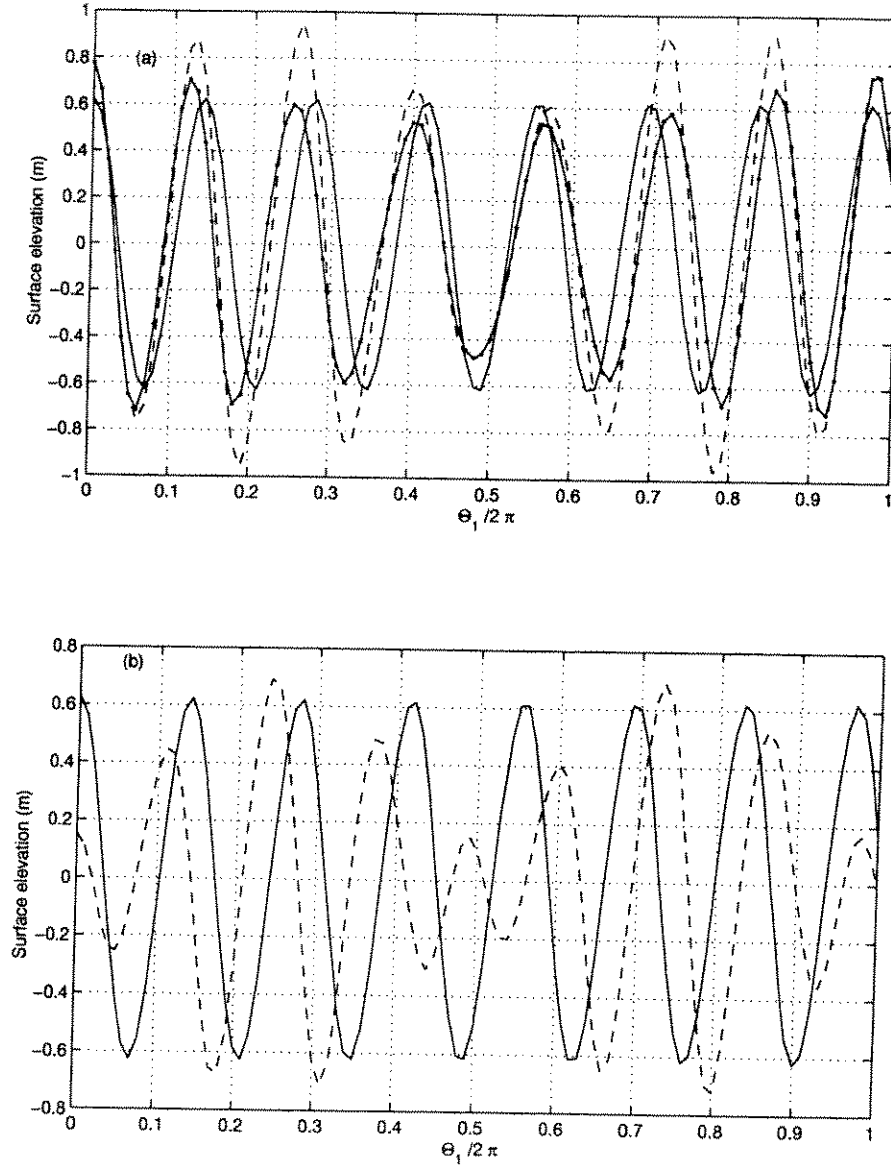


Figure 4.3: Comparison between the conventional perturbation solution and the phase modulation solution for a dual free-wave spectrum with $\varepsilon_1 = 0.20$, $\varepsilon_l = 0.139$: (a) short-wave elevation by the conventional perturbation solution at the leading-order (—), and up to the second-order (---) and by the phase modulation solution up to the second-order (—•—); (b) short-wave elevation by the conventional perturbation solution at the leading-order (—) and at the second-order (---), where Θ_1 is the phase of the long wave.

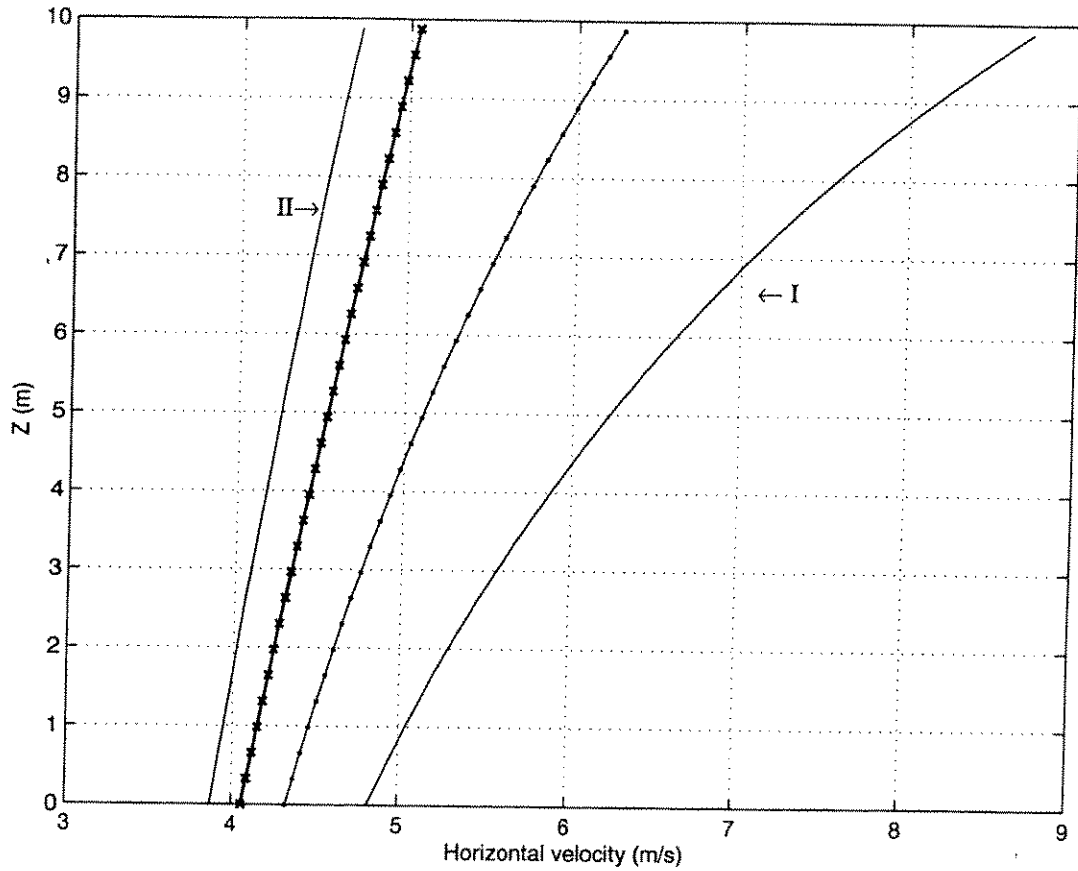


Figure 4.4: Comparison between the conventional perturbation solution (—) and the phase modulation solution (—•—) for a dual free-wave spectrum with $\varepsilon_1 = 0.20$, $\varepsilon_I = 0.139$: x -direction horizontal velocity profiles of the long- and short-waves up to the leading-order (I —) and the second-order (II —), and long-wave velocity only (—×—).

amplitude and shorter in wavelength at the intersections of the long-wave surface and the still water level, which are quite different from the features observed in the solution of the phase modulation approach. To show that the large differences between the solutions of the two approaches result from the non-convergence of the conventional solution truncated at second-order, the conventional solutions for the leading-order short-wave elevation and the elevation for the second-order bound wave components (sum- and difference-frequency bound waves) are plotted separately in Figure 4.3b. The comparison shows that the second-order bound-wave components are greater in amplitude than the leading-order short-wave component. This obviously violates the perturbation principle which requires the second-order solution to be much smaller than the first-order solution. The comparison implies that the conventional solution does not converge at second-order. However, one may ask why the bound-wave components are compared to the short-wave component not to the long-wave component. This is because when the short-wave component is much shorter in wavelength than the long-wave component, the frequencies and wavelengths of the second-order bound-wave components are close to those of the short-wave component. The significant differences between the two approaches can also be observed by comparing the resultant x -direction velocity under the wave crest. Figure 4.4 shows the x -direction horizontal velocity under the resultant wave crest where the short- and long-wave crests are coincident. The resultant horizontal velocity of the long wave and the leading-order short wave predicted by the leading-order conventional perturbation solution is much greater than the horizontal velocity induced by the long wave only. Although the contribution from the leading-order short wave is known to be exaggerated because of the factor $e^{k_2 z}$ (for $z \approx \zeta_1$), the increase in the resultant horizontal velocity is qualitatively correct because under the crest both wave components are in phase. However, when the resultant horizontal velocity is computed up to second-order, i.e. including the contribution from the second-order bound-wave components, the resultant horizontal velocity is found to be smaller than the horizontal velocity induced by the long wave only. The decrease in resultant horizontal velocity has

two implications. First, the contribution to the horizontal velocity from second-order bound-wave components is greater than that from first-order short-wave component. This again violates the perturbation principle. Secondly, the overall contribution to the horizontal velocity due to the presence of the short-wave component on the long-wave surface is opposite to the phase of the short-wave component. This is contradictory to both general wave theories and experiment observations. In contrast, the solution of the phase modulation method up to second order gives a physically reasonable description for the resultant velocity.

4.2 Comparison with Unidirectional HWM

A unidirectional wave field, or a long-crested wave field, is a special case of a directional wave field, in which all the wave components are propagating in the same direction and the wave properties along the crest line are identical. Since the unidirectional HWM has been verified against laboratory measurements (Spell *et al.* 1996), the DHWM is verified against it by predicting the wave properties of unidirectional irregular wave fields. For the first case, the nominal wave steepness of a unidirectional irregular wave train is 0.18, which is defined as the product of the half of the maximum wave height and the wavenumber at the peak frequency. The water depth is 145.0 m. The free-wave spectrum (Figure 4.5) and the specified initial phases used as input for the computation of resultant irregular waves were originally obtained by the decomposition of wave gauge measurements described in § 5.1. The two wave models are used to compute the resultant surface elevation at the location of 10.00 m downstream, and the pressure and velocity at the same horizontal location but 8.25 m below the mean water level. Figure 4.6 shows the calculated time-series of the surface elevation, dynamic pressure and horizontal velocity. The results of these two models are in excellent agreement.

Figure 4.7a shows another free-wave spectrum for verification of the DHWM. This spectrum represents a unidirectional transient wave train with extremely steep crests,

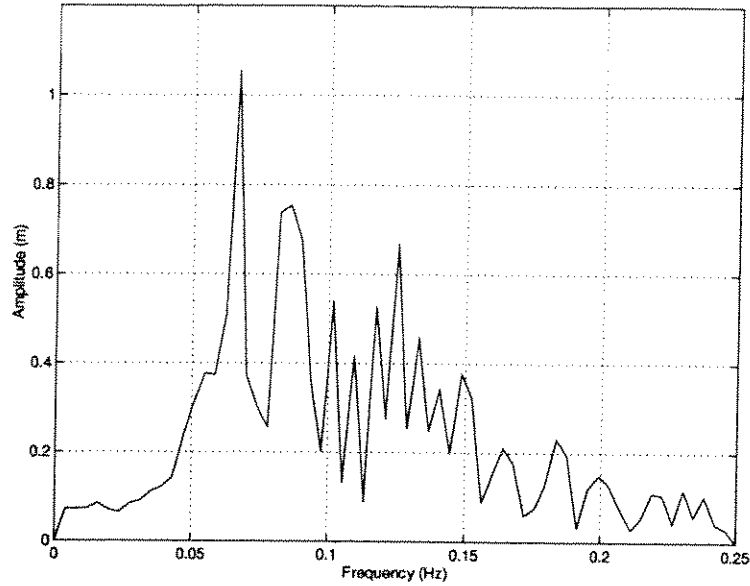


Figure 4.5: Unidirectional free-wave spectrum for verification of the DHWM against the unidirectional HWM.

which eventually leads to wave breaking (Zhang *et al.* 1997). The nominal steepness of the wave train is 0.2344. The water depth is 0.90 meter. Figure 4.7b & c show the computed surface elevation at the origin, and dynamic pressure at the same horizontal location but 25 cm below the mean water level. The results calculated using both methods are almost identical. These comparisons indicate that the DHWM and the unidirectional HWM are consistent in the case of unidirectional irregular waves.

4.3 Verification by Synthetic Data

The DHWM is examined in this section using the synthetic data which represent numerically simulated short-crested waves accurate up to second-order in wave steepness. This examination allows us to explore the accuracy and convergence of the present model since the synthetic data do not involve errors resulting from discrepancy between the ideal assumptions and real phenomena, such as viscosity effects, wave breaking, wave-wave interactions higher than the second-order in wave steepness, and wave-wind interac-

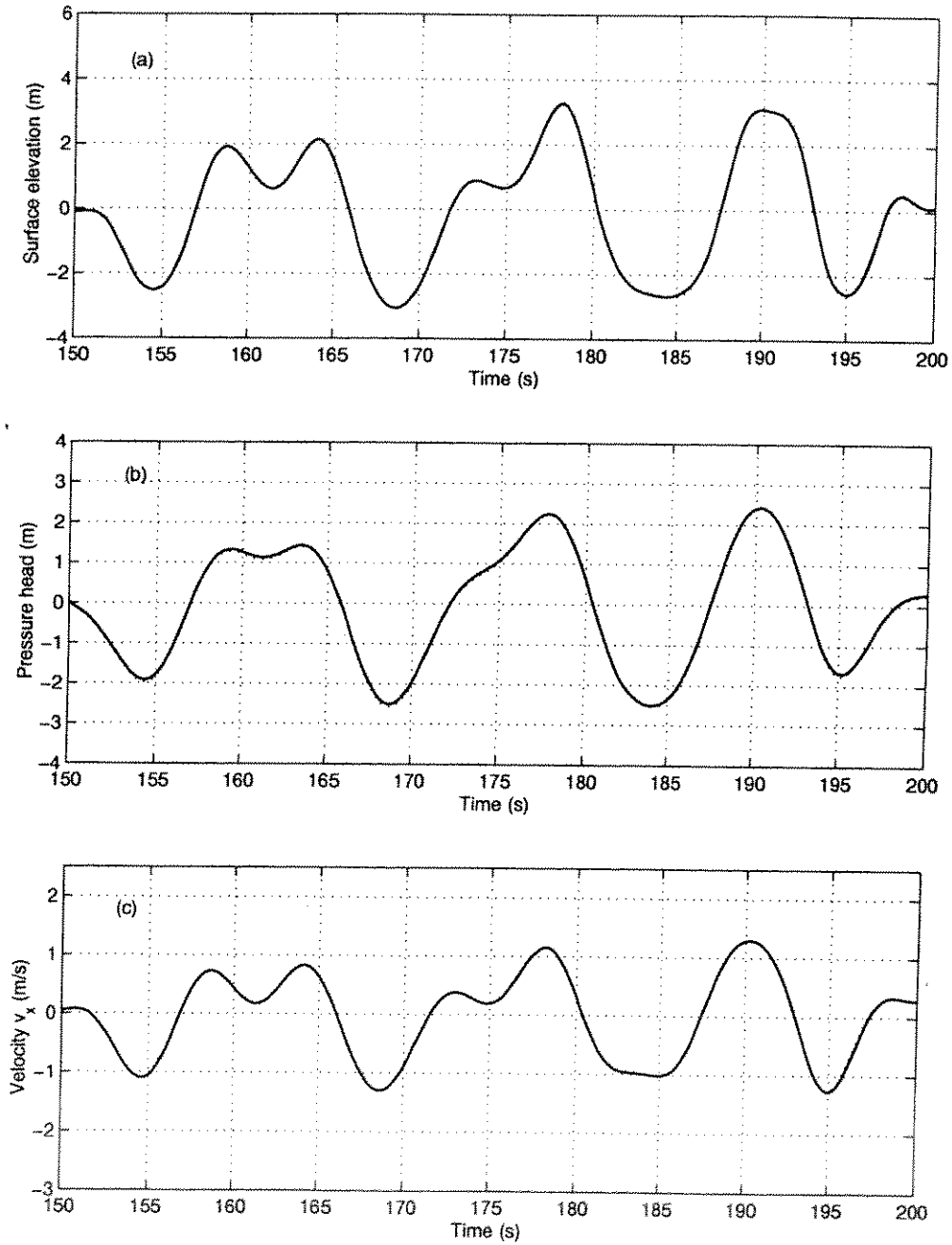


Figure 4.6: Comparison of the DHWM (—) with the unidirectional HWM (- - -): (a) surface elevation; (b) dynamic pressure; (c) horizontal velocity.

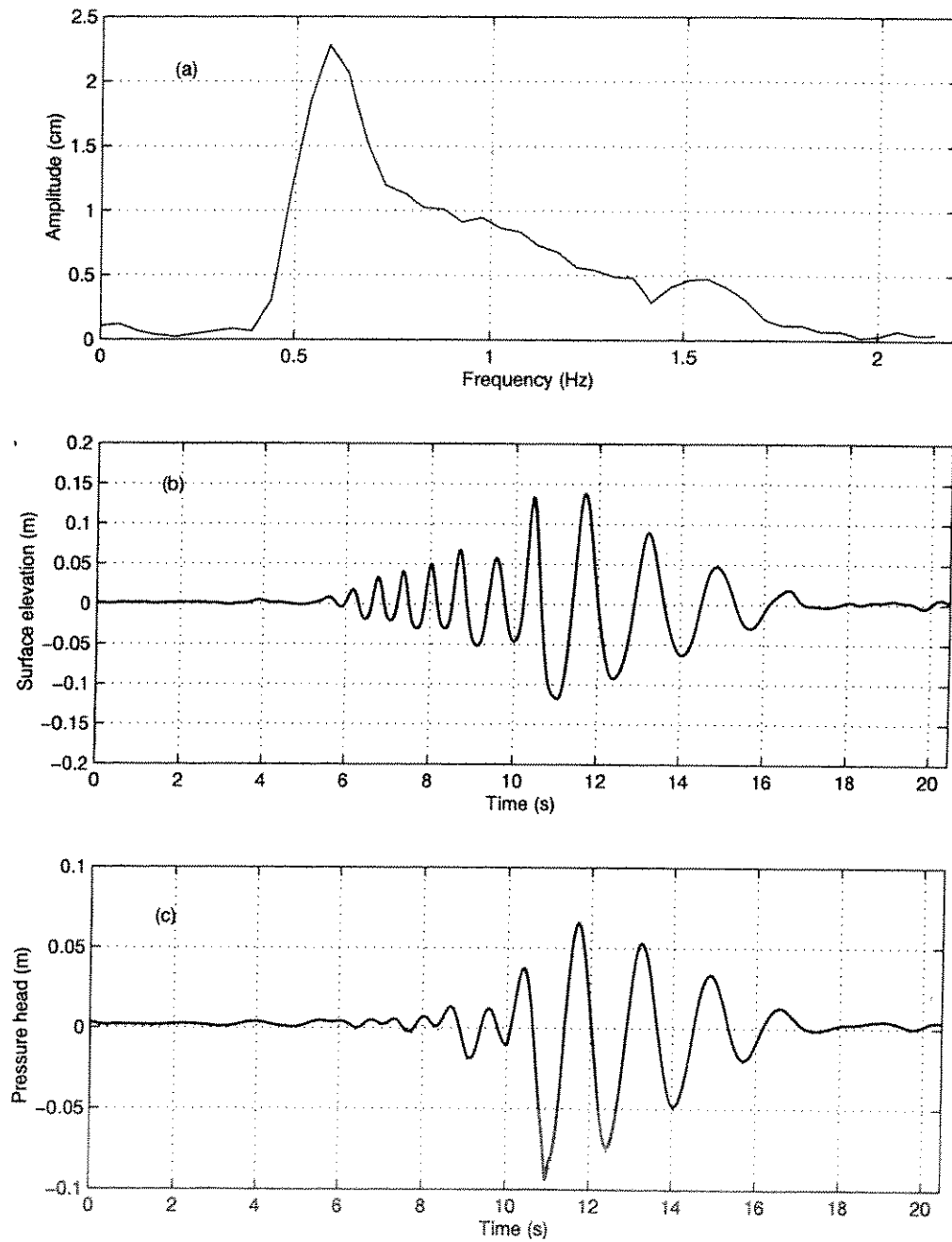


Figure 4.7: Comparison of the DHWM (—) with the unidirectional HWM (- - -) for a unidirectional breaking wave case: (a) free-wave spectrum; (b) surface elevation; (c) dynamic pressure.

tions. The characteristics of the free-wave components such as amplitudes, directions of propagation, and initial phases are given first and then the DHWM is used to generate the synthetic short-crested sea data, i.e. simulated time-series at fixed points. Then, the synthetic time-series are used as input to the numerical scheme of the DHWM described in § 3 and the synthetic wave field is decomposed into free-wave components. The decomposed results and the initial free-wave components used to generate the synthetic data are compared to check the accuracy and convergence of the DHWM.

A synthetic multidirectional wave field in water depth of 145 m is simulated based on four free-wave components. Each of the free-wave components is assigned to one of the characteristic frequency bands. The interactions among free-wave components are computed at least up to second-order based on the DHWM. The resultant time-series of wave elevation at the horizontal position (0,0) and two orthogonal horizontal velocity components at the same horizontal position but 10 m below the still water level are used as inputs for the wave decomposition. The comparison between the input and decomposed wave parameters is shown in Figure 4.8. The amplitudes, directions, and initial phases of the decomposed free-wave components are virtually coincident with those used as inputs for simulating the synthetic waves.

The next numerical wave simulation (shown in Figure 4.9) is based on a more realistic wave component selection which uses more free-wave components (64 discretized frequencies and single free-wave component at each frequency in water depth of 145 m). The input amplitudes, directions and phases are similar to the free wave components of the OTRC experiment data, which will be presented in § 5.1. As in the previous example, the given free-wave components are used to generate time-series of wave elevation at the horizontal position (0 m, 0.525 m) and two orthogonal horizontal velocity components at the same horizontal position but 8.53 m below the mean water level using the DHWM. The resultant times-series (synthetic data) are taken as the input for the wave decomposition. It can be seen that the decomposed free-wave components agree very well with the input. There are, however, some small discrepancies for the wave components of very

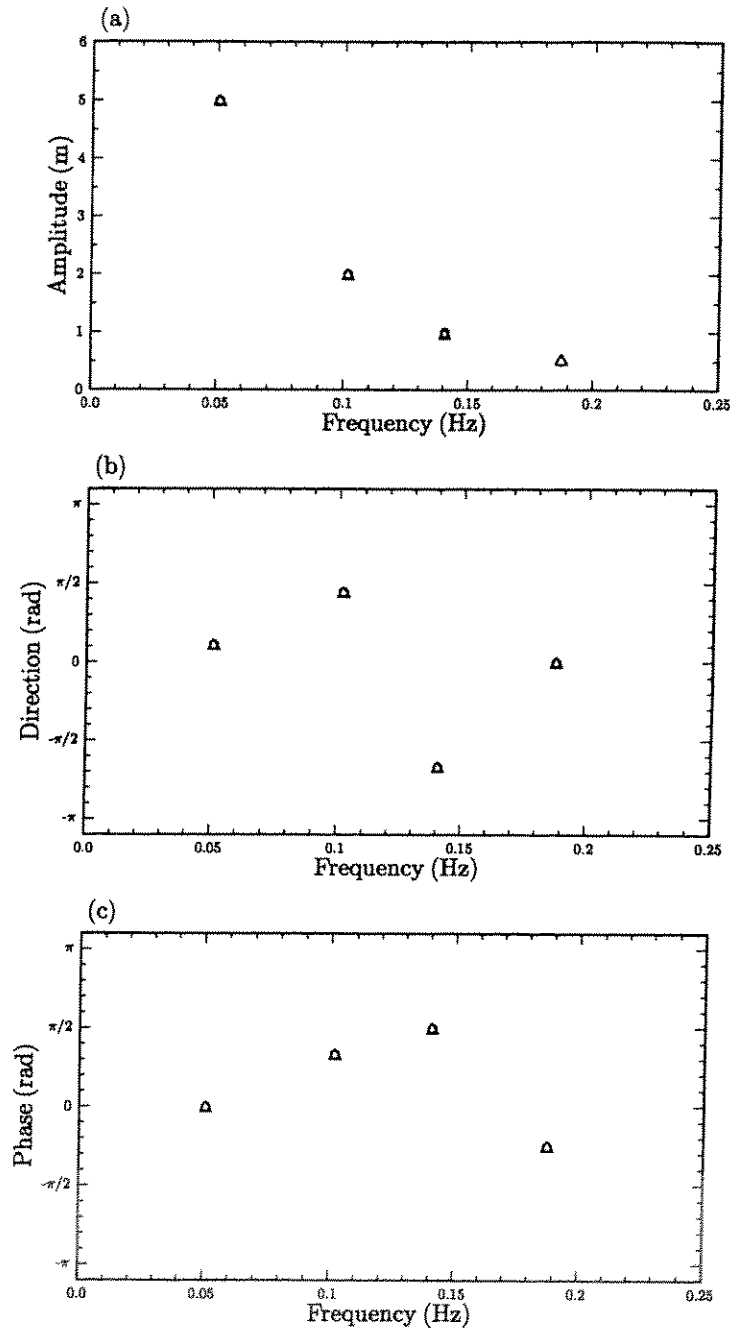


Figure 4.8: Free wave components (4) used as input (o) for the wave field simulation and their output (Δ) after the wave field decomposition.

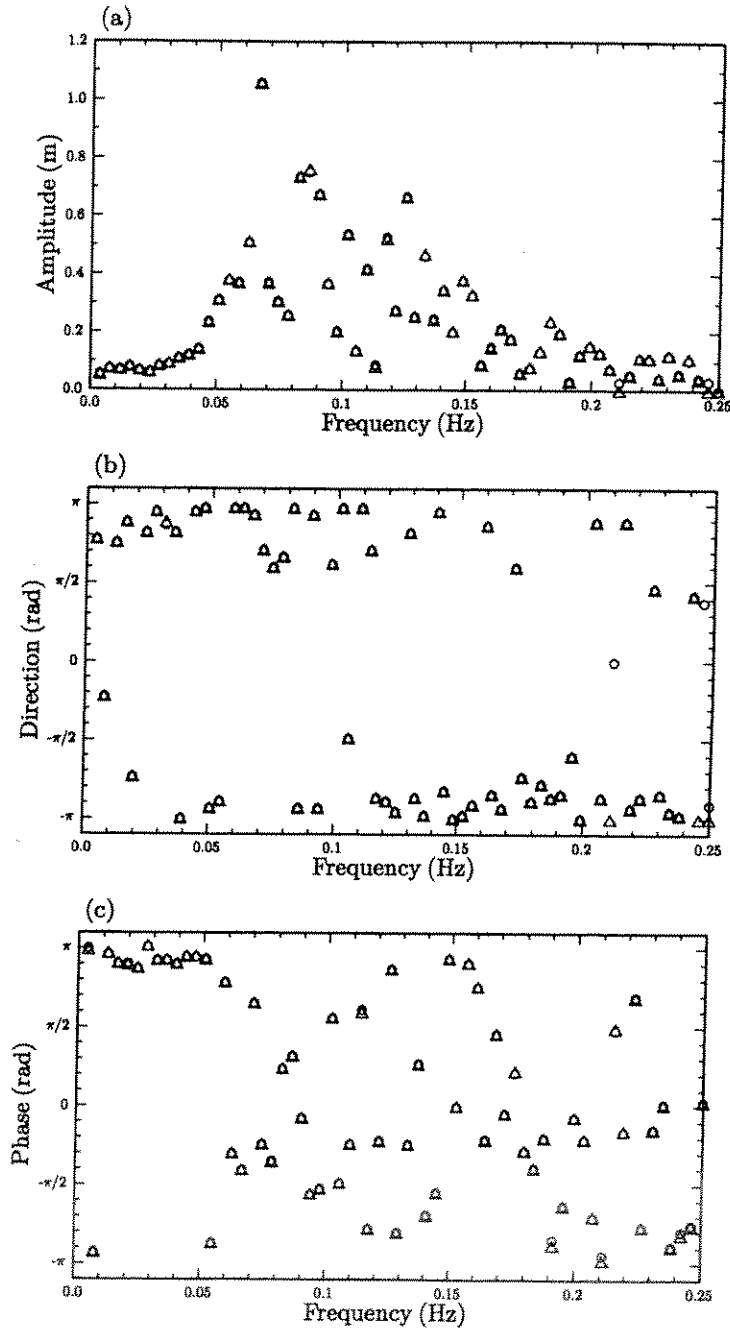


Figure 4.9: Free wave components (64) used as input (○) for the wave field simulation and their output (△) after the wave field decomposition.

low energy. Because the amplitudes of these components are so small that the differences between the prediction and input may be smaller than the prescribed error tolerance. In addition, as pointed out by Jeffery (1986), the correlation matrix used in the EMLM can be singular if the input data are from a single realization. The singularity can be avoided by disturbing the matrix with an additional small quantity of incoherent noise (Jefferys 1986), which might slightly affect the decomposed results. Excellent agreement is also observed when the surface elevations at three different locations are simulated as the measurements are from a wave gauge array (Prislin 1996).

5 Comparisons with Laboratory and Field Measurements

Unlike synthetic wave data, laboratory and field measurements are more or less contaminated by ambient noise, biased errors and imperfect calibration due to the limitations of instruments and data acquisition system. In addition, it should be noted that the DHWM is based on the potential theory and its nonlinear wave solutions are truncated at second-order in wave steepness. Therefore, effects such as viscosity and high-order nonlinear effects, which are naturally present during the measurements, are neglected in the DHWM. Wave-breaking and wind may also exist in the field measurements. Hence, the comparisons of the prediction based on the DHWM with the corresponding laboratory and field measurements may show how useful the DHWM is to real ocean waves.

The main objective of the comparison of the predictions with the corresponding laboratory and field measurements is to validate the effectiveness and accuracy of the DHWM for the deterministic decomposition of a short-crested irregular wave field. The computation includes two parts: (a) decomposing a wave field represented by the measured data at certain locations into an assemble of free-wave components; (b) predicting the wave properties at all measurement locations using the DHWM based on the decomposed free-wave components. In most cases, part of the measured data are used for the wave field decomposition and the remaining part of measurements are reserved for examining the predictions of the DHWM. The accuracy and feasibility of the DHWM are thus examined in two different tests. The first test involves the comparison of the predicted time-series with the corresponding measurements used as input in the deterministic wave decomposition. This kind of predicted time-series is referred as recovered signals. This test examines whether or not the iteration in our numerical scheme converges. The second test involves the comparison of the prediction with the corresponding measurements not used as input in the wave decomposition and hence is more compre-

hensive. This kind of predicted time-series is referred as predicted signals. This test may reveal whether or not the deterministic decomposition is useful in predicting wave characteristics nearby the measurements. The comparisons also demonstrate the flexibility of the DHWM by showing that the methodology is applicable to measurements from various types of sensors. The effects of the numbers of the sensors and the free-wave components at each frequency on the accuracy of the decomposition and prediction are also investigated.

5.1 OTRC Laboratory Data

5.1.1 Experimental Measurement

Laboratory data were collected in a multi-directional deep-water wave basin at the Off-shore Technology Research Center (OTRC), Texas A&M University. The OTRC wave basin is capable of generating waves, currents, and wind. The basin is 45.7 m long, 30.5 m wide, and 5.8 m deep. At the center of the basin there is a rectangular deep pit of 9.1 m long and 4.6 m wide, where the depth is adjustable from 5.8 to 16.7 m. The pit was covered during our tests so that the water depth was constant over the entire basin. At the North side of the basin, there is a multi-directional ‘snake-type’ wave generator, which consists of 48 hinged flaps (wave boards) in a row and are driven independently by servo-controlled linear hydraulic actuator. Each flap is 0.6 m wide and 9.84 m high. The wave maker is capable of generating multi-directional irregular waves through individually programmed drive signals for each wave board. The drive signals can be downloaded to three mechanical control units that control the wave boards. The wave maker is capable of generating oblique waves with a maximum angle of 60 degrees with respect to the longitudinal centerline of the basin.

To simulate an ocean wave field, the model scale is determined based on the Froude similarity criterion. For all tests in our study, the length scale of the model to prototype is 1:25. The data collected during the model tests were from the multi-array pressure

Sensor	Coordinates		
	x (m)	y (m)	z (m)
P1	0.000	0.000	-8.25
P2	0.000	-11.5	-8.25
P3	-11.6	0.000	-8.25
P5	11.28	0.000	-8.25
P6	5.625	-5.65	-15.9
P7	5.63	5.78	-15.9
W1	0.000	0.525	0.000
W2	0.000	-11.5	0.000
W3	-11.3	0.325	0.000
W4	0.000	11.5	0.000
W5	11.2	0.325	0.000

Table 5.1: Coordinates of the sensors in the OTRC model test (prototype scale).

and surface elevation measurements and from a single-point velocity measurements. The data used for the wave decomposition, however, are only pressure and surface elevation data because the measurements of wave particle velocities are found unreliable (Prislin 1996). The coordinates of the sensor locations in the OTRC model test are presented in Table 5.1 in which the capital letters P and W denote pressure sensors and wave gauges, respectively.

The directional waves are generated by combining two irregular wave trains of different peak frequencies and advancing in two different directions. The wave spectrum hence has two major peaks at different frequencies and different directions. The significant wave heights, directions and peak frequencies of the two irregular wave trains are $H_{1/3}^{(1)} = 7.5$ m, $\beta^{(1)} = -16^\circ$, $f^{(1)} = 0.07$ Hz, and $H_{1/3}^{(2)} = 5$ m, $\beta^{(2)} = +24^\circ$, $f^{(2)} = 0.1$ Hz, respectively, in the prototype scale. In addition, the wave components at each irregular wave train are spread for about 20 degrees with respect to the main wave directions, respectively. All results are presented in the prototype scale hereinafter. The significant wave height, estimated from the resultant frequency spectrum, is 7.3 m and the nominal

wave steepness, defined as the product of one half of the significant wave height and the wavenumber at the spectrum peak, is about 0.065. Hence, this wave field is of moderate steepness and does not represent the case of storm waves. Virtually no wave breaking is observed during the test. The duration of the analyzed records is 256 seconds and the sampling rate is 4 Hz. Further details of the experiments are referred to Prislin (1996).

5.1.2 Numerical Recovery and Prediction

The decomposition of the measured short-crested irregular wave field is initially carried out using two different sets of measurements as input: (a) the surface elevation at the wave gauges W1, W4, and W5, and (b) dynamic pressure at sensors P1, P5, and P7, respectively. A single wave component at each frequency is used for the wave decomposition because the signals for driving the wave maker were created by the same principle. The time-series of the surface elevation and pressure head are calculated based on the decomposed free-wave components and compared with the corresponding measurements which were filtered through a low-pass filter of cutoff frequency 0.25 Hz. First, the comparisons between the input and computed time-series of the surface elevation and pressure are presented in Figures 5.1 and 5.2, respectively. All the computed signals at the locations where the measurements were used as input, i.e. the recovered signals, are in excellent agreement with the measurements, indicating that the numerical scheme is convergent. Next, the proposed methodology is tested for the prediction of the wave properties at the locations where the measurements were not used in the decomposition. For this purpose, the dynamic pressure at P6 and the wave elevation at W3 are predicted, respectively, based on two sets of the decomposed free-wave components. The measured pressure at P6 is compared with the corresponding predictions in Figure 5.3. The predicted pressure time-series based on the decompositions of both the pressure and surface elevation measurements match the measured signals very well. The predicted surface elevations at W3 based on both of the two decompositions are presented

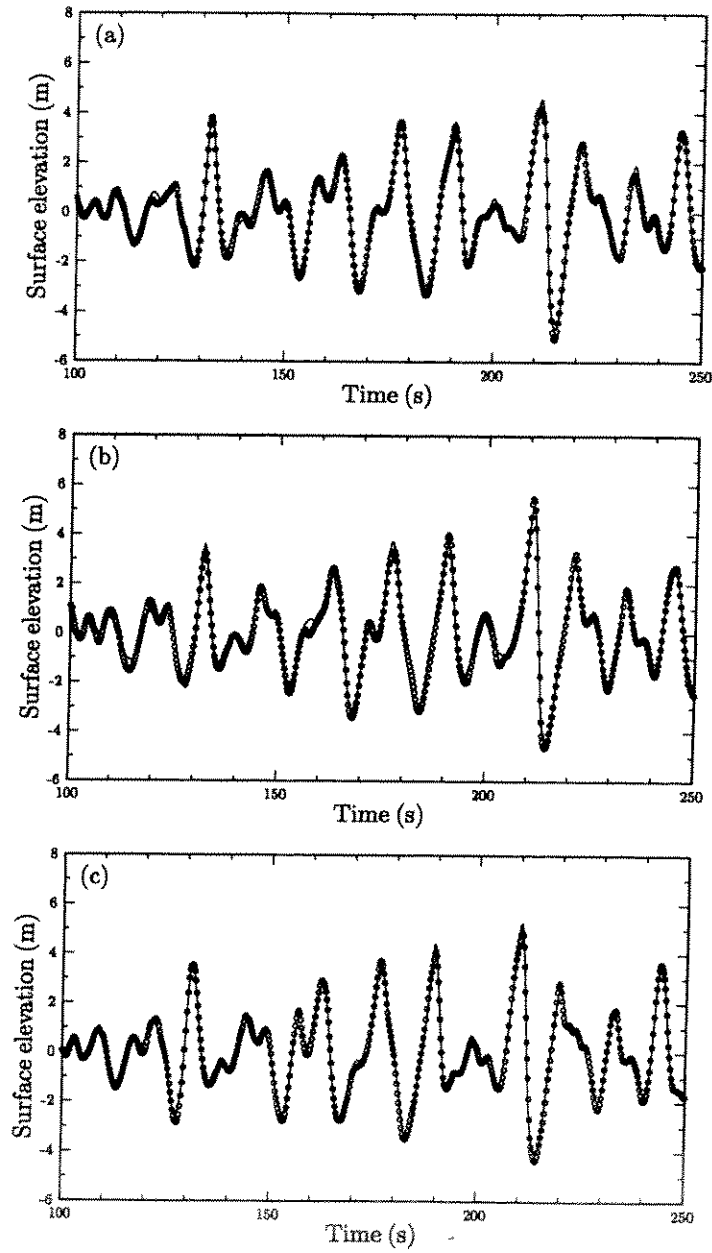


Figure 5.1: Surface elevation time-series as input (o) for the wave field decomposition and the corresponding recovered results (—) for the OTRC laboratory data at: (a) W1; (b) W4; (c) W5.

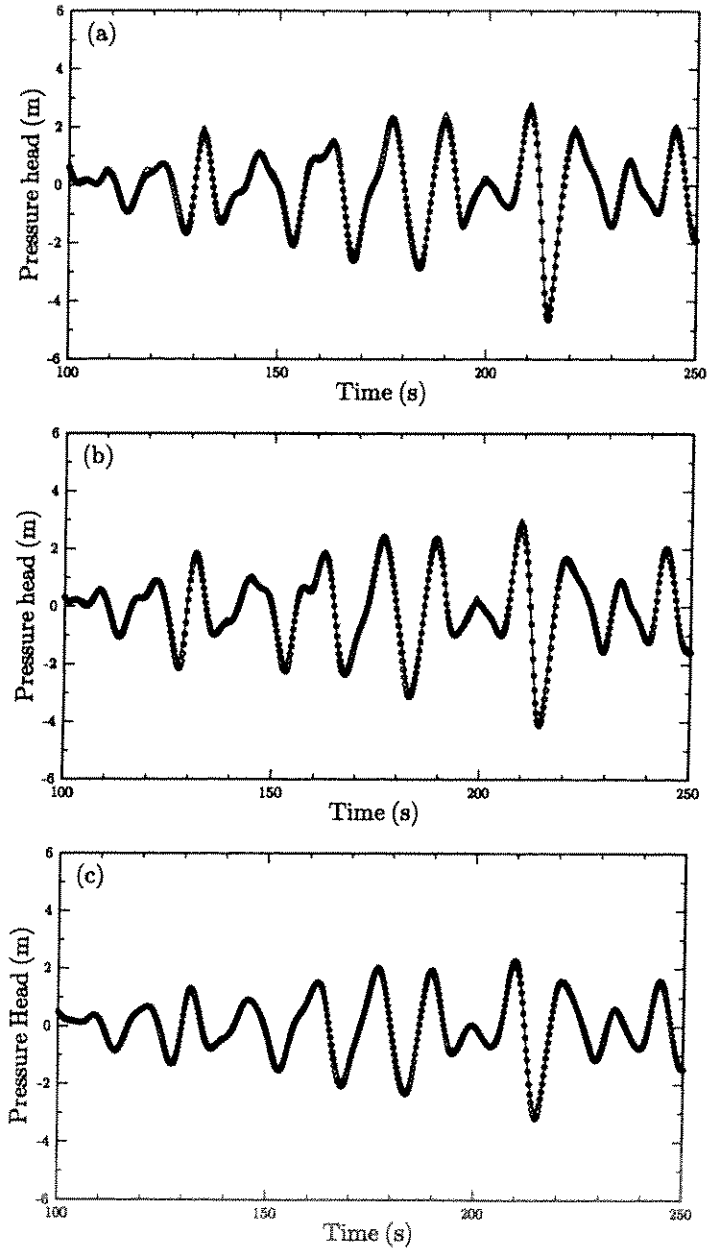


Figure 5.2: Pressure time-series as input (\circ) for the wave field decomposition and the corresponding recovered results ($—$) for the OTRC laboratory data at: (a) P1; (b) P5; (c) P7.

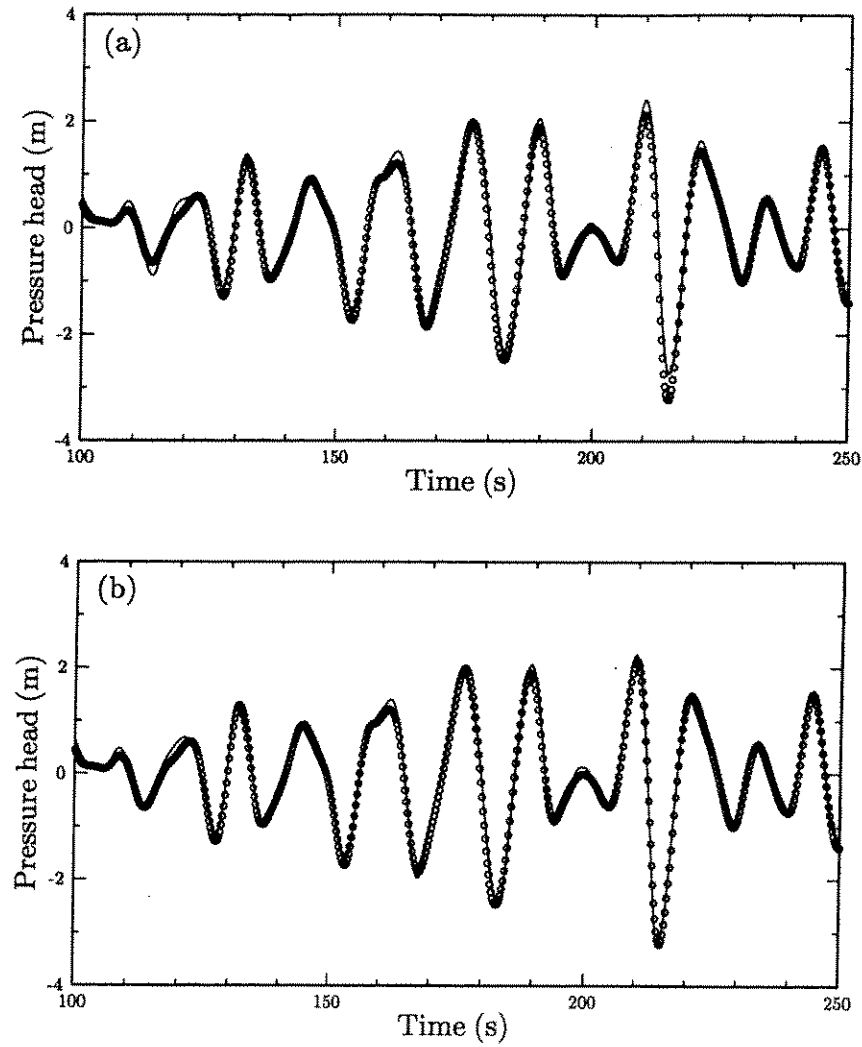


Figure 5.3: Pressure time-series as measurements (o) and the corresponding predicted results (—) for the OTRC laboratory data at the location of P6: (a) predicted from the surface elevation measurements; (b) predicted from the pressure measurements.

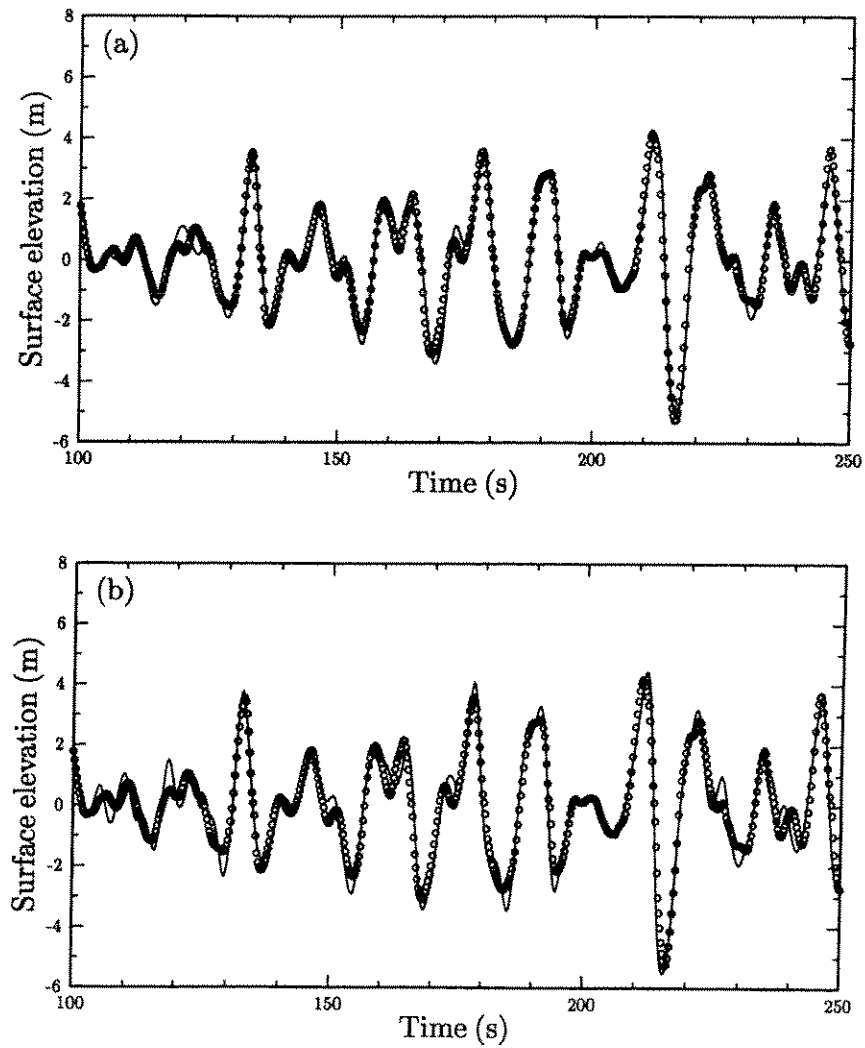


Figure 5.4: Surface elevation time-series as measurements (o) and the corresponding predicted results (—) for the OTRC laboratory data at the location of W3: (a) predicted the from surface elevation measurements; (b) predicted the from pressure measurements.

Model		W1		W2		W3		W4		W5	
Sensors	N_c	R	χ (%)	R	χ (%)	R	χ (%)	R	χ (%)	R	χ (%)
1 - 3	1	.993	1.16	.999	1.74	.993	1.28	.965	1.94	.974	2.19
1 - 3	3	.993	1.24	.992	1.48	.993	1.16	.965	2.01	.960	2.80
1 - 3	5	.996	0.85	.995	1.27	.997	0.94	.979	1.46	.981	1.74
1 - 3	7	.996	0.83	.995	1.19	.997	0.88	.981	1.66	.984	1.68
1 - 4	1	.994	1.01	.984	2.02	.991	1.37	.983	1.45	.977	2.04
1 - 4	3	.993	1.17	.988	1.67	.989	1.50	.990	1.11	.957	3.29
1 - 4	5	.996	0.89	.993	1.41	.996	0.91	.994	0.88	.976	2.06
1 - 4	7	.996	0.83	.994	1.32	.997	0.90	.995	0.84	.978	1.90
1 - 5	1	.990	1.25	.975	2.52	.985	1.78	.978	1.60	.983	1.65
1 - 5	3	.988	1.41	.979	2.36	.982	2.06	.983	1.63	.983	1.78
1 - 5	5	.990	1.26	.983	2.17	.991	1.41	.988	1.33	.988	1.39
1 - 5	7	.990	1.26	.984	2.15	.991	1.38	.988	1.26	.990	1.26

Table 5.2: Standard errors and correlation coefficients between the measured and computed time-series for the OTRC laboratory data.

in Figure 5.4. Similar to Figure 5.3, the agreement between the prediction based on the surface elevation measurement and the measured signals is excellent (Figure 5.3a). Because ocean waves are commonly measured using pressure transducers, it is of interest to examine the DHWM in predicting wave properties close to the free surface based on the data measured at the locations quite below the calm water level. In this case pressure measurements from the pressure transducer array P1, P5 & P7 were used for the decomposition and then the decomposed free-wave components are used to predict the surface elevation at the location of wave gauge W3. The measured and predicted signals are in satisfactory agreement (see Figure 5.4b). However, the discrepancies slightly increase in comparison with those in Figure 5.4a. This may result from greater noise to signal ratio in the higher frequency range of the pressure measurements.

To examine the effects of the number of wave components at each frequency and the number of sensors used in the decomposition on the accuracy of wave decomposition and predictions, different numbers of the surface elevation measurements and multiple

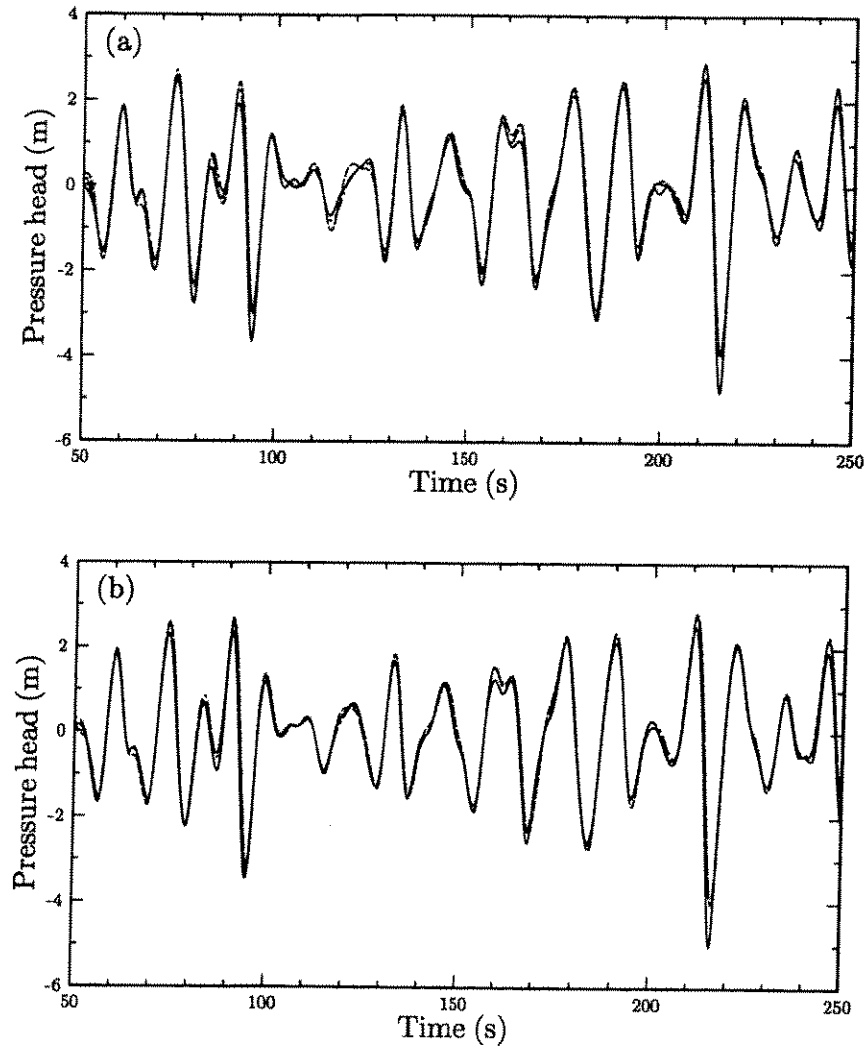


Figure 5.5: Pressure time-series as measurements (—) and the corresponding predicted results from the decomposed free-wave components based on the surface elevation time-series at W1–W5 with one (---) and seven (-.-) wave components at each frequency for the OTRC laboratory data: (a) at the location of P2; (b) at the location of P3.

free-wave components at each frequency are used in the decomposition. The time-series of surface elevations at all the measurement locations are calculated based on the decomposed free-wave components and are compared with the corresponding measurements. The correlation coefficients between the measured and calculated surface elevation time-series, and the standard errors are shown in Table 5.2. The correlation coefficient and standard error are defined as below,

$$R = \frac{\sum_{i=1}^N (\zeta_i - \bar{\zeta}) (\zeta_{Mi} - \bar{\zeta}_M)}{\left[\sum_{i=1}^N (\zeta_i - \bar{\zeta})^2 \right]^{1/2} \left[\sum_{i=1}^N (\zeta_{Mi} - \bar{\zeta}_M)^2 \right]^{1/2}}, \quad (5.1)$$

$$\chi = \frac{\sqrt{\frac{1}{N} \sum_{i=1}^N (\zeta_i - \zeta_{Mi})^2 \zeta_{Mi}^2}}{\zeta_{Mmax}} \times 100 \%, \quad (5.2)$$

where ζ_i and ζ_{Mi} are the calculated and measured surface elevations, respectively, and $\bar{\zeta}$ and $\bar{\zeta}_M$ are the means of ζ_i and ζ_{Mi} , respectively. N is the total number of data points in the time-series, and ζ_{Mmax} is the maximum surface elevation in the measured time-series. In Table 5.2, N_c is the number of free wave components at each frequency, and the column of 'Sensors' indicates which sensors' measurements are used in the decomposition. Overall, the table shows that the measured and calculated time-series match very well. For the recovered signals, all standard errors are smaller than 2.55% and all correlation coefficients are greater than 0.970. For the predicted time-series, these two parameters remain impressive, $\chi < 3.3\%$, $R > 0.955$. These results imply the high accuracy of the predictions in using the DHWM.

Table 5.2 also demonstrates that the increase in the number of wave components per frequency generally reduces the standard errors for the recovered signals but only slightly improves the accuracy of the predicted signals. The standard error for the recovered time-series can be reduced by up 40% by increasing the number of wave components

from one to seven at each frequency. This phenomenon is expected because more wave components provide more degrees of freedom for minimizing the target function of the phase fitting. However, the reduction of the standard error is not significant for the predicted signals, which may result from the narrow wave energy spreading in the test. Therefore, when the directional spreading of wave energy is narrow, the wave field can be modeled accurately by a single wave component at each frequency. It is noted that with the increase in the number of the sensors but with fixed free-wave components at each frequency used in the wave decomposition, both correlation coefficients and standard errors change slightly. No definite trends can be seen. Figure 5.5 shows the predicted pressure time-series at P2 and P3, respectively. The decomposition is made based on the elevation measurements at W1–W5. It is observed that all predicted signals match their corresponding measurements very well. By increasing the number of free-wave components at each frequency to seven, the predicted pressure time-series are slightly better in agreement with the corresponding measurements than the predictions of one wave component at each frequency.

5.2 HARVEST Field Data

5.2.1 Field Measurement

Pressure data were collected from an array of pressure sensors mounted on the Texaco Harvest offshore oil production platform, approximately 16 meters below the sea surface. The platform is a fixed structure located about 10 kilometers west of Pt. Conception in a water depth of 225 m. The data were transferred to the Coastal Data Information Program (CDIP) at the Scripps Institution of Oceanography at 3 hour intervals (Seymour *et al.* 1993).

A set of pressure data representing the sea state on May 24, 1993 were selected for this study. The sea state was a combination of two wave trains — a swell from the south and local wind waves from the north-west. The angle between their directions was

Coordinates	Sensor					
	P1	P2	P3	P4	P5	P6
x (m)	0.0	-22.9	-22.9	0.0	-59.4	-59.4
y (m)	0.0	0.0	22.7	22.7	0.0	22.7
z (m)	-16.0	-16.0	-16.0	-16.0	-16.0	-16.0

Table 5.3: Coordinates of the sensors for the HARVEST field measurements.

around 100 degrees. The spectral peaks of the swell and wind waves were around 0.066 and 0.10 Hz, respectively. The significant wave height, estimated from the resultant frequency spectra is 1.29 m and the nominal wave steepness is 0.012. Although the waves were not very steep, the case is chosen because the wave field is a combination of two distinct directional wave trains. The data were sampled at the rate of 1 Hz. The duration of the time-series used in the decomposition is limited to approximately 17 minutes assuming that within that duration of time wave properties such as wave amplitudes and directions of propagation are approximately stationary. There were six pressure sensors on the platform and their coordinates are listed in Table 5.3.

5.2.2 Numerical Recovery and Prediction

Initially, the measurements from the sensors P1, P2, and P3 are used for the wave decomposition, and the time-series from the sensors P4, P5, and P6 are reserved for comparison. Before the decomposition, the measurements of P1, P2, and P3 were filtered using a numerical low pass filter of the cutoff frequency of 0.185 Hz. The choice of the cut-off frequency at 0.185 Hz is because of low signal to noise ratio over the frequency 0.185 Hz. Based on the decomposed free-wave components, the pressure at the locations of the pressure sensors P4, P5 and P6 were predicted. The recovered pressure time-series at P1, P2 and P3 and the predicted pressure time-series at P4, P5 and P6 are compared with the corresponding measurements in Figures 5.6 and 5.7, respectively. The computed signals and the measurements are in excellent agreement.

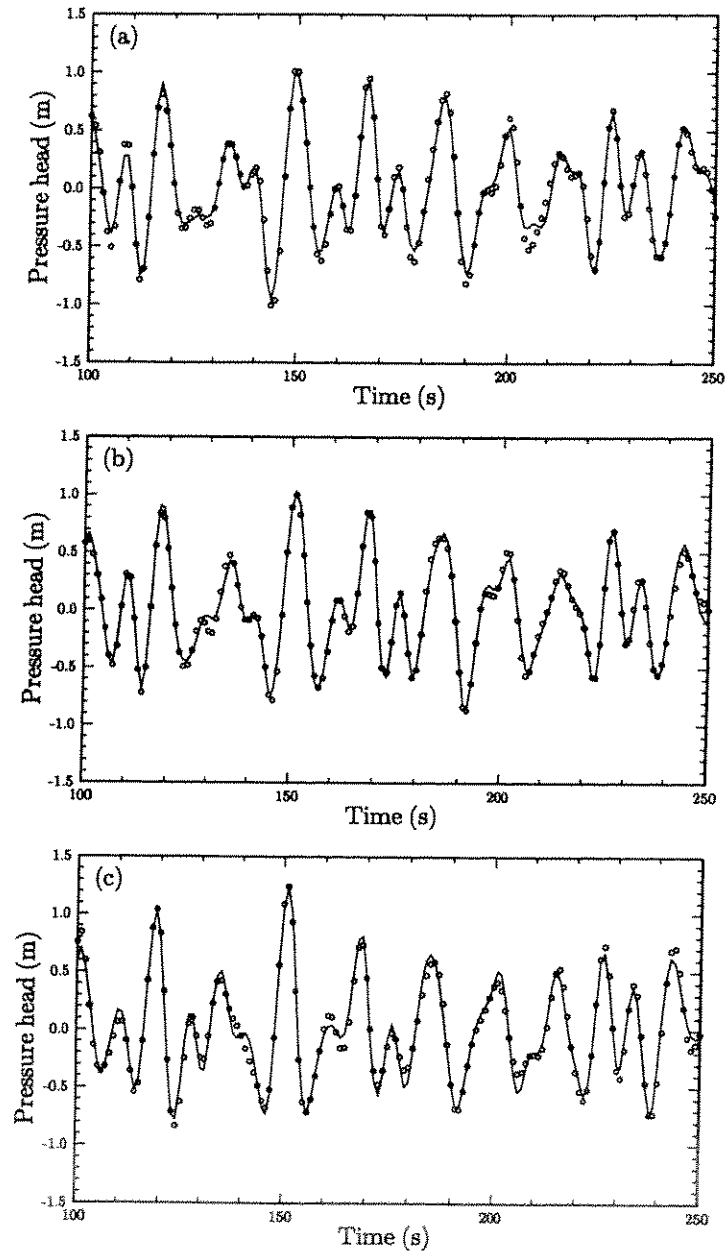


Figure 5.6: Pressure time-series as input (o) for the wave field decomposition and the corresponding recovered results (—) for the HARVEST field measurements at: (a) P1; (b) P2; (c) P3.

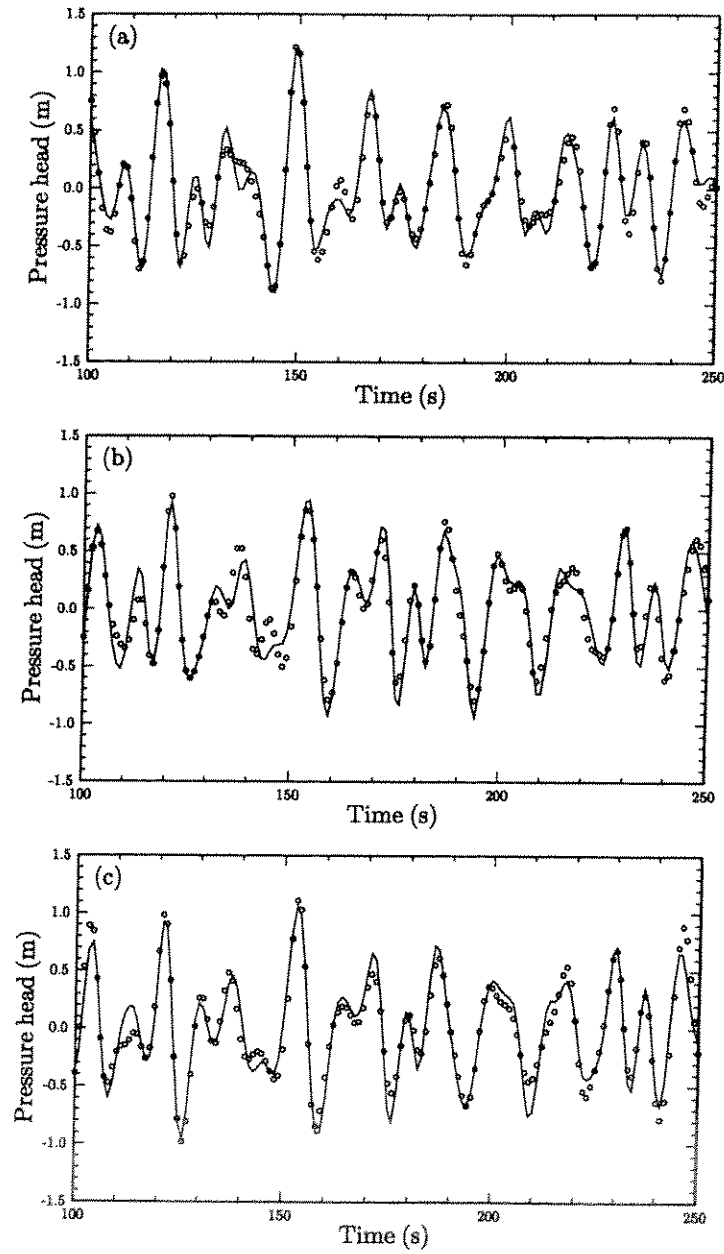


Figure 5.7: Pressure time-series as measurements (o) and the corresponding predicted results (—) for the HARVEST field measurements at: (a) P4; (b) P5; (c) P6.

Model		P1		P2		P3		P4		P5		P6	
Sensors	N_c	R	χ (%)	R	χ (%)	R	χ (%)	R	χ (%)	R	χ (%)	R	χ (%)
1 - 3	1	.991	0.96	.994	0.90	.988	1.29	.983	1.43	.968	2.12	.960	2.47
1 - 3	3	.995	0.77	.992	1.14	.994	0.88	.964	2.00	.919	3.44	.925	3.39
1 - 3	5	.998	0.52	.997	0.70	.997	0.73	.974	1.71	.958	2.37	.938	3.03
1 - 3	7	.998	0.43	.998	0.59	.998	0.68	.978	1.44	.959	2.31	.953	2.82
1 - 4	1	.955	2.43	.958	2.52	.962	2.41	.962	2.09	.941	2.97	.939	3.01
1 - 4	3	.954	2.27	.952	2.82	.958	2.68	.957	2.22	.878	4.86	.888	4.83
1 - 4	5	.958	2.26	.960	2.55	.965	2.33	.964	2.02	.917	3.28	.925	3.02
1 - 4	7	.960	2.29	.961	2.45	.966	2.28	.965	1.98	.937	2.92	.933	3.00

Table 5.4: Standard errors and correlation coefficients between the measured and computed time-series for the HAR-VEST field measurements.

The above results for the recovered and predicted time-series in Figures 5.6 and 5.7 are obtained based on the wave decomposition using the measurements of three transducers and one directional free-wave component at each frequency. The effects of the number of sensors and the number of wave components at each frequency used in the wave decomposition on accuracy of the decomposition and prediction are also investigated here. The correlation coefficients and standard errors for the computed and measured signals are shown in Table 5.4. The trends shown in Table 5.4 are similar to those observed in § 5.1. It seems that there is not significant improvement in correlations and standard errors due to the increase in the number of sensors. Increase in the number of wave components at each frequency improves the accuracy of the recovered times-series, but does not improve the accuracy of predicted time-series significantly.

5.3 FULWACK Field Data

5.3.1 Field Measurement

The FULWACK (Fulmar Wave Crest Kinematics) measurement was conducted at Fulmar Platform in the central North Sea during the winter of 1981–82. The data was collected during the second storm on November 24, 1982. There were two storms in series with a delay of 36 hours. Both storms had the same path and relatively slow forward motion that caused very high waves in the North Sea on November 24, 1982 (Forristall 1986). The water depth at the measurement site was 82.5 m.

A Baylor wave gauge and five Marsh-McBirney model 524 spherical electro-magnetic velocity meters (EMV) were installed outward the north side of the platform. The standard Baylor wave gauge consists of two vertical parallel steel wire ropes each of 12.7 mm diameter, separated at a distance of 228.6 mm and stretched under tension through the sea surface. The wires form an electrical transmission line terminated at its lower end by the sea surface. The impedance of this line was measured at 650 kHz, which assured linear instrument characteristics. The support system for the EMVs was

Coordinates	Sensor			
	Wave gage	EMV 5	EMV 2	EMV 4
x (m)	0.00	-0.66	-3.07	-1.21
y (m)	0.00	0.00	0.00	0.00
z(m)	N/A	-8.53	4.88	-5.48

Table 5.5: Coordinates of the sensors in the FULWACK field measurements.

a single wire rope, stretched over the upper and lower sheaves to form a pair of taut wires. The tension in the taut wire was adjusted to a desired value with a spring-loaded tensioning device. The EMVs and their cables were clamped to one side of the loop and lowered to a position by rotating the top sheave. The locations of three EMVs used in this study are deduced from Forristall (1986) and they are given in Table 5.5. During the measurement, the EMV 3 did not work, and the EMV 1 was seldom submerged in the water, so these two measurements were not included in our study. The coordinate system for velocity measurements was an orthogonal right-hand-side coordinate system with the z -axis oriented upward. The x -axis was pointed to 71.5° true north. The origin of the coordinate system was placed at the calm water level.

Before recording, all signals were passed through the same type of low-pass filters (the cutoff frequency was 4 Hz), which guaranteed the same phase lags for all signals. The calculation performed by Forristall (1986) showed that the natural frequency of the taut wire system was around 2 Hz. The vibration of EMVs is clearly seen from the measured velocity data.

A time-series of 256 seconds involving steep waves is selected and analyzed with a cutoff frequency of 0.25 Hz, which is about 3.3 times of the frequency at the spectral peak. The significant wave height is 11.2 m, and the nominal wave steepness is 0.138. The directional energy spreading is narrow and unimodal. The cutoff frequency is selected to be 0.25 Hz because the signal to noise ratio of the measurements from EMV 5 is too low above that frequency. The time-series from EMV 5 is chosen as input for

the wave decomposition because it is the only continuous time-series among all EMV measurements. All the other velocity measurements are intermittent since the EMVs emerged out of water when deep troughs passed by. Hence, they were not used for decomposition. However, they were used for the comparison with the predicted signals.

The FULWACK data are unique in the following three respects: (a) waves were relatively steep (nominal wave steepness is 0.138), (b) measurements were taken at the same horizontal position (not an array of the same type of instruments), and (c) measurements were taken at different depths below and above the calm water level.

5.3.2 Numerical Recovery and Prediction

The DHWM is used to decompose the wave field based on the measurements of surface elevation and a pair of horizontal velocity components (EMV measurements) at 8.53 meters below the calm water level. As discussed in earlier sections, because of very narrow directional energy spreading, only one wave component is used at each frequency for the wave decomposition. Horizontal velocity components at 5.48 meters below the calm water level (EMV 4) are predicted and compared with the corresponding measurements.

The measurements used as input for the wave decomposition are filtered by neglecting wave components above the cutoff frequency of 0.25 Hz. The comparisons of input and recovered time-series for the surface elevation and the horizontal velocity components at 8.53 meters below the calm water level are given in Figure 5.8. The recovered signals are in reasonably good agreement with the corresponding measurements, noticing that there were noises in the measured velocities induced by the vibrations of the taut wires.

The prediction of velocity components at depth $z = -5.49$ m (EMV 4) are compared with the corresponding measurements in Figure 5.9. In this case, the measured signals could not be filtered because of the intermittent nature of the time-series. The predicted signals agree very well with the measurements. In Figure 5.9, the flat zero sections in the predicted signals represent the time intervals when the sensors are out of water.

Some departures from the measured values are due to the large vibration displacement of velocity meter EMV4 rather than by the inaccuracy of the model. Forristall (1986) reported that the velocity meter at this depth had the biggest displacement of about 0.91 meters in a wave of 23 meters high. The predictions were also made to compare with measurements by EMV2, as presented in details by Prislin & Zhang (1997). They are not repeated here.

One of the prominent advantages of the DHWM is its ability to accurately decompose a wave field and to predict wave kinematics under the wave crest and above the calm water level. Other existing methods commonly used in practice for wave kinematics predictions in the wave crest are usually based on *ad hoc* modifications such as the 'stretching' and extrapolation techniques (Gudmestad 1991). These methods do not satisfy the hydrodynamic principles such as the free-surface boundary conditions and the Laplace equation, and do not account for wave directionality. Thus, their predictions of wave kinematics are quite inaccurate.

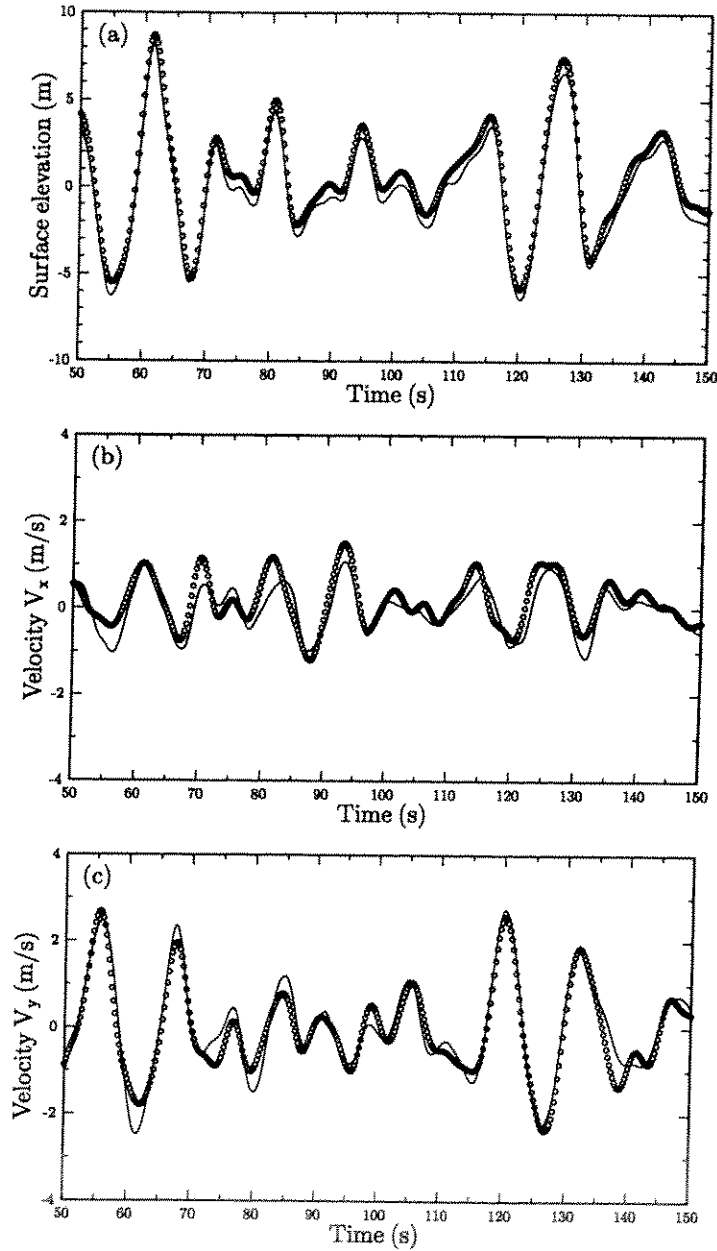


Figure 5.8: Time-series as input (o) for the wave field decomposition and the corresponding recovered results (—) for the FULWACK field measurements: (a) surface elevation at the location of the wave gauge, (b) V_x at EMV 5; (b) V_y at EMV 5.

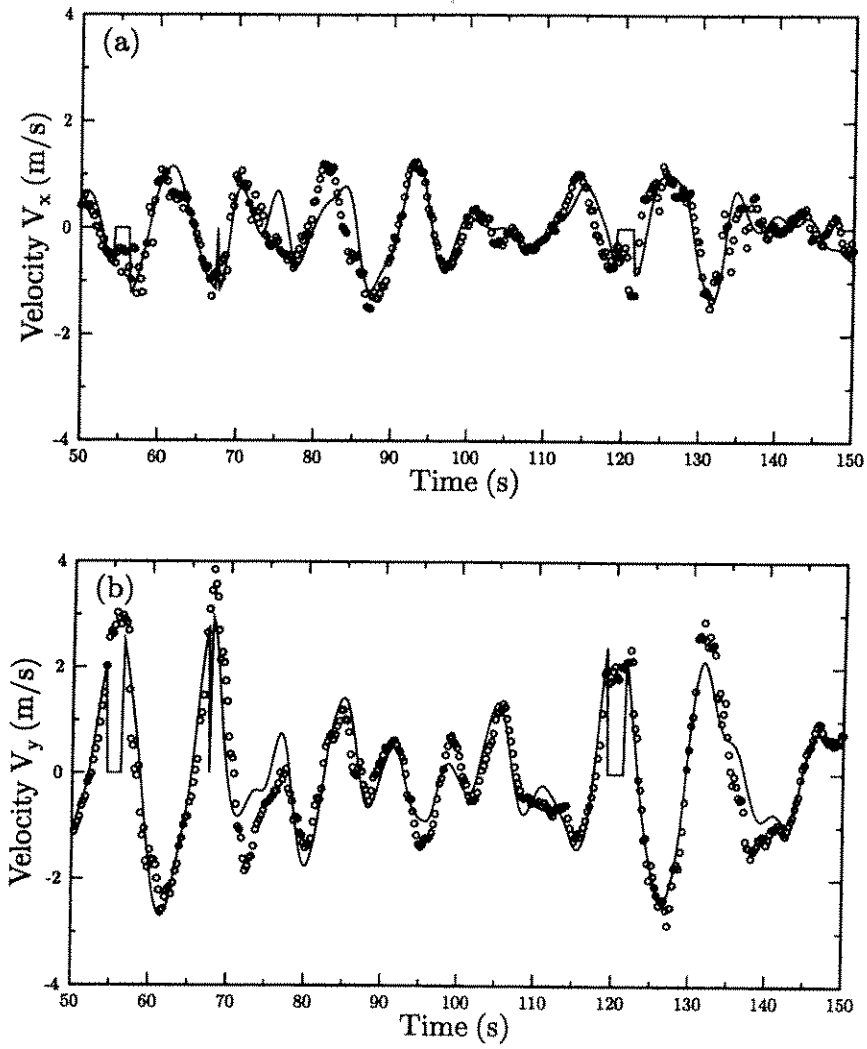


Figure 5.9: Velocity time-series as measurements (\circ) and the corresponding predicted results (—) for the FULWACK field measurements: at EMV 4: (a) V_x ; (b) V_y .

6 Conclusions and Further Work

A new methodology for the deterministic decomposition and prediction of short-crested ocean waves is described. This method has been validated through the comparisons with synthetic data, laboratory and field measurements and proved to be reliable, flexible and robust. It is able to provide accurate predictions for engineering applications based on wave measurements.

The methodology integrates three fundamental features of ocean waves: wave directionality, initial wave phases, and nonlinear wave-wave interactions. Based on the literature survey, this is the first time that all these features have been considered jointly to study an ocean wave field and its wave characteristics in a deterministic manner. The novelty of present method is that no priori assumption was made regarding functional or statistical properties of free-wave components. The purpose of wave decomposition is to determine the free-wave (linear) components constituting measured irregular wave field. Only after they are known, wave properties other than those measured can be deterministically predicted in the vicinity of the measurements. The difficulties of wave decomposition stem from the complicated structure of wave fields and inherently intertwined directional nonlinear waves. The additional challenge is that a wave field is described by a limited number of measurements.

The directional hybrid wave model (DHWM) calculates directional, nonlinear, and initial phase characteristics of free-wave components based on as few as three measurements of short-crested irregular ocean waves. It unifies conventional and contemporary nonlinear wave theories based on the wave phase modulation, attributed to the nonlinear hybrid wave theory (Zhang *et al.* 1993; 1996a). The DHWM is materialized in three major steps: the extended maximum likelihood method (EMLM) (Isobe *et al.* 1984) is employed for the computation of directional energy spreading, a least square phase fitting method is used for determining initial phases of free-wave components, and nonlinear effects up to at least the second-order in wave steepness are computed based on

the hybrid wave model and subtracted from the corresponding measurements. These three steps are related but each of them can be individually revised or replaced with its improvement in the future.

The consistency of the DHWM was examined numerically. Its accuracy and convergence were verified against the unidirectional hybrid wave model and two sets of synthetic data. The DHWM was also applied to one set of laboratory measurements and two sets of field measurements. In all cases, whether the input time-series were obtained from wave gauges, pressure sensors or current meters, the predictions of wave properties were accurate and in excellent or satisfactory agreement with the measurements.

The methodology allows for the use of different kinds of measurements as input, which is especially useful in various field and laboratory measurements. The DHWM can predict wave properties other than the measured and the prediction can be used to study wave-structure interactions and for the checking of wave measurements other than that used during the decomposition process.

The DHWM is, however, in its infant stage. There is a plenty of room for improvement. In the present work, the water depth is assumed to be uniform, and of intermediate depth with long-wave components and deep with respect to short-wave components. The extension of water depth to allow for intermediate to short-wave components and shallow to long-wave components will certainly offer new applications to coastal processes. The EMLM for wave directional decomposition based on the cross-spectral approach may fail in the bi-modal directional waves due to the artificial phase locking for the wave components of the same frequency but from different directions of propagation, when it is applied in a deterministic manner, i.e. no averaging over many realizations. Because of this weakness, it is important to work on better data-adaptive methods for directional decomposition. Finally, to better validate the DHWM, more comparisons with different laboratory and *in situ* measurements should be conducted in the future.

References

- Borgman, L.E., Irregular ocean waves: kinematics and forces. *The Sea*, Vol.9, *Ocean Engineering Science, Part A*, pp. 121-168, J. Wiley, New York, 1990.
- Brissette, F.P. and Tsanis, I.K., Estimation of wave directional spectra from pitch-roll buoy data. *J. of waterway, port, coastal, and ocean engineering*, 120(1), 93-115, 1994.
- Chase, J., Cote, L.J., Marks, W., Mehr, E., Pierson, W.J. Jr., Rönne, F.G., Stephenson, G., Vetter, R.C., and Walden, R.G., The directional spectrum of a wind generated sea as determined from data obtained by the Stereo Wave Observation Project. Tech. Rep., 267 pp, N.Y.U., Coll. of Eng., Dept. of Meteorol. and Oceanogr. and Engineering Statistics Group., New York, 1957.
- Chen, L. & Zhang, J. On interaction between intermediate-depth long waves and deep-water short waves. *J. of Ocean Engrg.*(in press), 1997.
- Forristall, G. Z., Kinematics in the crests of storm waves. *Proc. 20th Coastal Engineering Conference, ASCE*, pp. 208-222, Taipei, Taiwan, 1986.
- Funke, E. R. and Mansard, E. P. D., On the meaning of phase spectra. *Proc. of the International Symposium on Hydrodynamics in Ocean Engineering*, pp. 49-69, The Norwegian Institute of Technology, Norway, 1981.
- Goda, Y., Directional wave spectrum and its application in coastal engineering. in *Proc. of the International Conference on Hydrodynamics*, pp. 9-18, China Ocean Press. 1994.
- Gudmestad, O. T., Measured and predicted deep water wave kinematics in regular and irregular seas. *Report 1/92-A-25-100*, 83 pp., Offshore Technology Research Center, Texas A&M University, 1991.
- Hashimoto, N., Nagai, T. & Asai, T., Extension of the maximum entropy principle method for directional wave spectrum estimation. *Coastal Engineering 1994, ASCE*, pp. 232-246, 1994.

- Hasselmann, K., On the non-linear energy transfer in a gravity-wave spectrum. Part 1. General theory. *J. Fluid Mech.*, 12, 481–500, 1962.
- Herbers, T. H. C. and Guza, R. T., Estimation of directional wave spectra from multicomponent observations. *J. Phys. Oceanogr.*, 20, 1703–1724, 1990.
- Herbers, T. H. C. and Guza, R. T., Wind wave nonlinearity observed at the sea floor, Part I: forced wave energy. *J. Phys. Oceanogr.*, 21(12), 1740–1761, 1991.
- Herbers, T. H. C. & Guza, R. T., Wind-wave nonlinearity observed on the seafloor: Part II: Wavenumbers and third-order statistics. *J. Phys. Oceanogr.*, 22(5), 489–504, 1992.
- Hong, K., Nonlinear interactions between directional dual component waves in deep water. Ph. D. Thesis, Texas A&M University, 1993.
- Hsu, J. R. C., Tsuchiya, Y. and Silvester, R., Third-order approximation to short-crested waves *J. Fluid Mech.*, 90, 179–196, 1979.
- Irani, G.B., Gotwols, B.L., and Bjerkaas, A.W., The 1978 ocean wave dynamics experiment. Wave dynamics and radio probing of the ocean surface. Edited by O.M. Phillips and K. Hasselmann, pp. 165–179, Plenum, New York, 1986.
- Isobe, M., Kondo, K., and Horikawa, K., Extension of MLM for estimating directional wave spectrum. *Proc. Symposium on Description and Modeling of Directional seas, Paper NO. A-6*, pp 1–15, Technical University of Denmark, 1984.
- Jefferys, E. R., Comparison of three methods for calculation of directional spectra. *Proc. 5th International OMAE Symposium, Vol 1*, pp 45–50, ASME, Tokyo, 1986.
- Komen, G. J., Nonlinear contributions to the frequency spectrum of wind-generated water waves. *J. Phys. Oceanogr.*, 10, 779–790, 1980.
- Longuet-Higgins, M.S., Resonant interactions between two trains of gravity waves. *J. Fluid Mech.*, 12, 321–332, 1962.
- Longuet-Higgins, M.S., The propagation of short surface gravity waves on longer gravity waves. *J. Fluid Mech.*, 177, 293–306, 1987.

- Masuda, A., Kuo, Y., and Mitsuyasu, H., On the dispersion relation of random gravity waves, Part 1. Theoretical framework, *J. Fluid Mech.*, 92, 717-730, 1979.
- Mitsuyasu, H., Kuo, Y., and Masuda, A., On the dispersion relation of random gravity waves, Part 2. An experiment, *J. Fluid Mech.*, 92, 731-749, 1979.
- Phillips, O.M., Surface wave physics – a survey. *Flow Research Report*, 145, 91 pp, Flow Research Co. Division of Flow Industries, Inc., Kent, WA., 1979.
- Press, W.H., Teukolsky, S.A., Vetterling, W.T., Flannery, B.P., *Numerical recipes in FORTRAN: the art of scientific computing*, 2nd ed., 963 pp, Cambridge, 1992.
- Prislin, I., Nonlinear deterministic decomposition of short-crested ocean wave. Ph. D. Thesis, Texas A&M University, 1996.
- Prislin, I. & Zhang, J., Prediction of wave kinematics under the wave crest in short-crest irregular gravity waves. *Proc. 27th IAHR Congress*, pp 357-370, 1997.
- Prislin, I., Zhang, J. and Seymour, R. J., Deterministic decomposition of deep water short-crested irregular gravity waves. *J. Geophys. Res.*, 102(C6), 12,677-12,688, 1997.
- Sand, S.E., Three-dimensional deterministic structure of ocean waves. Institute of Hydrodynamics and Hydraulic Engineering, *Series Paper 24*, 177 pp, Technical University of Denmark, 1979.
- Schäffer, H.A. and Hylleberg P., Analysis of multidirectional waves using deterministic decomposition. in *International Symposium: Waves – physical and numerical modeling*, Vol. 2, pp. 911-920, UBC, Vancouver, Canada 1994.
- Seymour, R.J., Castel, D., McGehee, D., Thomas, J., O'Reilly, W., New technology in coastal wave monitoring. *Ocean Wave Measurement and analysis: Waves '93*, edited by O.T. Magoon and J.M. Hemsley, pp. 105-123, ASCE, 1993.

- Spell, C.A., Zhang, J., and Randall, R.E., Hybrid wave model for unidirectional irregular waves. Part II. Comparison with laboratory measurements. *J. Appl. Ocean Res.*, 18, 93–110, 1996.
- Su, M.Y. and Green, A.W., Experimental studies of strong nonlinear interactions of deep-water gravity waves. *Wave dynamics and radio probing of the ocean surface*, edited by O.M. Phillips and K. Hasselmann, pp. 231–253, Plenum, New York, 1981.
- Tick, L. J., A non-linear random model of gravity waves I. *J. Maths. and Mech.*, 8, 643–652, 1959.
- Torum, A. & Gudmestad, O. T., Water wave kinematics. *NATO ASI Series, Series E: Applied Science*, vol. 178, Kluwer Academic Publishers, 1989.
- van Heteren, J. and Keijser, H., and Schaap, B., Comparison wave directional measuring systems. *Appl. Ocean Res.*, 10(3), 128–143, 1988.
- Weber, B. L. & Barrick, D. E., On the nonlinear theory for gravity waves on the ocean's surface, Part I: Derivations. *J. Phys. Oceanog.*, 7, 3–7, 1977.
- Zhang, J., Hong, K., and Yue, D.K.P., Effects of wavelength ratio on wave modeling, *J. Fluid Mech.*, 248, 107–127, 1993.
- Zhang, J., Chen, L., Ye, M. and Randall, R.E., Hybrid wave model for unidirectional irregular waves. Part I. Theory and numerical scheme. *J. Appl. Ocean Res.*, 18, 77–92, 1996a.
- Zhang, J., Meza Conde, E. & Yang, J. Wave elevation based on the pressure measurements. *Texas A&M University, COE Rep. No. 352*, 1996b.
- Zhang, J., Conde, E. M. and Seymour, R. J., Experimental studies on energy dissipation in breaking waves. *Proc. 7th ISOPE, Vol III*, pp 178–183, 1997.

Appendix A Wave Properties by the Conventional Perturbation Solution

The dynamic pressure head, $z + P/(\rho g)$, can be derived from the Bernoulli equation

$$\frac{\partial \Phi}{\partial t} + \frac{1}{2} |\nabla \Phi|^2 + gz + \frac{P}{\rho} = C_0, \quad (\text{A.1})$$

where ρ is the density of water. For the interaction of two directional wave components, the hydrodynamic pressure obtained by the conventional perturbation solution is,

$$\begin{aligned} z + \frac{P}{\rho g} = & \sum_{i=1}^2 \left\{ a_i K_{pi} \cos \theta_i + \frac{\alpha_i^2 k_i}{2 \sinh(2k_i h)} \{1 - \cosh[2k_i(z+h)]\} \right. \\ & + \frac{\alpha_i^2 k_i}{2 \sinh(2k_i h)} [3(\alpha_i^2 - 1) \cosh 2k_i(z+h) - 1] \cos 2\theta_i \Big\} \\ & + \frac{a_1 a_2 k_2}{2\alpha_2} \left[-(1-\lambda) A_{(-)} \frac{\cosh[|\mathbf{k}_1 - \mathbf{k}_2|(z+h)]}{\cosh(|\mathbf{k}_1 - \mathbf{k}_2|h)} + E_{(-)} \right] \cos(\theta_1 - \theta_2) \\ & + \frac{a_1 a_2 k_2}{2\alpha_2} \left[(1+\lambda) A_{(+)} \frac{\cosh[|\mathbf{k}_1 + \mathbf{k}_2|(z+h)]}{\cosh(|\mathbf{k}_1 + \mathbf{k}_2|h)} + E_{(+)} \right] \cos(\theta_1 + \theta_2), \quad (\text{A.2}) \end{aligned}$$

where

$$E_{(\mp)} = -\alpha_1 \alpha_2 \lambda (\Gamma K_{p1} K_{p2} \pm R), \quad (\text{A.3a})$$

$$K_{pi} = \frac{\cosh[k_i(z+h)]}{\cosh k_i h}, \quad i = 1, 2, \quad (\text{A.3b})$$

$$R = \frac{\sinh[k_1(z+h)] \sinh[k_2(z+h)]}{\cosh k_1 h \cosh k_2 h}, \quad (\text{A.3c})$$

with Γ , α_i and λ being defined in § 2.1.1.

The velocity components are the spatial derivatives of the potential Φ ,

$$\begin{aligned} u = & \sum_{i=1}^2 \left\{ \frac{a_i g k_{ix}}{\sigma_i} K_{pi} \cos \theta_i + \frac{3 \alpha_i^2 k_{ix} \sigma_i \cosh[2k_i(z+h)]}{4 \sinh^4(k_i h)} \cos(2\theta_i) \right\} \\ & + \frac{a_1 a_2 \sigma_2}{2} A_{(-)} (k_{1x} - k_{2x}) \frac{\cosh[|\mathbf{k}_1 - \mathbf{k}_2|(z+h)]}{\cosh(|\mathbf{k}_1 - \mathbf{k}_2|h)} \cos(\theta_1 - \theta_2) \end{aligned}$$

$$+ \frac{a_1 a_2 \sigma_2}{2} A_{(+)}(k_{1x} + k_{2x}) \frac{\cosh[|\mathbf{k}_1 + \mathbf{k}_2|(z+h)]}{\cosh(|\mathbf{k}_1 + \mathbf{k}_2|h)} \cos(\theta_1 + \theta_2), \quad (\text{A.4a})$$

$$v = \sum_{i=1}^2 \left\{ \frac{a_i g k_{iy}}{\sigma_i} K_{pi} \cos \theta_i + \frac{3}{4} \frac{a_i^2 k_{iy} \sigma_i \cosh[2k_i(z+h)]}{\sinh^4(k_i h)} \cos(2\theta_i) \right\} \\ + \frac{a_1 a_2 \sigma_2}{2} A_{(-)}(k_{1y} - k_{2y}) \frac{\cosh[|\mathbf{k}_1 - \mathbf{k}_2|(z+h)]}{\cosh(|\mathbf{k}_1 - \mathbf{k}_2|h)} \cos(\theta_1 - \theta_2) \\ + \frac{a_1 a_2 \sigma_2}{2} A_{(+)}(k_{1y} + k_{2y}) \frac{\cosh[|\mathbf{k}_1 + \mathbf{k}_2|(z+h)]}{\cosh(|\mathbf{k}_1 + \mathbf{k}_2|h)} \cos(\theta_1 + \theta_2), \quad (\text{A.4b})$$

$$w = \sum_{i=1}^2 \left\{ \frac{a_i g k_i}{\sigma_i} \frac{\sinh[k_i(z+h)]}{\cosh(k_i h)} \sin \theta_i + \frac{3}{4} \frac{a_i^2 k_i \sigma_i \sinh[2k_i(z+h)]}{\sinh^4(k_i h)} \sin(2\theta_i) \right\} \\ + \frac{a_1 a_2 \sigma_2}{2} A_{(-)} |\mathbf{k}_1 - \mathbf{k}_2| \frac{\sinh[|\mathbf{k}_1 - \mathbf{k}_2|(z+h)]}{\cosh(|\mathbf{k}_1 - \mathbf{k}_2|h)} \sin(\theta_1 - \theta_2) \\ + \frac{a_1 a_2 \sigma_2}{2} A_{(+)} |\mathbf{k}_1 + \mathbf{k}_2| \frac{\sinh[|\mathbf{k}_1 + \mathbf{k}_2|(z+h)]}{\cosh(|\mathbf{k}_1 + \mathbf{k}_2|h)} \sin(\theta_1 + \theta_2). \quad (\text{A.4c})$$

The acceleration includes two parts: local acceleration and convective acceleration,

$$a_x = \sum_{i=1}^2 \left\{ a_i g k_{ix} \frac{\cosh[k_i(z+h)]}{\cosh(k_i h)} \sin \theta_i + \frac{a_i^2 k_{ix} \sigma_i^2}{2 \sinh^2(k_i h)} [3(\alpha_i^2 - 1) \cosh 2k_i(z+h) - 1] \sin(2\theta_i) \right\} \\ - \frac{a_1 a_2 (k_{1x} - k_{2x}) \sigma_2^2}{2} \left\{ A_{(-)}(1 - \lambda) \frac{\cosh[|\mathbf{k}_1 - \mathbf{k}_2|(z+h)]}{\cosh(|\mathbf{k}_1 - \mathbf{k}_2|h)} + T_{(-)} \right\} \sin(\theta_1 - \theta_2) \\ + \frac{a_1 a_2 (k_{1x} + k_{2x}) \sigma_2^2}{2} \left\{ A_{(+)}(1 + \lambda) \frac{\cosh[|\mathbf{k}_1 + \mathbf{k}_2|(z+h)]}{\cosh(|\mathbf{k}_1 + \mathbf{k}_2|h)} - T_{(+)} \right\} \sin(\theta_1 + \theta_2), \quad (\text{A.5a})$$

$$a_y = \sum_{i=1}^2 \left\{ a_i g k_{iy} \frac{\cosh[k_i(z+h)]}{\cosh(k_i h)} \sin \theta_i + \frac{a_i^2 k_{iy} \sigma_i^2}{2 \sinh^2(k_i h)} [3(\alpha_i^2 - 1) \cosh 2k_i(z+h) - 1] \sin(2\theta_i) \right\} \\ - \frac{a_1 a_2 (k_{1y} - k_{2y}) \sigma_2^2}{2} \left\{ A_{(-)}(1 - \lambda) \frac{\cosh[|\mathbf{k}_1 - \mathbf{k}_2|(z+h)]}{\cosh(|\mathbf{k}_1 - \mathbf{k}_2|h)} + T_{(-)} \right\} \sin(\theta_1 - \theta_2) \\ + \frac{a_1 a_2 (k_{1y} + k_{2y}) \sigma_2^2}{2} \left\{ A_{(+)}(1 + \lambda) \frac{\cosh[|\mathbf{k}_1 + \mathbf{k}_2|(z+h)]}{\cosh(|\mathbf{k}_1 + \mathbf{k}_2|h)} - T_{(+)} \right\} \sin(\theta_1 + \theta_2), \quad (\text{A.5b})$$

$$a_z = \sum_{i=1}^2 \left\{ -a_i g k_i \frac{\sinh[k_i(z+h)]}{\cosh(k_i h)} \cos \theta_i + \frac{a_i^2 k_i \sigma_i^2 \sinh 2k_i(z+h)}{2 \sinh^2(k_i h)} [1 - 3(\alpha_i^2 - 1) \cos 2\theta_i] \right\} \\ + \frac{a_1 a_2 \sigma_2^2}{2} \left\{ A_{(-)} |\mathbf{k}_1 - \mathbf{k}_2| (1 - \lambda) \frac{\sinh[|\mathbf{k}_1 - \mathbf{k}_2|(z+h)]}{\cosh(|\mathbf{k}_1 - \mathbf{k}_2|h)} + V_{(-)} \right\} \cos(\theta_1 - \theta_2) \\ + \frac{a_1 a_2 \sigma_2^2}{2} \left\{ A_{(+)} |\mathbf{k}_1 + \mathbf{k}_2| (1 + \lambda) \frac{\sinh[|\mathbf{k}_1 + \mathbf{k}_2|(z+h)]}{\cosh(|\mathbf{k}_1 + \mathbf{k}_2|h)} + V_{(+)} \right\} \cos(\theta_1 + \theta_2), \quad (\text{A.5c})$$

where

$$T_{(\mp)} = \frac{\lambda}{\sinh k_1 h \sinh k_2 h} [\Gamma \cosh k_1(z+h) \cosh k_2(z+h) \pm \sinh k_1(z+h) \sinh k_2(z+h)], \quad (\text{A.6a})$$

$$V_{(\mp)} = \frac{\lambda}{\sinh k_1 h \sinh k_2 h} [(\Gamma k_1 \mp k_2) \sinh k_1(z+h) \cosh k_2(z+h) \mp (k_1 \mp \Gamma k_2) \cosh k_1(z+h) \sinh k_2(z+h)]. \quad (\text{A.6b})$$

Appendix B Parameters of the Phase Modulation Solution

The parameters of the phase modulation solution in (2.19) can be obtained as discussed in § 2.1.2. By truncating the first order spacial derivatives of the modulated short-wave potential to $O(\lambda^4)$, the related parameters can be expressed as follows.

$$\rho_{00} = \alpha_1 \Gamma, \quad (\text{B.1a})$$

$$\rho_{01} = \frac{1}{2}(\alpha_1^2 \Gamma^2 - 1), \quad (\text{B.1b})$$

$$\rho_{02} = \frac{\alpha_1 \Gamma}{4}(\alpha_1^2 \Gamma^2 - 1), \quad (\text{B.1c})$$

$$\rho_{03} = \frac{1}{8}(\alpha_1^4 \Gamma^4 + 2\alpha_1^2 \Gamma^2 - 4\alpha_1^2 + 1), \quad (\text{B.1d})$$

$$\rho_{04} = \frac{\alpha_1 \Gamma}{16}(\alpha_1^4 \Gamma^4 - 2\alpha_1^2 \Gamma^2 + 1). \quad (\text{B.1e})$$

$$\rho_{10} = -\Gamma, \quad (\text{B.2a})$$

$$\rho_{11} = 0, \quad (\text{B.2b})$$

$$\rho_{12} = \frac{1}{4}(4\alpha_1^2 \Gamma - 3\alpha_1^2 \Gamma^3 - \Gamma). \quad (\text{B.2c})$$

$$\rho_{20} = \frac{\alpha_1}{2} \Gamma^3. \quad (\text{B.3})$$

$$\gamma_{00} = \alpha_1 \Gamma^2, \quad (\text{B.4a})$$

$$\gamma_{01} = \frac{\Gamma}{2}(\alpha_1^2 \Gamma^2 - 1), \quad (\text{B.4b})$$

$$\gamma_{02} = \frac{\alpha_1}{4}(\alpha_1^2 \Gamma^4 + \Gamma^2 - 2), \quad (\text{B.4c})$$

$$\gamma_{03} = \frac{\Gamma}{8}(\alpha_1^4 \Gamma^4 + 2\alpha_1^2 \Gamma^2 - 4\alpha_1^2 + 1), \quad (\text{B.4d})$$

$$\gamma_{04} = \frac{\alpha_1}{16}(\alpha_1^4 \Gamma^6 + 8\alpha_1^2 \Gamma^4 + 3\Gamma^2 - 14\alpha_1^2 \Gamma^2 + 4\alpha_1^2 - 2). \quad (\text{B.4e})$$

$$\gamma_{10} = -\frac{1}{2}\Gamma^2, \quad (\text{B.5a})$$

$$\gamma_{11} = 0, \quad (\text{B.5b})$$

$$\gamma_{12} = \frac{\Gamma^2}{8}(6\alpha_1^2 - 5\alpha_1\Gamma^2 - 1). \quad (\text{B.5c})$$

$$\gamma_{20} = \frac{\alpha_1}{6}\Gamma^4. \quad (\text{B.6})$$

$$\tau_0 = \frac{1}{4}(2\alpha_1 - \alpha_1\Gamma^2 - \alpha_1^{-1}), \quad (\text{B.7a})$$

$$\tau_1 = \frac{1}{2}\alpha_1^2\Gamma(1 - \Gamma^2), \quad (\text{B.7b})$$

$$\tau_2 = \frac{1}{16}[2\alpha_1 - \alpha_1^{-1} - \alpha_1^3(5\Gamma^4 + 2\Gamma^3 - 6\Gamma^2)], \quad (\text{B.7c})$$

$$\tau_3 = \frac{1}{16}(-4\alpha_1^4\Gamma^5 - \alpha_1^4\Gamma^4 + 4\alpha_1^4\Gamma^3 - 6\alpha_1^2\Gamma^3 + 12\alpha_1^2\Gamma - \Gamma). \quad (\text{B.7d})$$

$$b_0 = \frac{2\alpha_1 + \alpha_1\Gamma^2 + \alpha_1^{-1}}{4}, \quad (\text{B.8a})$$

$$b_1 = \frac{\Gamma(2\alpha_1^2 - \alpha_1^2\Gamma^2 - 1)}{4}, \quad (\text{B.8b})$$

$$b_2 = \frac{\alpha_1^{-1} - \alpha_1(6 - 4\Gamma^2) + \alpha_1^3\Gamma^2(6 - 3\Gamma^2 - 2\Gamma)}{16}, \quad (\text{B.8c})$$

$$b_3 = \frac{1}{16}(\alpha_1^5\Gamma^5 + 4\alpha_1^4\Gamma^5 + \alpha_1^4\Gamma^4 - 4\alpha_1^4\Gamma^3 - 2\alpha_1^3\Gamma^3 + 6\alpha_1^2\Gamma^3 - 12\alpha_1^2\Gamma + \alpha_1\Gamma + \Gamma). \quad (\text{B.8d})$$

Appendix C Wave Properties by the Phase Modulation Solution

The dynamic pressure of the short-wave component modulated by a long-wave component can be obtained from the Bernoulli equation

$$\frac{P_3}{\rho g} + z = -\frac{1}{g} \nabla \Phi_3 \cdot \nabla \Phi_1 - \frac{1}{g} \frac{\partial \Phi_3}{\partial t} - \frac{1}{2g} |\nabla \Phi_3|^2, \quad (\text{C.1})$$

with

$$\Phi_1 = \frac{a_1 g \cosh[k_1(z+h)]}{\sigma_1 \cosh(k_1 h)} \sin \theta_1, \quad (\text{C.2})$$

where the subscripts 1 and 3 represent the long-wave component and the modulated short-wave component, respectively. Hence, by substituting the phase modulation solution given in § 2.1.2 into (C.1), we have

$$\frac{P_3}{\rho g} + z = a_3 e^{k_3 f_k} \left[(1 + \varepsilon_1 C \cos \theta_1) \cos \bar{\theta}_3 + \varepsilon_1 S \sin \theta_1 \sin \bar{\theta}_3 \right] - \frac{1}{2} a_3^2 k_3 e^{2k_3 f_k}, \quad (\text{C.3})$$

where

$$C = \tau - \lambda^{-1} \Gamma K_{p1} + \lambda^{-1} \alpha_1^{-1} \sum_{j=0}^{J+1} \rho_j (k_1 z)^j, \quad (\text{C.4a})$$

$$S = -\tau \lambda + \lambda^{-1} \alpha_1^{-1} - \lambda^{-1} H_{p1} - \lambda k_3 z \sum_{j=0}^J \gamma_j (k_1 z)^j, \quad (\text{C.4b})$$

$$H_{p1} = \frac{\sinh[k_1(z+h)]}{\cosh k_1 h}, \quad (\text{C.4c})$$

with Γ and K_{p1} being defined in (2.6d) and (A.3b), respectively.

The velocity components of the modulated short-wave component can be calculated by the spatial derivatives of Φ_3 ,

$$u = a_3 \sigma_3 e^{k_3 f_k} [(\cos \beta_3 + \varepsilon_1 C_u \cos \theta_1) \cos \bar{\theta}_3 + \varepsilon_1 S_u \sin \theta_1 \sin \bar{\theta}_3], \quad (\text{C.5a})$$

$$v = a_3 \sigma_3 e^{k_3 f_k} [(\sin \beta_3 + \varepsilon_1 C_v \cos \theta_1) \cos \tilde{\theta}_3 + \varepsilon_1 S_v \sin \theta_1 \sin \tilde{\theta}_3], \quad (\text{C.5b})$$

$$w = a_3 \sigma_3 e^{k_3 f_k} [\varepsilon_1 C_w \sin \theta_1 \cos \tilde{\theta}_3 + (1 + \varepsilon_1 S_w \cos \theta_1) \sin \tilde{\theta}_3], \quad (\text{C.5c})$$

where

$$C_u = \tau \cos \beta_3 + \cos \beta_1 \sum_{j=0}^{J+1} \rho_j (k_1 z)^j, \quad (\text{C.6a})$$

$$C_v = \tau \sin \beta_3 + \sin \beta_1 \sum_{j=0}^{J+1} \rho_j (k_1 z)^j, \quad (\text{C.6b})$$

$$C_w = \sum_{j=1}^{J+1} j \rho_j (k_1 z)^{j-1}, \quad (\text{C.6c})$$

$$S_u = \cos \beta_1 \left[1 - \tau \lambda^2 \alpha_1 - \sum_{j=0}^J \gamma_j (k_1 z)^{j+1} \right], \quad (\text{C.6d})$$

$$S_v = \sin \beta_1 \left[1 - \tau \lambda^2 \alpha_1 - \sum_{j=0}^J \gamma_j (k_1 z)^{j+1} \right], \quad (\text{C.6e})$$

$$S_w = \tau + \sum_{j=0}^{J+1} (j+1) \gamma_j (k_1 z)^j. \quad (\text{C.6f})$$

The acceleration of the modulated short-wave component is in the form of

$$\mathbf{a} = \left\{ \begin{array}{l} \frac{\partial u_3}{\partial t} + (u_1 + u_3) \frac{\partial u_3}{\partial x} + (v_1 + v_3) \frac{\partial u_3}{\partial y} + (w_1 + w_3) \frac{\partial u_3}{\partial z} \\ \frac{\partial v_3}{\partial t} + (u_1 + u_3) \frac{\partial v_3}{\partial x} + (v_1 + v_3) \frac{\partial v_3}{\partial y} + (w_1 + w_3) \frac{\partial v_3}{\partial z} \\ \frac{\partial w_3}{\partial t} + (u_1 + u_3) \frac{\partial w_3}{\partial x} + (v_1 + v_3) \frac{\partial w_3}{\partial y} + (w_1 + w_3) \frac{\partial w_3}{\partial z} \end{array} \right\}, \quad (\text{C.7})$$

where the first-order long-wave velocity components are,

$$u_1 = \frac{a_1 g k_1}{\sigma_1} K_{p1} \cos \beta_1 \cos \theta_1, \quad (\text{C.8a})$$

$$v_1 = \frac{a_1 g k_1}{\sigma_1} K_{p1} \sin \beta_1 \cos \theta_1, \quad (\text{C.8b})$$

$$w_1 = \frac{a_1 g k_1}{\sigma_1} H_{p1} \sin \theta_1, \quad (\text{C.8c})$$

the time derivatives of the modulated velocity components are

$$\begin{aligned} \frac{\partial u_3}{\partial t} = a_3 \sigma_3^2 e^{k_3 f_k} & \left\{ \sin \tilde{\theta}_3 [\cos \beta_3 + a_1 k_3 \lambda \cos \theta_1 \cos \beta_3 \sum_{j=0}^{J+1} \rho_j(k_1 z)^j + \varepsilon_1 C_u \cos \theta_1 \right. \\ & - \varepsilon_1 \lambda S_u \cos \theta_1] + \cos \tilde{\theta}_3 \sin \theta_1 [\lambda \varepsilon_1 C_u - \varepsilon_1 S_u - a_1 k_3 \lambda \cos \beta_3 \\ & \left. + \varepsilon_1 \lambda k_3 z \cos \beta_3 \sum_{j=0}^J \gamma_j(k_1 z)^{j+1}] \right\}, \end{aligned} \quad (\text{C.9a})$$

$$\begin{aligned} \frac{\partial v_3}{\partial t} = a_3 \sigma_3^2 e^{k_3 f_k} & \left\{ \sin \tilde{\theta}_3 [\sin \beta_3 + a_1 k_3 \lambda \cos \theta_1 \sin \beta_3 \sum_{j=0}^{J+1} \rho_j(k_1 z)^j + \varepsilon_1 C_v \cos \theta_1 \right. \\ & - \varepsilon_1 \lambda S_v \cos \theta_1] + \cos \tilde{\theta}_3 \sin \theta_1 [\varepsilon_1 \lambda C_v - \varepsilon_1 S_v - a_1 k_3 \lambda \sin \beta_3 \\ & \left. + \varepsilon_1 \lambda k_3 z \sin \beta_3 \sum_{j=0}^J \gamma_j(k_1 z)^{j+1}] \right\}, \end{aligned} \quad (\text{C.9b})$$

$$\begin{aligned} \frac{\partial w_3}{\partial t} = a_3 \sigma_3^2 e^{k_3 f_k} & \left\{ \sin \tilde{\theta}_3 \sin \theta_1 [\varepsilon_1 \lambda S_w - a_1 k_3 \lambda + \varepsilon_1 \lambda k_3 z \sum_{j=0}^{J+1} \rho_j(k_1 z)^j + \varepsilon_1 C_w] \right. \\ & \left. - \cos \tilde{\theta}_3 [1 + \varepsilon_1 \cos \theta_1 (\lambda + S_w) + a_1 k_3 \lambda \sum_{j=0}^{J+1} \rho_j(k_1 z)^j] \right\}, \end{aligned} \quad (\text{C.9c})$$

and the spatial derivatives of the modulated velocity components are:

$$\frac{\partial u_3}{\partial x} = -a_3 \sigma_3 k_3 e^{k_3 f_k} \cos^2 \beta_3 \sin \tilde{\theta}_3, \quad (\text{C.10a})$$

$$\frac{\partial u_3}{\partial y} = -a_3 \sigma_3 k_3 e^{k_3 f_k} \cos \beta_3 \sin \beta_3 \sin \tilde{\theta}_3, \quad (\text{C.10b})$$

$$\frac{\partial u_3}{\partial z} = a_3 \sigma_3 k_3 e^{k_3 f_k} \cos \beta_3 \cos \tilde{\theta}_3, \quad (\text{C.10c})$$

$$\frac{\partial v_3}{\partial x} = \frac{\partial u_3}{\partial y}, \quad (\text{C.10d})$$

$$\frac{\partial v_3}{\partial y} = -a_3 \sigma_3 k_3 e^{k_3 f_k} \sin^2 \beta_3 \sin \tilde{\theta}_3, \quad (\text{C.10e})$$

$$\frac{\partial v_3}{\partial z} = a_3 \sigma_3 k_3 e^{k_3 f_k} \sin \beta_3 \cos \tilde{\theta}_3, \quad (\text{C.10f})$$

$$\frac{\partial w_3}{\partial x} = \frac{\partial u_3}{\partial z}, \quad (\text{C.10g})$$

$$\frac{\partial w_3}{\partial y} = \frac{\partial v_3}{\partial z}, \quad (\text{C.10h})$$

$$\frac{\partial w_3}{\partial z} = a_3 \sigma_3 k_3 e^{k_3 f_k} \sin \tilde{\theta}_3. \quad (\text{C.10i})$$

For a short-wave component modulated by M long-wave components, the modulated surface elevation is the sum of the modulations by all M long-wave components,

$$\zeta_3 = a_3 \left(1 + \sum_{m=1}^M \varepsilon_m b_m \cos \theta_m \right) \cos(\tilde{\theta}_3), \quad (\text{C.11})$$

where

$$\tilde{\theta}_3 = k_{3x}x + k_{3y}y - \sigma_3 t + \delta_3 + \sum_{m=1}^M k_3 a_m \rho_{0m} \sin \theta_m + \sum_{m=1}^M \Delta_m \varepsilon_m \sin \theta_m, \quad (\text{C.12a})$$

$$\Delta_m = \lambda_m \tau_m, \quad \lambda_m = \frac{\sigma_m}{\sigma_3}. \quad (\text{C.12b})$$

The modulated dynamic pressure is, then,

$$\frac{P_3}{\rho g} + z = a_3 e^{k_3 f_k} \left[(1 + \varepsilon_1 C \cos \theta_1) \cos \tilde{\theta}_3 + \varepsilon_1 S \sin \theta_1 \sin \tilde{\theta}_3 \right], \quad (\text{C.13})$$

with

$$C = \sum_{m=1}^M \left[\tau_m - \lambda_m^{-1} \Gamma_m K_{pm} + \lambda_m^{-1} \alpha_m^{-1} \sum_{j=0}^{J+1} \rho_{mj} (k_m z)^j \right], \quad (\text{C.14a})$$

$$S = \sum_{m=1}^M \left[-\tau_m \lambda_m + \lambda_m^{-1} \alpha_m^{-1} - \lambda_m^{-1} H_{pm} - \lambda_m k_3 z \sum_{j=0}^{J+1} \gamma_{mj} (k_m z)^j \right], \quad (\text{C.14b})$$

$$\lambda_m = \frac{\sigma_m}{\sigma_3}, \quad H_{pm} = \frac{\sinh[k_m(z+h)]}{\cosh k_m h}, \quad K_{pm} = \frac{\cosh[k_m(z+h)]}{\cosh k_m h}. \quad (\text{C.14c})$$

The modulated velocity components are in the same form as (C.5), but with

$$C_u = \sum_{m=1}^M \left[\tau_m \cos \beta_3 + \cos \beta_m \sum_{j=0}^{J+1} \rho_{mj} (k_m z)^j \right], \quad (\text{C.15a})$$

$$C_v = \sum_{m=1}^M \left[\tau_m \sin \beta_3 + \sin \beta_m \sum_{j=0}^{J+1} \rho_{mj} (k_m z)^j \right], \quad (\text{C.15b})$$

$$C_w = \sum_{m=1}^M \sum_{j=1}^{J+1} j \rho_{mj} (k_m z)^{j-1}, \quad (\text{C.15c})$$

$$S_u = \sum_{m=1}^M \cos \beta_m \left[1 - \tau_m \lambda_m^2 \alpha_m - \sum_{j=0}^{J+1} \gamma_{mj} (k_m z)^{j+1} \right], \quad (\text{C.15d})$$

$$S_v = \sum_{m=1}^M \sin \beta_m \left[1 - \tau_m \lambda_m^2 \alpha_m - \sum_{j=0}^{J+1} \gamma_{mj} (k_m z)^{j+1} \right], \quad (\text{C.15e})$$

$$S_w = \sum_{m=1}^M \left[\tau_m + \sum_{j=0}^{J+1} (j+1) \gamma_{mj} (k_m z)^j \right]. \quad (\text{C.15f})$$

The modulated acceleration components can be calculated as (C.7), but with the summation over all the long-wave components,

$$u_1^{(1)} = \sum_{m=1}^M \frac{a_m g k_m}{\sigma_m} K_{pm} \cos \beta_m \cos \theta_m, \quad (\text{C.16a})$$

$$v_1^{(1)} = \sum_{m=1}^M \frac{a_m g k_m}{\sigma_m} K_{pm} \sin \beta_m \cos \theta_m, \quad (\text{C.16b})$$

$$w_1^{(1)} = \sum_{m=1}^M \frac{a_m g k_m}{\sigma_m} H_{pm} \sin \theta_m, \quad (\text{C.16c})$$

$$f_k = z - \sum_{m=1}^M \left\{ a_m \cos \theta_m + \varepsilon_m z \cos \theta_m \left[\sum_{j=0}^J \gamma_{jm} (k_m z)^j \right] \right\}, \quad (\text{C.16d})$$

$$\tilde{\theta}_3 = k_{3x} x + k_{3y} y - \sigma_3 t + \delta_3 + \sum_{m=1}^M \left[k_3 a_m \sin \theta_m \sum_{j=0}^J \rho_{jm} (k_m z)^j \right]. \quad (\text{C.16e})$$

